The Influence of Cellular Structure on the Dynamics of Detonations with Constant Mass Divergence

by

Bijan Borzou

Thesis submitted to the
Faculty of Graduate and Postdoctoral Studies
In partial fulfillment of the requirements
For the Ph.D. degree in
Mechanical Engineering

Ottawa-Carleton Institute for Mechanical and Aerospace Engineering
Faculty of Engineering
University of Ottawa

Abstract

Detonation waves are supersonic combustion waves that have a complex three-dimensional cellular structure. There is growing experimental evidence that the cellular structure of detonations promotes their propagation in the presence of losses. In spite of that, the conventional model for the detonation structure, known as the Zeldovich - Von Neumann - Doring (ZND) model, neglects the existence of cellular structure for detonations and assumes the wave to consist of a strong leading planar shock coupled with trailing chemical reactions. Therefore, the influence of cellular structure on the dynamics and extinction limits of detonation waves has been of particular interest.

Previous studies have investigated the influence of cellular structure on the dynamics of detonations with mass divergence in the framework of narrow tubes, porous-walled tubes and weak confinement. However, precise quantification of the loss mechanism in these frameworks has been associated with some difficulties. Complex flow in the boundary layers, inherent in thin tubes, or attenuation of the transverse waves in the porous-walled tubes has made the evaluation of the loss mechanism more difficult in such geometries.

In this thesis, a novel well-posed problem is formulated for detonations with mass divergence. It is shown that detonations propagating in a channel with a cross-section area increasing exponentially have a constant mass divergence. The detonations were found to propagate at a quasi-steady speed below the ideal Chapman-Jouguet velocity. This permitted to make meaningful comparison with the theoretical models and simulations.

The experiments were performed in two mixtures, one displaying characteristic weakly unstable detonations ($2C_2H_2 + 5O_2 + 21Ar$), and the other displaying highly unstable detonations ($C_3H_8 + 5O_2$). The dependence of the velocity deficits and limits on the amount of mass divergence for the two mixtures were compared with the predictions of the quasi-one-dimensional ZND model with lateral mass divergence. Since the ZND model neglects the cellular structure of the detonations, such comparison permitted to asses the influence of cellular structure on the dynamics of detonations with mass divergence.

Comparisons were also made with the results of simulations of inviscid cellular detonations. These comparisons showed that the velocity deficits and critical rate of mass divergence in the weakly unstable mixture were reasonably well predicted by the quasi-one-dimensional model. For smaller values of mass divergence rate, a good agreement between the experiments and the predictions of the two-dimensional cellular simulations was observed for the weakly unstable mixture. For the highly unstable detonations, the quasi-one-dimensional model significantly over-predicted the effect of mass divergence.

Detonations were observed for rates of mass divergence 93% higher than the critical predicted value, displaying more substantial velocity deficits than predicted. Such observations show conclusively that the ZND model cannot capture the dynamics of highly unstable detonations on large scales.

Acknowledgements

For the years of guidance, I would like to thank my supervisor Matei I. Radulescu. He has helped me to develop my research skills over the years we worked together. He has provided fantastic guidance and cooperation throughout my PhD studies. I wish to acknowledge NSERC Hydrogen Canada (H2CAN) Strategic Research Network for their sponsoring this thesis work and financial support to Dr. Radulescu through a Discovery Grant. I also thank Shell Canada for their financial support of this thesis.

I would also like to thank Karl German, Terrence R. Phenix, Mohammed Saif Al Islam and Qiang Xiao for help in conducting the experiments.

I would like to acknowledge Professor Sam Falle of the University of Leeds for providing the numerical code used in the thesis.

My parents have been essential in helping me achieve our dreams. I am blessed beyond measure to have parents whose support and encouragement, during the lowest of lows and the highest of highs, fuels me every moment. I would especially like to thank my mother for opening my eyes toward the dreams and for all her dedications for my life, my studies and my goals. Also I have been so gifted for having a great father who has always been there for support. I dedicate this work to my parents.

I really like to appreciate the help and assistance of my brother and sisters in all these hard years of being far away from home. I would also like to admire the supports of my grandparents during all the years of studies.

I would like to thank my best friend forever, Mohammad Alavirad, whom I cannot call anything but my brother. His help, presence and dedications in the last ten years of my life cannot be described by words. Without him being there, passing this long road was nothing but impossible.

Contents

List of Figures

Nomenclature

Roman Symbols

A	Channel cross-section area
A'	Stream tube area
c	Sound speed
c_p	Specific heat at constant pressure
D	Detonation speed
E_a	Activation energy
e	Internal energy per unit mass
H	Heaviside function
h	Enthalpy per unit mass
K	Area divergence rate of the channel
K_i	Induction rate parameter
K_r	Reaction rate parameter
M	Mach number
N	Total number of species
p	Pressure
Q	Chemical energy content
q	Chemical heat release
R	Ideal gas constant
T	Temperature
t	Time
t_i	Induction time scale
t_e	Reaction time scale
u	Flow velocity in x direction
v	Flow velocity in y direction
W	Molar mass
x	Horizontal coordinate of space
Y	Mass fraction
y	Vertical coordinate of space

Greek Symbols

α	Area divergence rate of the stream tube
γ	Specific heat ratio
Δ	Detonation wave thickness
$\Delta_{1/2}$	Half reaction length
Δ_i	Induction zone length scale
η	Sonic parameter
λ_i	Progress variable for the induction zone
λ_r	Progress variable for the reaction zone
ν	Reaction order
ρ	Density
$\dot{\sigma}$	Thermicity
τ	Time coordinate in the shock frame of reference
Φ_{BL}	Boundary layer loss term
χ	Stability parameter
ω	Net rate of creation/depletion

Subscripts

0	Unburnt upstream state
BL	Boundary layer
CJ	Chapman-Jouguet
eff	Effective
exp	Experimental
i	Induction zone
ign	Ignition
r	Reaction zone
s	Shocked state
VN	Von Neumann state

Superscripts

$'$	Shock frame of reference
$\tilde{}$	Dimensional variable
$*$	Critical value

Abbreviations

CJ	Chapman-Jouguet
DNS	Direct Numerical Simulation
FPS	Frame Per Second
GPI	Grid per induction zone
HVI	High Voltage Ignition
ODE	Ordinary Differential Equation
PVC	Polyvinyl Chloride
VN	Von Neumann
ZND	Zel'dovich-Von Neumann-Doring

Chapter 1

Introduction

1.1 Overview

It has been well known for the past 50 years that real detonations exhibit a complex three-dimensional cellular structure [1]. The multi-dimensional effects are manifested as interactions between the leading and transverse shocks [2, 3]. There is now a growing experimental evidence that the cellular structure of detonations promotes their propagation in the presence of losses, such as friction, heat loss and geometrical divergence. In the present thesis, the influence of cellular structure on the dynamics of detonations with mass divergence is addressed. The dynamics of detonation waves in the presence of a well-controlled and constant global rate of mass divergence is studied. The discrepancy between the real dynamics and the predictions by current theoretical models is addressed quantitatively in this thesis.

1.2 State-of-the-art

1.2.1 Detonation cellular structure

Detonation waves are supersonic self-sustained reaction waves. They propagate with a velocity of approximately 2000 m/s in reactive gases and usually in excess of 6000 m/s in condensed phase energetic materials. These waves consist of a strong leading shock coupled with trailing chemical reactions. The shock heats the gas through compression and initiates the reactions. The subsequent expansion of the gases resulting from chemical energy release sustains the leading shock. Using a control volume approach neglecting the

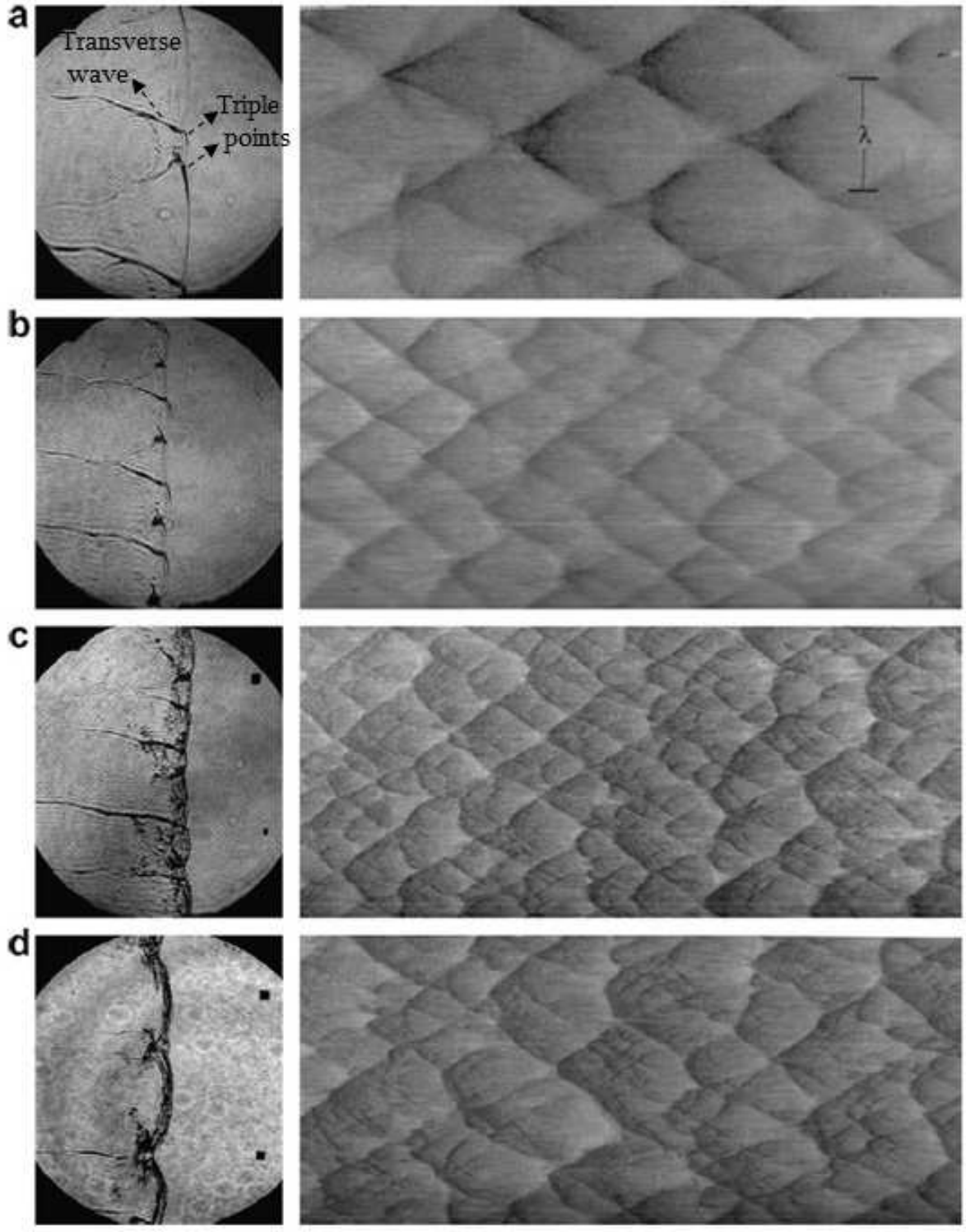

Figure 1.1: Schlieren images from detonation waves and their corresponding cellular structure in (a) $2H_2 + O_2 + 17Ar$, (b) $2H_2 + O_2 + 12Ar$, (c) $H_2 + N_2O + 1.33N_2$ and (d) $C_3H_8 + 5O_2 + 9N_2$ [4].

structure of the wave, known as Chapman-Jouguet (CJ) theory, one can predict various steady averaged detonation parameters, including velocity [5]. However, this control volume approach gives no insight into the structure of a detonation wave. In the past 50 years, experimental visualization of the reaction zone structure clarified the propagation mechanism. For instance, as can be seen in Figure 1.1, detonation waves have a multi-front shock structure. It is now well known that there are pressure, temperature and velocity fluctuations in the reaction zone caused by instabilities [6]. These instabilities in real detonation waves are caused, in part, by the exponential temperature dependence of the chemical reaction rates, as well as the hydrodynamic instabilities of the reaction front [6]. The instabilities manifest themselves as a cellular structure along with transversely propagating shock waves.

Figure 1.1 shows images taken by Austin [4] of the detonation wave structure in different reactive mixtures. The multi-shock front, the laterally sweeping transverse waves and the triple points at their intersections can be seen in the images. It has been shown that if one tracks the path of these triple points and visualizes them along the propagation path, the unstable three-dimensional cellular structure of the detonation wave is revealed [2, 3]. In Figure 1.1, the cellular structure obtained from tracking the time history of the path of triple points is also shown for the mixtures. These images, usually called "soot-foil" images, are obtained by passing a detonation over a lightly sooted surface [7, 8]. In this case, a pattern is left scoured in the soot by the triple points. This cellular pattern is a manifestation of the instability of the front and the cell width represents the length scale of the instability [6].

Such experimental investigations not only have visualized the unstable cellular structure for detonation waves but have also revealed striking regularity differences between the detonation structure of different mixtures. For example, in the images taken by Austin [4] (Figure 1.1) mixtures *a* ($2H_2 + O_2 + 17Ar$) and *b* ($2H_2 + O_2 + 12Ar$) have relatively smooth fronts and periodically-spaced transverse shock waves. The detonation waves in such mixtures with regular cellular structures have been called "weakly unstable" detonations in the literature and are characterized by weaker chemical reaction rate dependence to temperature fluctuations [9, 10, 11, 12]. However, in mixtures *c* ($H_2 + N_2O + 1.33N_2$) and *d* ($C_3H_8 + 5O_2 + 9N_2$) the fronts have a more roughened appearance. Irregular spacing of the transverse waves can also be seen for these mixtures. Consequently, the cellular structure of these mixtures also show more irregularities in the size, shape and pattern. The turbulence generated in the structure of these so-called "highly unstable" detonations is believed to promote turbulent mixing and to enhance

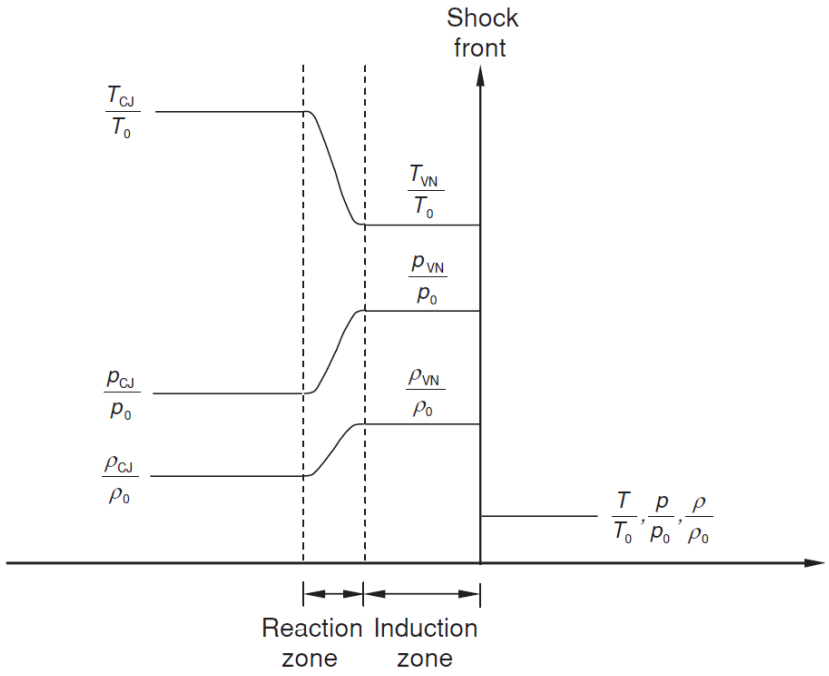

Figure 1.2: The steady structure assumed for detonation waves by the ZND model including a planar shock front, induction and reaction zones.

the burning rates [9, 13].

The conventional model for the detonation structure, known as the Zeldovich - Von Neumann - Doering (ZND), neglects the existence of cellular structure for detonations and it assumes the wave to consist of a strong leading planar shock coupled with trailing chemical reactions [5, 3]. The detonation wave is assumed to consist of a steady planar shock front having a subsequent zone of generation of radicals (induction zone) and a zone of recombination of the generated radicals into product molecules and consequent energy release (reaction zone). Figure 1.2 shows this idealized ZND structure for a steady detonation wave.

To account for the attenuation of detonations in the presence of losses, quasi-one-dimensional extensions have been introduced for the ZND model by taking friction, mass divergence and heat loss into consideration [14, 15, 16, 17]. This class of models is discussed below.

1.2.2 Detonation extinction limits in narrow tubes

It has been observed experimentally that in the propagation of detonations in narrow tubes that the wave dynamics and its extinction limits are governed by losses to the tube walls [18, 19, 20, 21, 22, 23]. During the propagation, the viscous boundary layers developing along the tube walls act as a sink of mass from the tube core to the boundary layers. The flow diverges due to the negative boundary layer displacement thickness with respect to a reference coordinate system fixed to the shock front. Divergence of the streamlines in the reaction zone results in a curved detonation front experiencing a velocity deficit [20, 24]. The velocity deficit of the front grows with decreasing tube size, typically on the order of 20%, until transition to deflagration speeds occurs [25].

The first model of detonation attenuation and extinction limits in narrow tubes was due to Fay [15]. Fay modeled the boundary layer displacement effect within the reaction zone via boundary layer theory, and related it to the uniform flow divergence experienced in an average sense by the detonation front. Chao *et al.* [26] and Camargo *et al.* [27] used Fay's model by coupling the boundary layer analysis with a quasi-one-dimensional model for the reaction zone in the presence of mass divergence.

However, much of the debate in the literature is related to whether the detonation wave dynamics and its attenuation by the local conditions at the walls can be modeled in a global hydrodynamic sense [9] in spite of the systematic departures from a quasi-one-dimensional structure due to the cellular instability. The answer to this question can be obtained by comparing the behaviour of the detonation wave with global models for its attenuation.

Subsequently and using their quasi-one-dimensional extension to the ZND model, Chao *et al.* [26] and Camargo *et al.* [27] found relatively good quantitative agreement between experiment and predictions for mixtures characterized by regular cellular structures in their so-called *weakly unstable* mixtures (e.g. $H_2 + 0.5O_2 + 1.5Ar$ and $C_2H_2 + 2.5O_2 + 14Ar$). For more unstable mixtures, however, the limits predicted by their theory did not match with the experimental values [27] and were found to over-predict the limits as detonations would propagate under conditions marked by extinction in the models. The authors took this result as indicative of the growing role of the three-dimensional cellular detonation structure in promoting its propagation. While the results highlight that a global hydrodynamic theory appears to be valid for weakly unstable detonations, no attempt was made to visualize the wave structure and to identify the mechanisms controlling the losses in more unstable detonations. Furthermore, the

question of whether or not a global hydrodynamic description is valid in more unstable detonations still remains.

1.2.3 Detonation extinction limits in porous-walled tubes

In an attempt to control the amount of lateral mass divergence and visualize the cellular structure dynamics, Radulescu performed experiments in porous wall tubes [28, 29]. When the tube wall is porous, the global mass divergence is controlled by the porosity of the walls. Since the lateral mass divergence in porous wall tubes is much greater than in the boundary layers of the narrow solid tubes, the detonation limits occur before the onset of single head spin. Near failure, the front maintains a global cellular structure, which can then be monitored [28, 29].

For weakly unstable detonations, the authors have found that the porous wall acted mainly to provide a global mass divergence to the front, which became progressively more curved as the limits were approached [28, 29]. In more unstable mixtures, however, localized explosions and re-generation of new transverse waves were observed as the limits were approached. Radulescu and Lee have also compared their results with an approximate quasi-one-dimensional model relating the mass divergence to the wall porosity [28, 29]. As was discovered in the later work of Chao *et al.* [26] and Camargo *et al.* [27] in narrow channels, they found a relatively good agreement between experiment and theory for the more regular mixtures, while the limits were found to be systematically over-predicted in more unstable detonations.

1.2.4 Detonations with weak confinement

The influence of mass divergence on detonations is also central in problems of detonations with weak confinement. When the detonations propagate in a condensed explosive, the confinement always yields to the very high pressures generated in the reaction zone [30, 31, 32, 33]. In gases, the same problem arises when a reactive charge is weakly confined by an inert gas [32]. In this context, recent simulations of Li *et al.* [34] further revealed the role played by the three-dimensional non-homogeneities. They found that the presence of density non-homogeneities promoted the detonation propagation, although no attempt was made to model these effects in a global sense.

1.2.5 Detonations with friction and heat loss

Gaseous detonations in channels that exhibit large velocity deficits due to momentum and heat transfer losses due to wall roughness or obstacles have been extensively studied [35, 36, 37, 38, 39, 40, 5]. Propagation rates as low as 50% of the ideal speed have been reported. As might be expected, the incorporation of heat losses sets up a competition between heat production and extraction which can lead to detonation quenching [35, 37, 36]. The influence of frictional losses is also central to the propagation mechanism of detonation waves in tubes with embedded obstacles. The global wave propagation mechanism, has been reported to consist of detonation failure caused by flow diffraction around obstacles followed by local re-initiation at Mach stems formed by shock wave-obstacle interactions [38, 39, 40]. Makris reports that the dynamics is governed by the reactivity of the detonable mixture and by the obstacle's size [39, 40].

In the same context, the influence of instabilities on the detonation response to heat and frictional losses has been addressed in a recent study by Sow and co-workers [41]. They conducted numerical simulations of pulsating one-dimensional detonations in the presence of volumetric heat and frictional losses. They found that the predictions made without accounting for the pulsating instabilities under-predicted the velocity deficit. The extinction limit predicted by a quasi-steady model over-predicted the amount of loss necessary for extinction. This is the opposite trend to that observed experimentally for multi-dimensional detonations as discussed above. It is presently unclear whether this result is due to the assumption of one-dimensional flow, albeit a pulsating one. These observations further suggest the role of the pulsating dynamics in controlling the limits.

1.2.6 Necessity of a well-posed experiment to evaluate cellular structure influence on limits

Previous attempts to compare the predictions made by steady quasi-one-dimensional models with experiment strongly suggest that these models do not capture the dynamics in strongly unstable mixtures, as reviewed above. For weakly unstable mixtures, the agreement is deemed good. Some ambiguities still remain. They are associated with the difficulty to precisely quantify and model the loss mechanism in the experiments. This in general renders the comparison more qualitative than quantitative. In thin tubes and channels, mass divergence losses to boundary layers are also associated with complex flow in the boundary layers themselves. This is further complicated by momentum and heat losses in the boundary layer flow itself, which have not been considered in the analyses

of Chao *et al.* and Camargo *et al.* [26, 27].

In the experiments with porous walls, the pores act to attenuate the transverse waves, making the evaluation of the loss mechanism more difficult. Similarly, modeling of the boundary flow near the porous walls attempted by Radulescu and his collaborators was very approximate [28, 29, 42]. In very recent numerical simulations of cellular detonations in porous wall tubes [42], significant discrepancy was found with experiment. Thus, numerical simulations of these problems also suffer from the approximate nature of boundary conditions as do the steady wave models.

The model applicability is also questionable, as it pertains to the assumption of uniform curvature along the front, implying uniform area divergence for each streamline. A curved detonation due to wall boundary layers or permeable walls is not expected to have a unique curvature, as demonstrated by Chinnayya et al. numerically [24]. Further away from the axis of the channel or tube, the flow divergence departs from that along the streamline along the axis. For this reason, the models assumed previously only hold for weakly curved fronts, away from the limits. Whether the models agree or not for the limits and velocity deficits may be coincidental.

For these reasons, it is desirable to formulate a well-posed problem in which the loss mechanism and boundary conditions can be easily accounted for. This would permit one to unambiguously compare the results of the experiments with simulations and analytical models in order to evaluate the utility of the global models for detonation dynamics. This is the goal of the present thesis.

1.3 Problem definition

The exact governing equations in multiple dimensions for a N-component system, which neglect transport terms, are the so-called reactive Euler equations. In the reactive Euler equations, conservation of mass, momentum and energy following the path of a fluid particle are:

$$-\frac{1}{\rho}\frac{D\rho}{Dt} = \nabla \cdot \mathbf{u} \tag{1.1}$$

$$\rho\frac{D\mathbf{u}}{Dt} = -\nabla p \tag{1.2}$$

$$\frac{De}{Dt} = -\frac{p}{\rho^2}\frac{D\rho}{Dt} \tag{1.3}$$

where ρ, $\mathbf{u}$ and p denote the fluid density, velocity vector and pressure, respectively. Also $D/Dt = \partial/\partial t + \mathbf{u} \cdot \nabla$ is the material derivative and the symbols have their usual meaning [43]. These need to be complemented by an appropriate equation of state for the internal energy e of the form:

$$e = e\left(p, \rho, Y_1, Y_2, ..., Y_i, Y_N\right) \tag{1.4}$$

and the appropriate kinetics for the evolution of the mass fractions of each of the system's components:

$$\frac{DY_i}{Dt} = \frac{\omega_i}{\rho} \tag{1.5}$$

When a quasi-one-dimensional formulation is sought in a duct (or streamtube) of cross-section $A(x)$, the variables take the meaning of transverse averages (or streamtube variables) and the equations remain unchanged, with $D/Dt = \partial/\partial t + u\partial/\partial x$. The divergence of the velocity field in the continuity equation ((1.1)), which describes the rate of volume change of a fluid element per unit volume, can be expressed as two contributions. The first is the usual rate of strain of a fluid element in the flow direction x, and the second is the rate of strain in the transverse direction [43]:

$$\nabla \cdot \mathbf{u} = \frac{\partial u}{\partial x} + u\frac{d(lnA)}{dx} \tag{1.6}$$

The last term plays a fundamental role in gasdynamics[3], as it provides a rate of expansion or compression of a fluid element due to geometrical effects. In this research, we will deal with flows for which the source term appearing in the quasi-one-dimensional formulation for a streamtube or in a tube of cross-sectional area $A(x)$, namely:

$$K \equiv \frac{d(lnA)}{dx} \tag{1.7}$$

is a *constant*. The source term being a constant permits us to establish a steady (on average) detonation structure, as can be anticipated since the source is neither a function of space nor time. In the current work, we study the dynamics of detonations in a channel with a constant logarithmic derivative K, i.e., a channel with a cross-section varying exponentially with distance (see Figure 1.3). This is also known as an *exponential horn* in acoustics. Since the loss is always constant in an exponential horn, steady state detonations (on average) can be established, as will be shown in this thesis. This provides a unique opportunity to compare experimental results with steady state global models and numerical simulations and to draw conclusions from the various hypotheses and assumptions in each class of models.

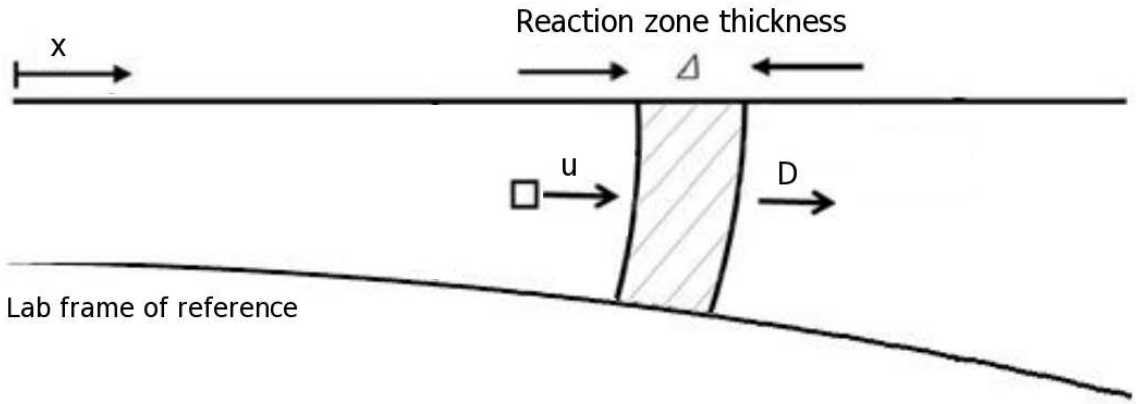

Figure 1.3: Schematic of a detonation wave with reaction zone thickness of Δ and speed of D propagating in a diverging channel and the quasi-one-dimensional flow behind it.

1.3.1 Reactive mixture selection

The experiments were performed for two different mixtures so that they exhibit either weakly unstable or highly unstable cellular structures. In order to select appropriate gases, a survey was performed on the reactive mixtures used in past studies. For the experiments in mixtures characterized by piece-wise laminar reaction structures (i.e. weakly unstable), the oxy-acetylene mixture with argon dilution has been a frequent choice [44, 45, 26, 27, 28, 29]. Increasing the argon dilution the regularity of the cellular structure has also been reported to increase in this mixture [44, 45]. Therefore, many previous studies on detonation propagation with presence of losses have adopted oxy-acetylene with argon dilution as a candidate mixture for weakly unstable cellular structure. For example, Chao *et al.* [26] performed their experiments on detonation propagation in narrow tubes using $C_2H_2 + 2.5O_2 + 14Ar$. Other studies of detonation propagation with presence of losses like the ones by Camargo *et al.* [27] and Radulescu *et al.* [28, 29] have also conducted their experiments using $2C_2H_2 + 5O_2 + 21Ar$ as the choice of mixture with regular structure.

On the other hand, for experiments on mixtures characterized by highly irregular and unstable cellular structures, methane and propane mixtures have been adopted in past studies [46, 28, 27]. Therefore, based on these considerations and by doing some

preliminary kinetic calculations on the above list to assess whether the mixtures were sufficiently sensitive so that tests at low pressure would be possible (details presented in Chapter 6), the mixtures were chosen for the experiments as follows: oxy-acetylene mixture with 75 volume percentage of argon addition ($2C_2H_2 + 5O_2 + 21Ar$) for weakly unstable cellular structures and propane-oxygen mixture (C_3H_8+$5O_2$) for highly unstable cellular structures.

1.3.2 The influence of cellular structure on the dynamics

In order to investigate the influence of cellular instabilities on the detonation propagation, quantitative comparisons were made with the predictions based on a quasi-one-dimensional ZND model with lateral mass divergence. The dependence of the velocity deficits and limits on the amount of mass divergence for the two mixtures were compared with the predictions of the quasi-one-dimensional ZND model with lateral mass divergence. Since the ZND model neglects the cellular structure of the detonations, such a comparison would permit one to asses the influence of cellular structure on the dynamics of detonations with mass divergence. The experiments and the ZND model predictions were also compared with the results of numerical simulations of the two-dimensional inviscid cellular detonations. This sheds more light on the importance of cellular structure on the dynamics and it quantifies the discrepancies in the detonation predictions caused by ignoring the cellular structure.

1.3.3 Thesis outline

The thesis is organized as follows. Chapter 2 introduces the setup of the diverging channel experiments and explains the details of the experimental procedure used. Chapter 3 presents the results of the experiments performed in the diverging channel framework. Chapter 4 addresses the solution of the quasi-one-dimensional ZND model with lateral mass divergence for predicting the dynamics of quasi-one dimensional curved detonations. Chapter 5 presents the numerical simulation results of the cellular detonation dynamics in diverging channels. Finally, my discussions of the results and recommendations for future work are presented in Chapter 6. These are followed by two appendices. Appendix A provides the details of velocity measurements for all the experiments performed in the thesis. Appendix B presents the conversion between the scaling used in the numerical simulations of this thesis and the scaling used by Short and Sharpe [47], whose results were used for bench-marking the present code.

Chapter 2

Experimental setup and technique

2.1 Overview

This chapter describes the details of the experimental setup used in the thesis. The diverging channel framework for the experiments is introduced and the technique used for performing the experiments is described.

2.2 Flow facility

2.2.1 Shock tube setup

Figure 2.1 shows the schematic of the 3.4-m-long rectangular channel used for the experiments in this thesis [48, 49]. The channel is made of aluminum and referred to herein as the shock tube. The internal height and width of the channel are 203.2 mm and 19.1 mm respectively. This internal width was found to be the optimum value to suppress the transverse perturbations and thus approximate the detonation cellular dynamics as two-dimensional [48].

As can be seen in Figure 2.1, the tube has three identical sections. The third section of the channel is equipped with non-tempered glass panels allowing one to visualize the flow evolution. The ramp was therefore placed in this window section. To ignite the mixture a spark plug ignition system was installed in the first section of the shock tube. Pressure transducers were installed along the top wall to record the arrival of the detonation wave and to monitor its strength. The actual experimental setup assembly in the lab is also illustrated in figure 2.2.

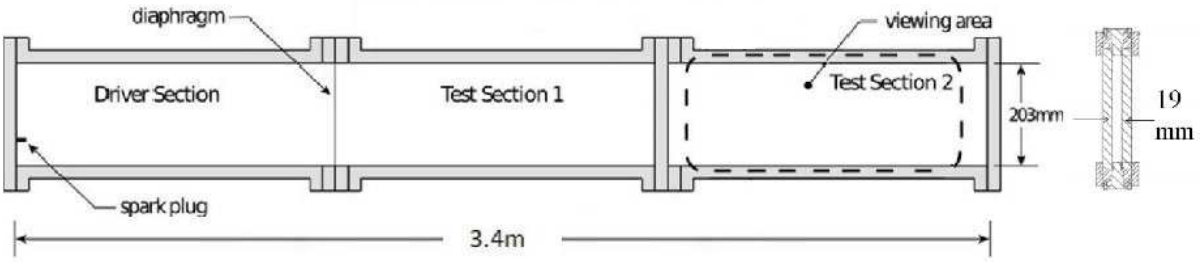

Figure 2.1: A schematic showing dimensions, driver section, test sections and ignition equipment of the experimental setup referred to herein as the shock tube.

Figure 2.2: Photograph of the actual shock tube setup assembly in the lab

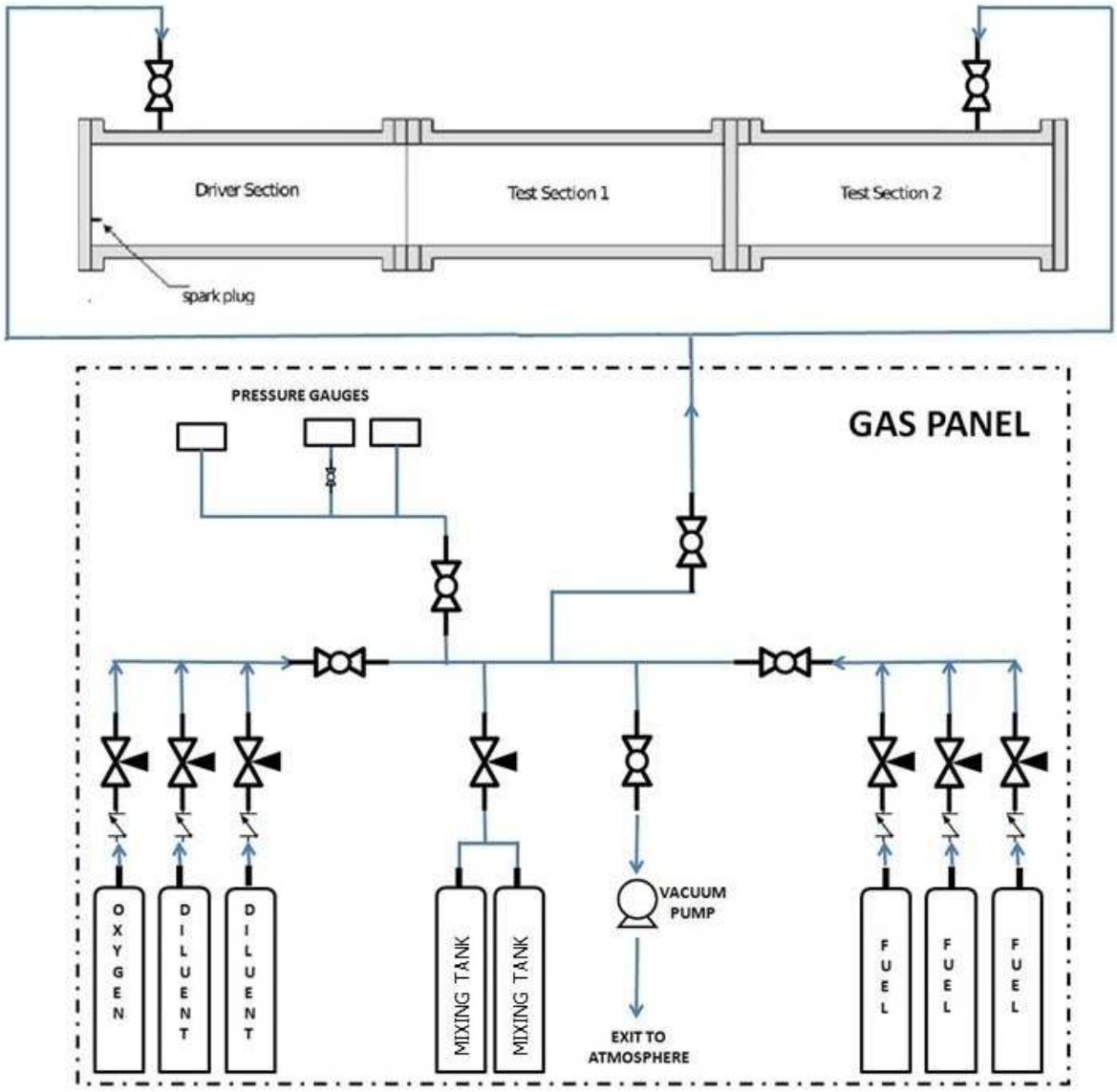

Figure 2.3: A schematic diagram of the gas line connections between the shock tube and its gas panel showing the direction of the gas flow.

Figure 2.3 is a schematic diagram of the gas panel used along with the shock tube for preparing the test mixture, filling and purging of shock tube channel. The Swagelok needle valves on the bottom right corner are connected to different fuels while the oxygen (O_2) line was connected to the needle valve on the bottom left. Additional valves were installed to avoid any reverse-flow or accidental mixing. The absolute static pressure in the shock tube was monitored by two OMEGA DPI32 programmable digital meters. The vacuum pressure in the shock tube was also measured using an OMEGA DVG-64 vacuum gauge [48]. The test mixture was fed into the shock tube from the mixing tanks, via the gas panel, through Swagelok rubber insulated gas lines. The test mixture was prepared by the method of partial pressures in the mixing tank and left to stand for approximately 24 hours. Ball valves connected onto the shock tube were used to seal either a section or to isolate the entire shock tube from the gas panel. Before performing each experiment, the shock tube was evacuated to 80 Pa using a Varian DS602 1PH rotary vane pump to purge the shock tube of residual gas products that might have been left behind from the previous experiment.

2.2.2 Diverging section geometry

Using the above mentioned experimental setup, a diverging section was adopted for the experiments. The cross-sectional area of the diverging geometry $A(x)$ varied exponentially with distance. Two geometries were tested. A long ramp (with a 1-m-length and $K = \frac{1}{A}\frac{dA}{dx} = 2.302\ m^{-1}$, see Figure 2.4) and a short ramp (with a 0.5 m length and $K = \frac{1}{A}\frac{dA}{dx} = 4.605\ m^{-1}$, see Figure 2.4) were designed and manufactured with PVC to make the diverging channel. Figure 2.5 shows the actual diverging geometry assembled by mounting the ramps separately in the viewing section of the shock tube.
In the experiments, a detonation wave was generated in the mixture of interest and propagated along the diverging section. In order to study the dynamics of the wave, a movie of the detonation wave propagating and its trailing reaction zone was recorded for each experiment.

2.3 Methods for gas ignition

The two following methods were used in my research to initiate a detonation wave by igniting the test mixture inside the shock tube.

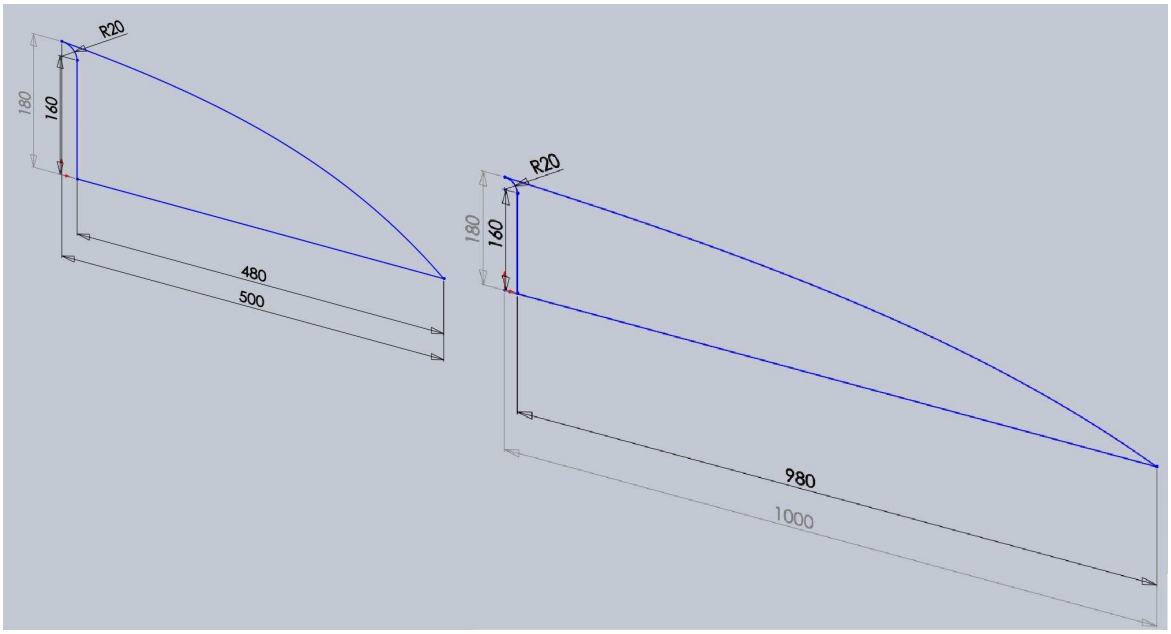

Figure 2.4: Dimensions of the two ramps with exponential rate of area divergence designed for the experiments (measures in units of millimeters).

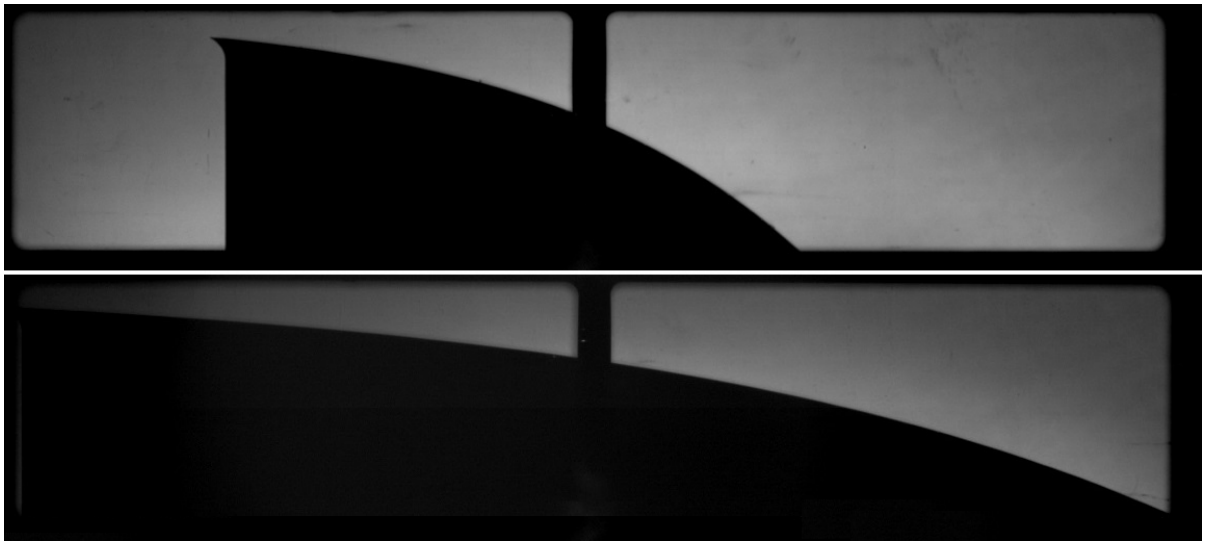

Figure 2.5: Pictures of the small and large ramp with exponential rate of area divergence mounted in the viewing section of the experimental setup.

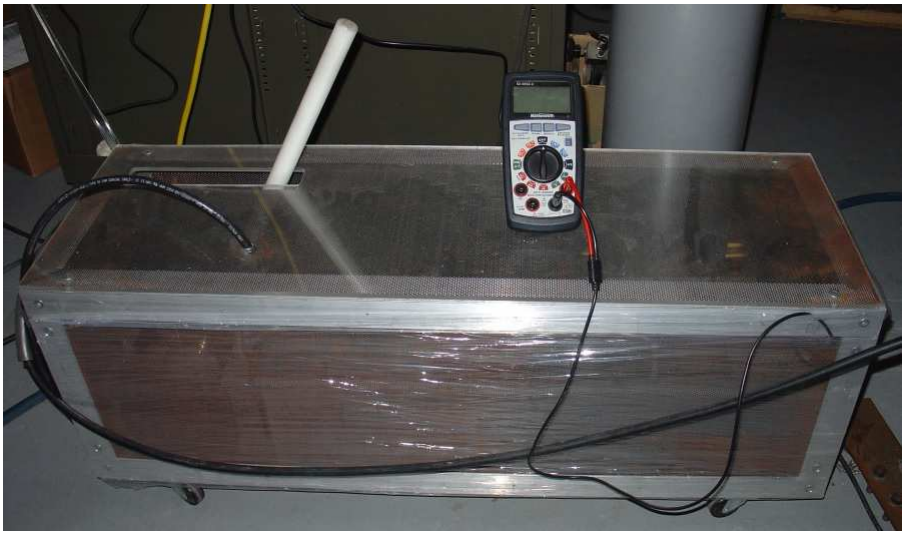

Figure 2.6: Photograph of the High Voltage Igniter (HVI) system used to ignite the mixture.

2.3.1 High Voltage Ignition (HVI) method

In the first method, a high voltage igniter (HVI) shown in Figure 2.6 was used. The HVI is a compact ignition system built by Sev Kamensikh from McGill University. It consists of a capacitor bank, operating at a maximum voltage of approximately 30 KV [48, 49]. The HVI system includes two 1 μF capacitors, a triggered spark gap and a trigger module. A voltage signal is sent to the trigger module by a pulse generator. This signal triggers the spark gap and discharges the capacitors into the mixture. The unit is capable of storing up to approximately 1000 J (at a charging voltage of $V_0 = 32\ kV$) of nominal energy and releasing it with a response time of less than 2 μs. Additional details can be found in Bhattacharjee's thesis [48].

After the HVI capacitors discharge their load into the mixture, a strong blast wave is generated followed by a high speed deflagration wave. A wire-mesh installed near the spark plug (see Figure 2.7) induces turbulence into the generated deflagration wave and accelerates it. The acceleration then leads to the deflagration-to-detonation (DDT) transition phenomenon [5] and an over-driven detonation wave is generated. The over-driven detonation wave then stabilizes to a CJ detonation wave before reaching the viewing section of the shock tube.

Figure 2.7: A photograph of the wire-mesh used to accelerate the flame generated by the HVI and cause a detonation wave.

2.3.2 Shock tube with a diaphragm method

Less reactive mixtures require high ignition energy to initiate a detonation wave. Therefore, a detonation wave can not be established in such reactive mixtures using the HVI method. This occurs especially for low pressure mixtures. In such cases when the HVI system could not initiate a detonation wave in the test mixture, a different method using a driver gas mixture was used. Accordingly, this experimental setup was equipped with a driver section (see Figure 2.1) filled with a more easily ignited mixture (e.g., stoichiometric oxy-ethylene $C_2H_4 + 3O_2$). The driver section was separated from the test section which was filled with the test gas, using a plastic diaphragm having an average thickness of roughly 80 μm.

The driver gas was ignited as described above using the HVI, leading to a detonation in the driver gas. The generated detonation wave ruptured the diaphragm and was transmitted into the test section as a strong shock wave. This strong shock wave transitioned into a CJ detonation wave before reaching the window section of the shock tube.

2.4 Experimental procedure

2.4.1 Experiments with driver mixture

In the experiments with a driver mixture, the shock tube and all the gas lines connecting the mixing tanks, shock tube and the gas panel were first purged by evacuating them to 80 Pa. After achieving the desired vacuum pressure, the test section was sealed and the driver section was filled with the driver mixture chosen (stoichiometric oxy-ethylene $C_2H_4 + 3O_2$). This was done by controlling the flow from the needle valve on the gas panel. In this step, the pressure difference across the diaphragm was restricted to be less than 20 kPa (abs) to minimize the risk that the plastic diaphragm would rupture. After reaching the desired pressure in the driver mixture, the driver section was sealed by closing the corresponding valves. All gas lines were then purged by evacuating them to a pressure less than 60 Pa. This helped in avoiding any mixing between any residual driver gas in the lines and the driven mixture. The test section was then filled with the mixture of interest to study. After reaching the desired pressure in the test mixture, the shock tube was then completely sealed and isolated from the gas panel. All the gas lines were once again evacuated to a pressure of less than 60 Pa. The HVI was charged to 24 kV and the ignition was performed as described in section 2.3.2.

2.4.2 Experiments with High Voltage Ignition

In the experiments with the High Voltage Ignition technique, the shock tube and all the connection lines between the shock tube, gas panel and the mixing tanks were first evacuated to 80 Pa. The shock tube was filled with the test mixture of interest. This was done by controlling the gas flow from the needle valve on the gas panel. After reaching the desired pressure, the shock tube was sealed and isolated from the gas panel. All the gas lines were evacuated to a pressure of less than 60 Pa. The HVI was charged to 24 kV and the ignition was performed as described in Section 2.3.1.

2.4.3 Sensitivity of the reactive mixture

In the experiments performed, the sensitivity of the test mixtures ($2C_2H_2 + 5O_2 + 21Ar$ and $C_3H_8 + 5O_2$) was controlled by keeping the composition and temperature constant and changing only the initial pressure. Increasing the pressure (and consequently the density) makes the reaction rates faster and the mixture more sensitive. Previous cor-

relations have shown that the reaction zone thickness and cell size of reactive gases are almost inversely proportional to the initial pressure [50, 28]:

$$\Delta_{1/2} \propto \lambda \propto P_0^{-a} \tag{2.1}$$

where $\Delta_{1/2}$ represents the half-reaction length defined as the distance behind the shock front to the point where half of the energy is released in a ZND model framework. Also, λ denotes the characteristic cell size of the gas mixture.

2.5 Flow visualization

2.5.1 The shadowgraph system

The optical system used for visualization of the flow was a large-scale shadowgraph system adopted from Dennis *et al.* [51]. The shadowgraph technique is a simple form of optical system suitable for observing a flow exhibiting variations of density [51, 52]. In principle, we cannot directly see a difference in temperature, density, or a shock wave in the transparent gas mixture. However, all these disturbances refract light rays, so they can cast shadows. Figure 2.8 shows the schematic of the shadowgraph assembly used for the experiments. The shadowgraph technique employs a light source and a recording plane (Figure 2.8). The mixture is exposed to the light beam coming from the light source. The refracted light rays are then projected on the recording plane [51, 52].

The retro-reflective screen used had a 2 m by 2 m dimensions, allowing visual access to the experiments over the entire 1 m of the viewing section. The shadowgraph system was used by placing the shock tube at $d/f = 1/2$ to obtain the clearest images. The collimated light exiting from the arc lamp was condensed to a 3-5 mm point using a 50-mm-focusing glass lens. This point was then focused onto a 10-mm-diameter cylindrical rod mirror cut at a 45^o angle. The mirror then projected the light onto the retro-reflective screen as if it directly emanated from the camera lens, increasing the luminosity of the returned image to the camera [51, 49].

A 1600 W continuous xenon arc lamp, made by Newport, and a Phantom v1210 high-speed video camera, made by Vision Research, recorded the high-speed videos for the experiments. The 42496 frame per second (fps) rate and 42049 fps rate of the camera with a 1 μs exposure were used in the experiments.

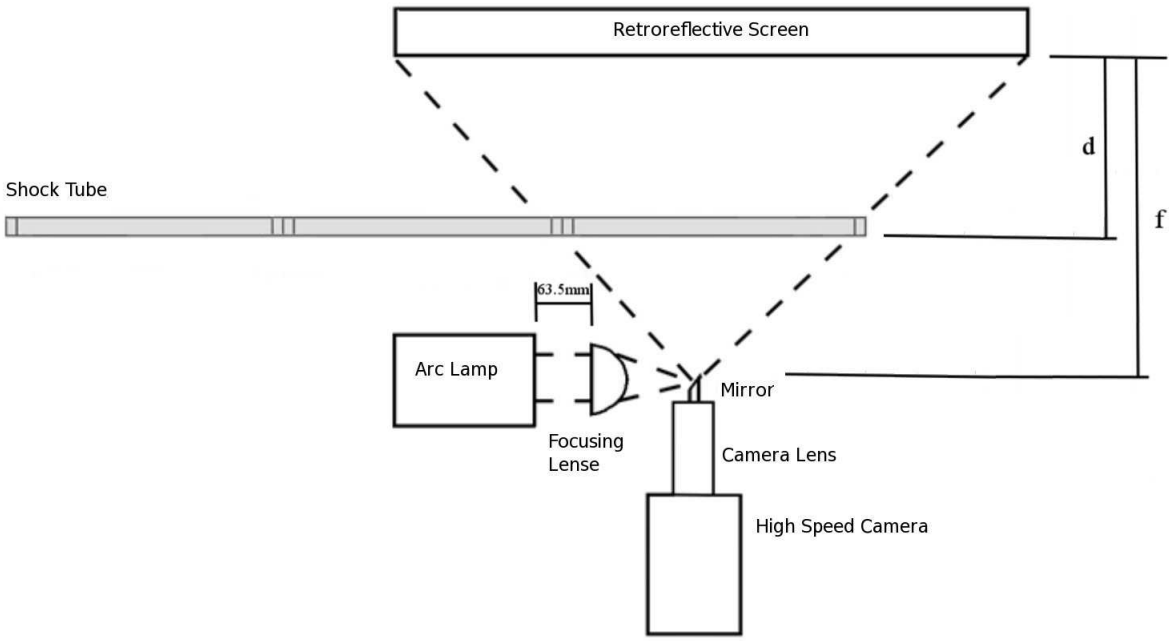

Figure 2.8: Schematic of the shadowgraph setup including the arc lamp, retroreflective screen focusing lenses and the camera, used in the experiments for visualizing the flow evolution.

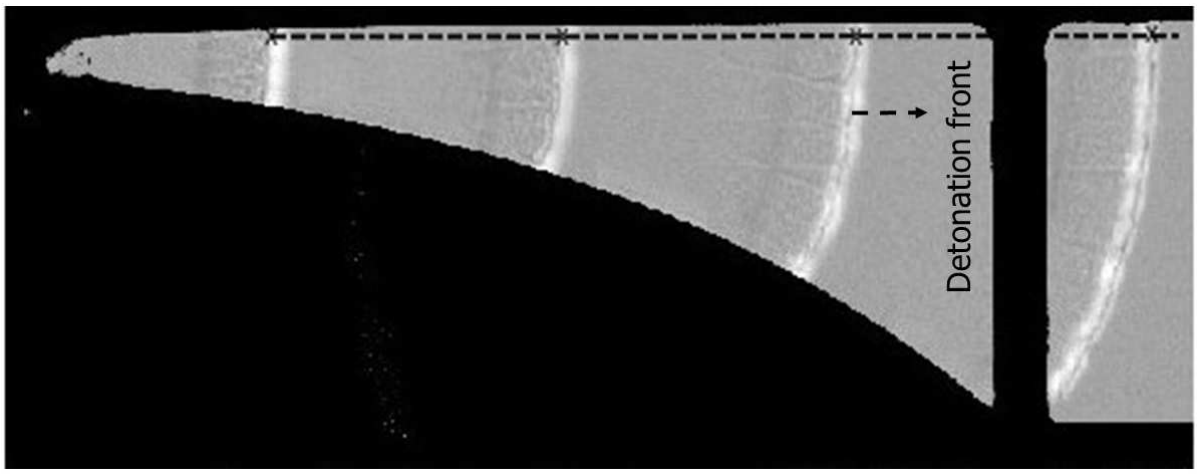

Figure 2.9: Superposition of detonation wave shadowgraph pictures at different time intervals used to detect the location of shock front along the top wall.

2.6 Data reduction technique

In order to study the dynamics of the detonation wave, velocity measurements were performed using the videos taken from the experiments. In this regard, the location of the detonation front was detected in all of the video frames along the top wall. For example Figure 2.9 shows some frames of the video taken for an acetylene experiment along the short ramp that have been put beside each other in a composite image. In the experiment videos taken by the shadowgraph technique, the leading shock front is identified as a thick black line followed by a white band resulting from the chemi-luminescence of the gas particles. For the velocity measurement, the flow sufficiently close to the top wall is assumed to be parallel to it. Accordingly, the leading front (dark line) was detected in all the video frames, along the dashed line sketched parallel and sufficiently close to the top wall. The locations were detected in pixels and were then converted into physical distances by knowing a reference length scale in the pictures, such as the ramp length. The uncertainty of the measurement is also a result of the possible errors in determining the exact pixel of the shock location correctly. Therefore, in order to take this uncertainty into account, an uncertainty corresponding to a $\Delta x = 1$ pixel is considered for the measurements.

After obtaining the location of the shock front at each frame and in order to measure its velocity, the time interval between the frames was also needed. This was obtained

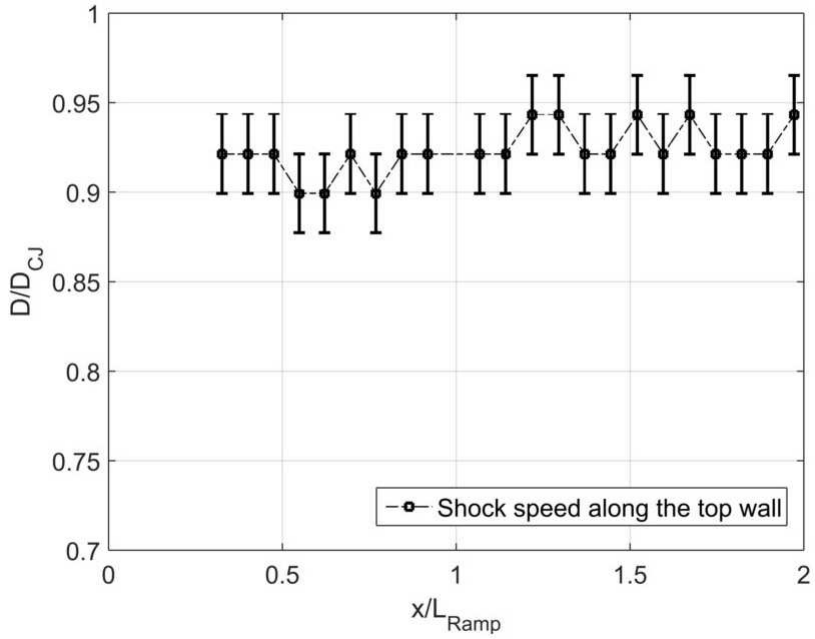

Figure 2.10: Shock speed variation along the top wall for the acetylene experiment at 13.8 kPa along the small ramp.

from the frame per second rate used for capturing the video. For example, if the video is recorded using a frame per second rate of 42049, then the time interval between two sequential frames is 1/42049 sec.

An example of the speed data is shown in Figure 2.10. The Figure shows the shock speed variation along the top wall non-dimensionalized by the CJ speed (the speed prescribed by Chapman-Jouguet theory for steady propagation of detonation waves [3]) for acetylene mixture at 13.8 kPa. Considering the error bars for the measurement, it can be seen that the detonation velocity remains relatively constant for this case. The calculation details of the data reduction technique for all other experiments are presented in Appendix A.

Chapter 3

Experimental results

3.1 Overview

This chapter presents the experimental results. The evolution of the detonation wave observed in the shadowgraph system for both mixtures is presented and the speed measurements performed for the detonation wave are reported.

3.2 Flow evolution results

3.2.1 Initial pressure ranges

Experiments were performed for decreasing pressures until a self-supported detonation wave could no longer be sustained in the diverging section. On this basis, both mixtures were tested with a wide range of initial pressures on the large and small ramps. The pressure ranges used for the experiments along with the corresponding method of igniting the gas at that pressure are reported in Table 3.1 for both mixtures.

Table 3.1: Initial pressure ranges used for acetylene and propane mixtures experiments

Experiment	HVI technique	Driver gas ignition technique
Large ramp-$2C_2H_2 + 5O_2 + 21Ar$	8.5-13.8 kPa	4.2-7.6 kPa
Small ramp-$2C_2H_2 + 5O_2 + 21Ar$	8.2-19.0 kPa	7.6-4.8 kPa
Large ramp-$C_3H_8 + 5O_2$	2.1-13.8 kPa	-
Small ramp-$C_3H_8 + 5O_2$	4.5-12.0 kPa	-

3.2.2 Acetylene mixture results

Large ramp experiments

Figures 3.1 (a),(b) and (c) show the evolution of the detonation wave propagation for three different experiments in an acetylene mixture with initial pressures of 13.8 kPa, 12.1 kPa, and 10.3 kPa, respectively. These pictures were obtained by overlaying the shadowgraph images of the detonation front at different locations along the ramp. As the detonation proceeds along the ramp, the area of the curved shock front increases. The pictures show the detonation wave propagating from left to the right in the diverging domain. The leading shock front is identified by the thick black line, followed by a very thin zone of high temperature and pressure where the chemical reactions occur. Accordingly, the bright band seen in the pictures very close to the shock front result from chemi-luminescence of the gas at high temperatures.

It can be seen that at these sufficiently high pressures, the detonation front is textured with a large number of small sized cells. Traces of the transverse waves starting from the triple points on the wave front, and extending toward the reaction zone are also observed. As the detonation progresses in the enlarging section, it acquires the expected curvature due to the geometrical divergence of the gases behind the front.

Figures 3.2 (a),(b) and (c) show the detonation wave evolution in additional experiments with lower initial pressures of 9.0 kPa, 8.6 kPa, and 7.6 kPa, respectively. In these experiments, the test mixture had a less rapid chemical energy release due to the lower initial pressure as compared to the tests shown in Figure 3.1. Consequently, the gas particles shocked by the front are influenced to a greater significance by expansion cooling than gas particles in the tests with higher initial pressures. Accordingly, as can be seen in Figures 3.2 (a),(b) and (c), a thicker reaction zone is observed for these lower pressure cases. The number of cells along the shock front is also reduced due to the enlargement in their size.

By continuing to decrease the initial pressure, the extinction limit was eventually reached. Figures 3.3 (a), (b) and (c) show the experimental results for the initial pressures of 6.2 kPa, 4.9 kPa and 4.2 kPa, respectively. In Figure 3.3 (a), (b), it can be seen that the reaction zone becomes thicker due to the reduced sensitivity of the gas. In Figure 3.3 (b), even some unburned gas pockets that have escaped from shock ignition can be seen. These pockets are more visible in the enlarged view of this picture shown in Figure 3.4.

Figures 3.3 (a) and (b) also show that the number of the cells along the shock front has decreased. In these pictures, only one main triple point is observed that experiences

reflections from the top wall and the ramp during the wave propagation. The transverse wave coming out of this triple point also looks stronger. In Figure 3.3 (b), a local detonation seems to be occurring about the transverse wave. This is shown in more detail in the enlarged view of this picture in Figure 3.4.

Finally, Figure 3.3 (c) shows that, after the pressure goes below the detonation limits of the mixture, a detonation wave can no longer be sustained. In such a case, the expansion cooling is sufficiently strong to significantly thicken the reaction zone and to decouple the shock front from the zone of energy release.

Small ramp experiments

Figures 3.5 (a), (b) and (c) show some sequential frames of the detonation propagation along the small ramp at pressures of 19.0 kPa, 17.2 kPa and 15.5 kPa in the acetylene mixture, respectively. All three pictures show that as the detonation wave propagates from left to the right in the diverging domain, the shock area supported by the heat release in the reaction zone increases. The fronts consist of a large number of small cells with their corresponding transverse waves extending behind the shock. Once again the bright band of chemical luminescence of the gas is apparent in the pictures.

Figures 3.6 (a), (b) and (c) show the images of the detonation front for slightly lower values of pressures. The pictures show a relative thickening of the reaction zone, especially in the later frames. The size of the cells in the detonation front has also increased when compared to the finer cells of Figure 3.5.

Figures 3.7 (a), (b) and (c) show the experimental results for lower initial pressures of 8.3 kPa, 7.6 kPa and 6.9 kPa, respectively. It can be seen that the size of the cells in the detonation front is larger. Strong transverse waves also start to emerge. The transverse waves help in reacting the shocked materials that may have not burned completely. These observations can be more easily seen in the enlarged view of 3.7 (a), presented in Figure 3.8.

Figures 3.9 (a), (b) and (c) also show the behaviour of the detonation wave in the test mixture, close to its extinction limit, corresponding to pressures of 6.2 kPa, 6.0 kPa and 4.8 kPa, respectively. Due to the larger rate of area divergence of the small ramp and the less rapid rates of energy release at such low pressures, a thick detonation wave can be seen to occur in even the early frames. In the later frames of Figure 3.9 (a) the transverse wave itself can be seen to transition into a detonation wave. This is shown more clearly in the enlarged view presented in Figure 3.10. The last frame of Figure 3.9 (b), shows the completion of chemical reactions happens a considerable distance away

from the leading front. Also, as shown in the enlarged view of this picture (see Figure 3.11), unburned gas pockets that have not ignited completely by the weakened shock have emerged. Finally in Figure 3.9 (c), the thick trailing reaction zone in the early frames completely decouples from the shock in the last two frames. In this picture, a single shock far from the last evidences of chemical reactions can be seen at the end of the ramp.

3.2.3 Propane mixture results

Large ramp experiments

Figures 3.12 (a), (b) and (c) show the evolution of the detonation wave structure at 13.8 kPa, 12.1 kPa and 10.3 kPa in the propane mixture, respectively. The fronts look very similar in all three pictures. The curved dark line with a large number of very fine ripples represents the detonation front and its cellular texture that experiences an increase in area as propagation continues along the ramp. The chemical luminescence of the propane mixture is observed in the experiments from the high intensity of the bright band of light behind the detonation front.

Figures 3.13 (a), (b) and (c) illustrate the flow field at lower initial pressures of 8.6 kPa, 6.9 kPa and 5.2 kPa, respectively. The changes in the front's appearance are readily observed in pictures (b) and (c). At this point, some larger sized cells start to appear along the shock front.

Figure 3.14 shows that the extinction limit is eventually satisfied by a more substantial decrease in the initial pressure. Figures 3.14 (a) and (b) show the texture of the thickened front to consist of one or two large cells. However, unlike the acetylene mixture, the transverse waves appear as non-reactive near the limit. Instead, complex shear flow with finely textured unreacted pockets are observed. This can be seen more easily in the enlarged view shown in Figure 3.15. Figure 3.14 (c) also shows that as the detonation propagates along the ramp, the distance between the shock front and the points where reactions are completed gets larger until the shock and reaction zone completely decouple as shown in the last frame of this sequence.

Small ramp experiments

A similar sequence of events was also observed in the experiments performed with the small ramp. Figures 3.16 (a), (b) and (c) depict the detonation wave in the propane

mixture at initial pressures of 12.1 kPa, 10.3 kPa and 8.6 kPa passing along the short ramp. At these sufficiently high pressures, the reaction rates of the gas are still high and the chemical energy release is able to compete with the expansion cooling. Therefore, no substantial change is observed either in the thickness of the reaction zone or in the texture of the front.

Figures 3.17 (a) and (b) show that at lower pressures of 6.2 kPa and 5.5 kPa, a main big cell with one or two triple points are governing the dynamics of the front. The transverse wave behind the triple point is also clearly seen in Figure 3.17 (b). However, unlike the acetylene mixture experiments, the transverse wave appears as non-reactive. This is shown in more detail in the enlarged view of Figure 3.18. Additionally, the flow behind the shock also has a more complex pattern when compared to the acetylene experiments. Finally, after passing the extinction limit at 4.5 kPa (Figure 3.17 (c)), the shock and reaction zone complex falls apart from each other. Consequently, the shock front in the last frame is observed as an inert shock that has been deprived of any cellular pattern.

3.2.4 Reproduciblity of the experiments

In order to verify the reproducibilty of the results, repeat experiments were performed for some of the experiments in both mixtures. A high, a mid-range and a close to limit initial pressure were selected for the repeat cases. The evolution of the detonation dynamics and the average speed were compared together in the repeat experiments and good agreement was observed. For example Figure 3.19 shows the results of three repeated experiments for propane mixture at initial pressure of 5.2 kPa along the large ramp. Likewise, Figure 3.20 shows the repeated experiments performed for propane mixture at its extinction limit along the large ramp. It can be seen that the evolution of the detonation dynamics and the pattern of cellular structure of the wave are similar in the repeated experiments shown in Figures 3.19 and 3.20 . For instance, Figure 3.20 shows that the texture of the thickened front at all the three repeated experiments consists of one or two large cells. Thickening of the reaction zone behind the detonation front is observed in all the three tests as the detonation propagates toward the end of the ramp. Appearance of non-reactive transverse waves and complex shear flow with finely textured unreacted pockets are also observed at the end of the diverging section.

In addition to comparing the cellular structure of the detonations in the repeated tests, data reduction and average speed measurement was also performed for each case

and the results are included and shown in the Section 3.3 and the quantitative comparison performed in Chapter 6.

3.3 Speed measurement results

The high speed videos illustrated in the previous section were analyzed in order to extract the front speed evolution, as explained in Chapter 2. In this regard, the technique described in Section 2.6 of the thesis was used to measure an average speed for the shock front along the top wall of the diverging domain. The summary of the measurement and analysis performed for the experiments are presented in Figure 3.21. In this figure, the average speeds measured for the experiments on the large and small ramps were plotted with respect to the initial pressure of the gas. The data for the CJ speed of the detonation wave for the corresponding initial pressures was also plotted to compare with the experiments. The CJ speed was found through calculations performed using the NASA CEA code [53]. The error bars for the plot were also prescribed by calculating the standard error of the speed at different locations along the ramp with respect to average speed measured for each experiment.

The Figure shows that, the shock speed decays for both large and small ramp experiments when the initial pressure is lowered. The shock speed also deviates from the CJ speed with a decrease in the initial pressure. This can be interpreted in terms of the gas sensitivity varying with the initial pressure. Mixtures with lower initial pressures are the ones with slower reaction rates and chemical energy release rate. Therefore, the expansion cooling experienced by the shocked gas particles due to the area divergence is able to decrease the shock strength and speed. Since the CJ speed represents the velocity of a steady detonation wave, the lower initial pressures result in more deviation from the CJ speed. The details of the calculations performed for each experiment to obtain the average speed and to construct the plots shown in Figure 3.21 is presented in Appendix A.

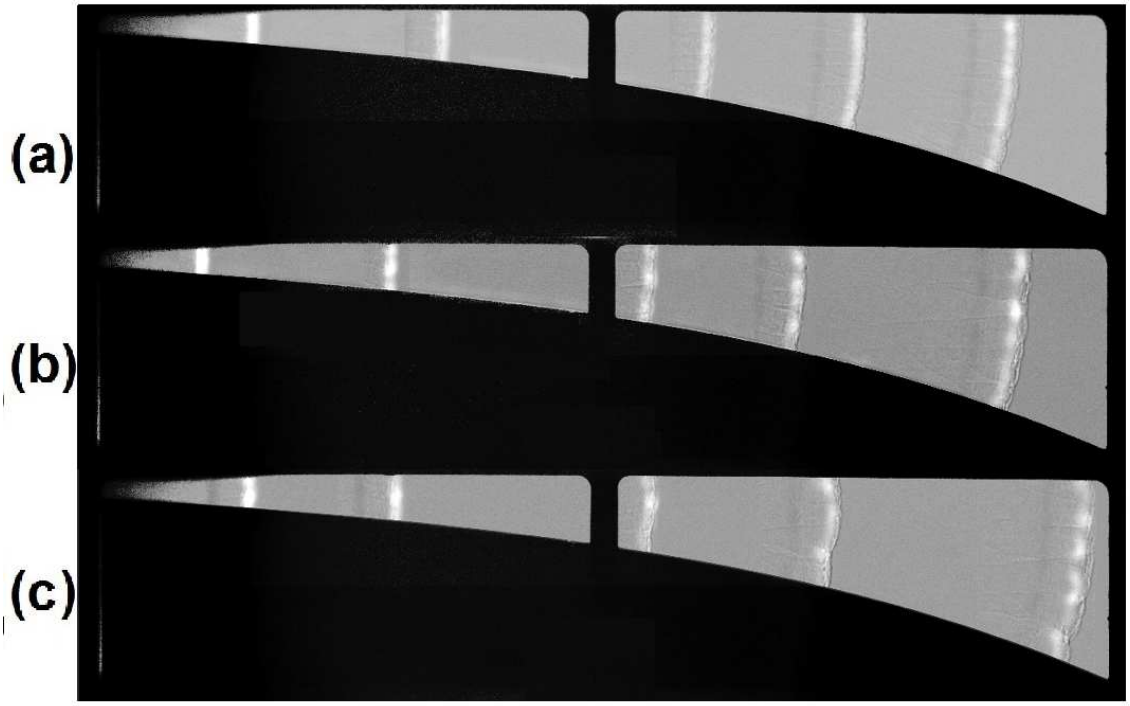

Figure 3.1: Shadowgraph images of detonation wave structure along the large ramp (1-m-length) at sequential time frames for $2C_2H_2 + 5O_2 + 21Ar$ mixture at (a) 13.8 kPa, (b) 12.1 kPa and (c) 10.3 kPa.

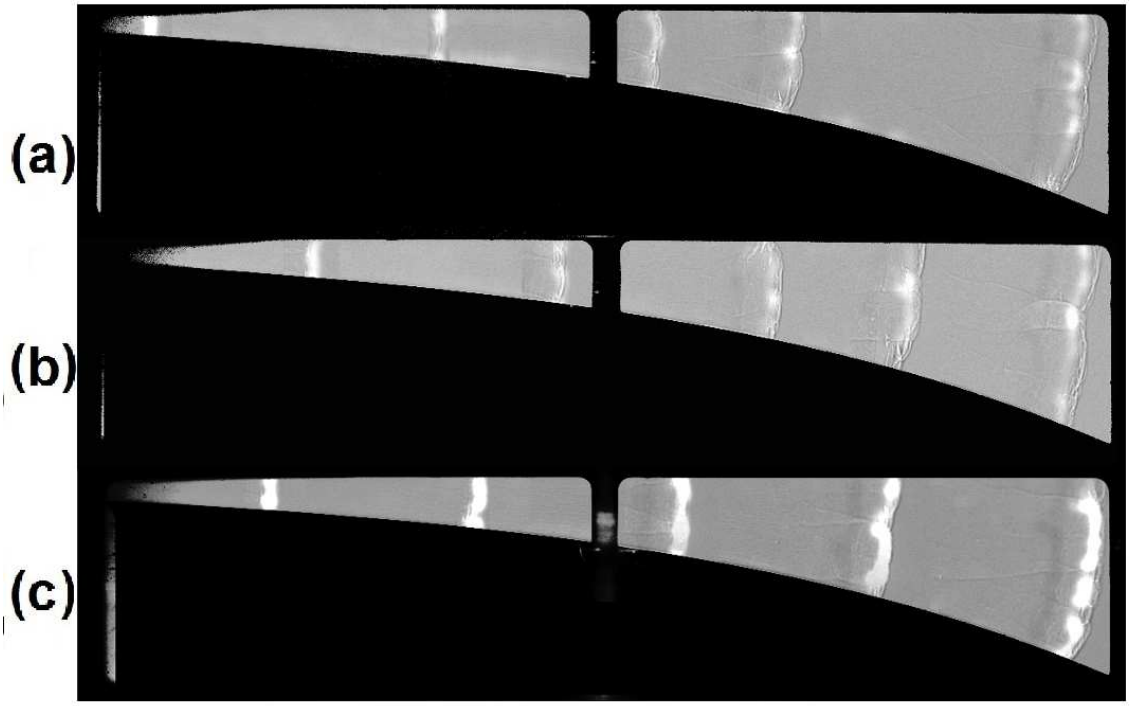

Figure 3.2: Shadowgraph images of detonation wave structure along the large ramp (1-m-length) at sequential time frames for $2C_2H_2 + 5O_2 + 21Ar$ mixture at (a) 9.0 kPa, (b) 8.6 kPa and (c) 7.6 kPa.

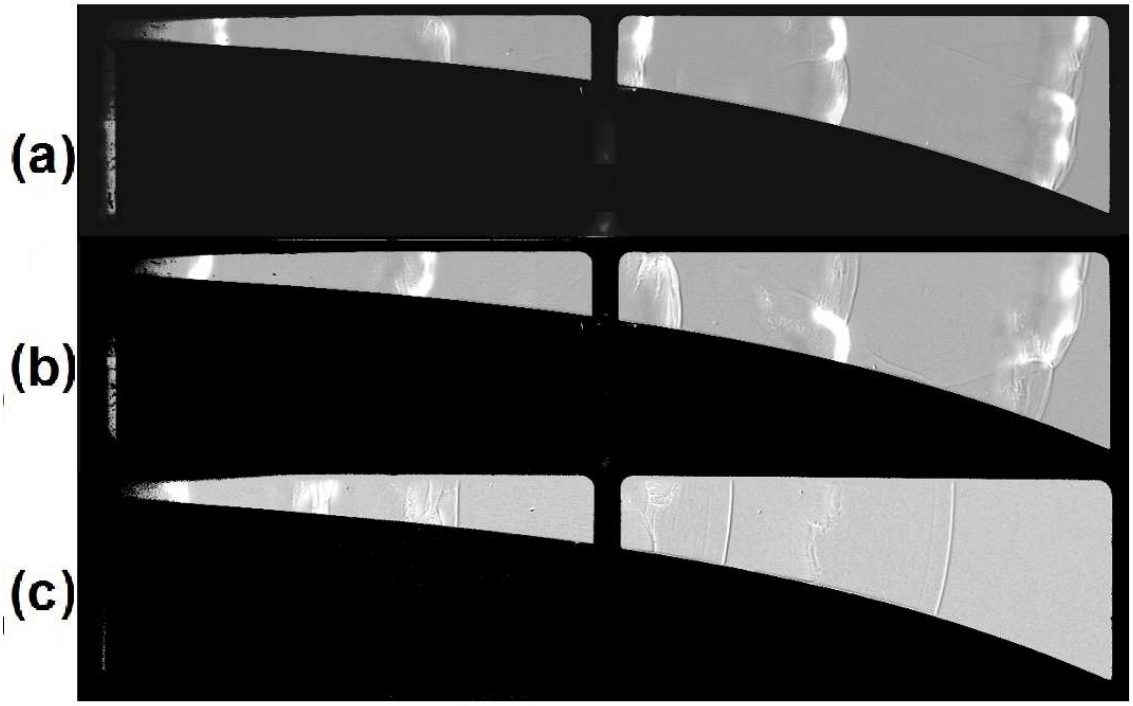

Figure 3.3: Shadowgraph images of detonation wave structure along the large ramp (1-m-length) at sequential time frames for $2C_2H_2 + 5O_2 + 21Ar$ mixture at (a) 6.2 kPa, (b) 4.9 kPa and (c) 4.2 kPa.

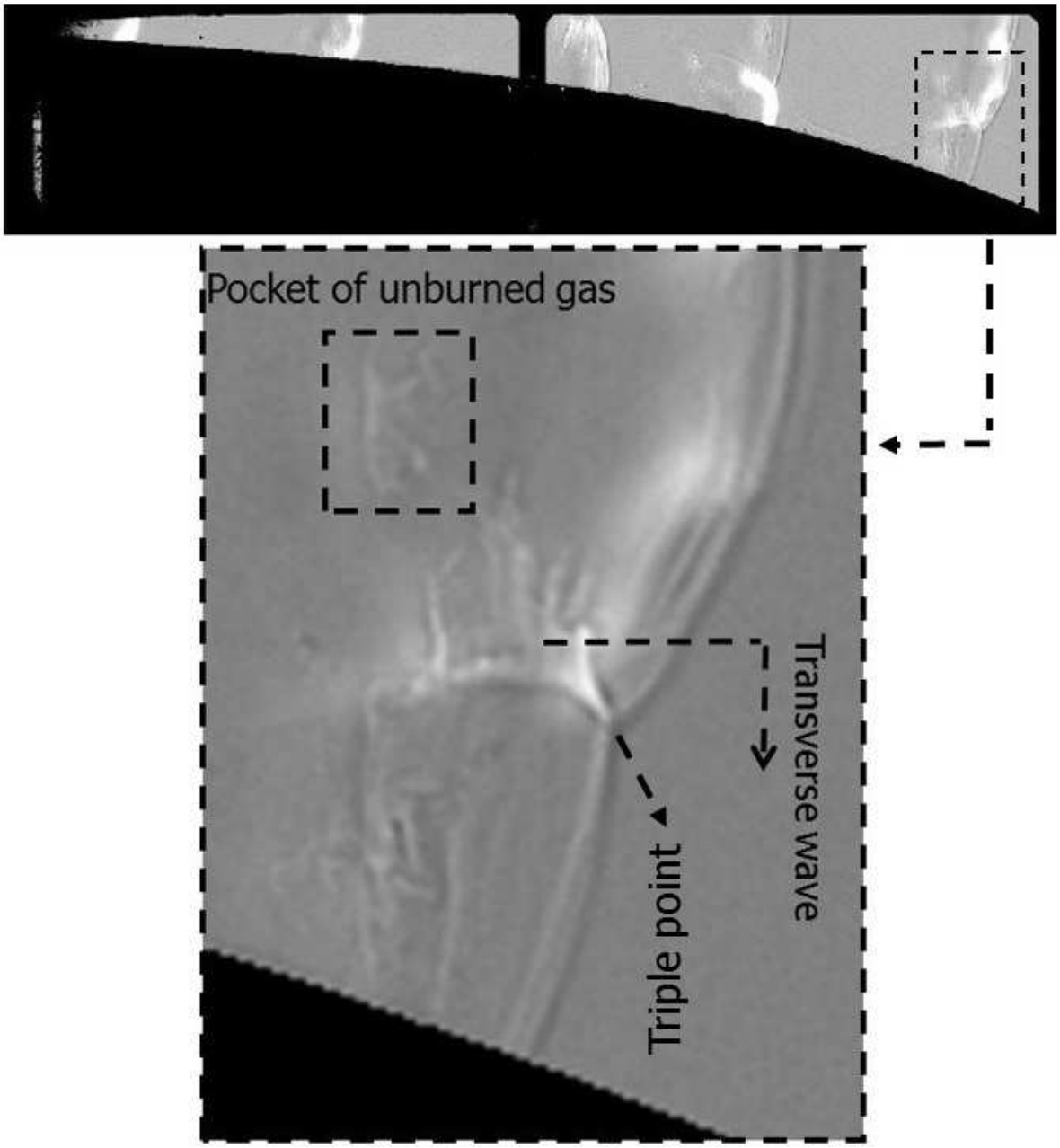

Figure 3.4: Strong transverse wave and pocket of unburned gas behind the detonation front for $2C_2H_2 + 5O_2 + 21Ar$ mixture at 4.9 kPa (an enlarged view with more details of Figure 3.3 (b)).

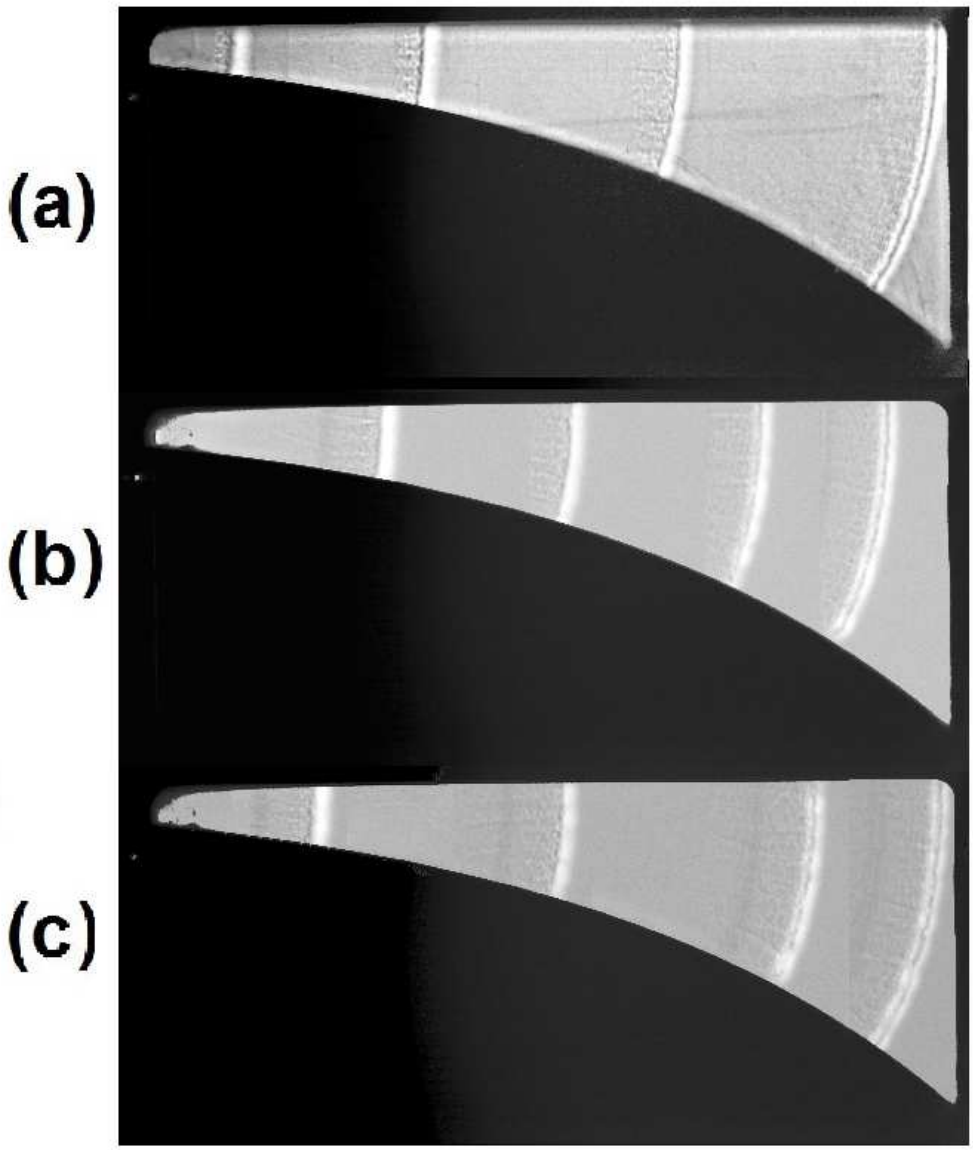

Figure 3.5: Shadowgraph images of detonation wave structure along the small ramp (0.5-m-length)at sequential time frames for $2C_2H_2 + 5O_2 + 21Ar$ mixture at (a) 19.0 kPa, (b) 17.2 kPa and (c) 15.5 kPa.

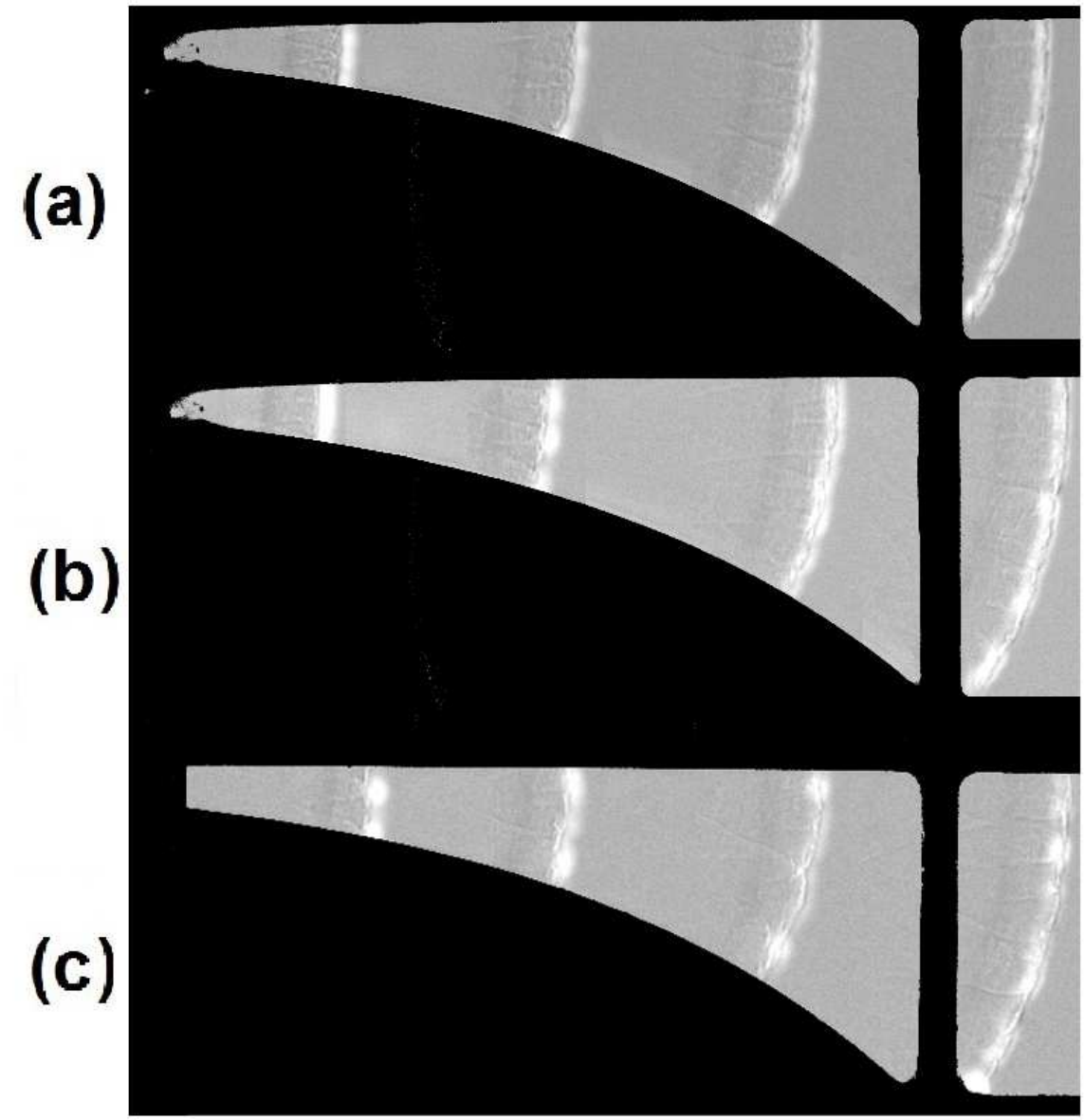

Figure 3.6: Shadowgraph images of detonation wave structure along the small ramp (0.5-m-length) at sequential time frames for $2C_2H_2 + 5O_2 + 21Ar$ mixture at (a) 13.8 kPa, (b) 12.1 kPa and (c) 9.0 kPa.

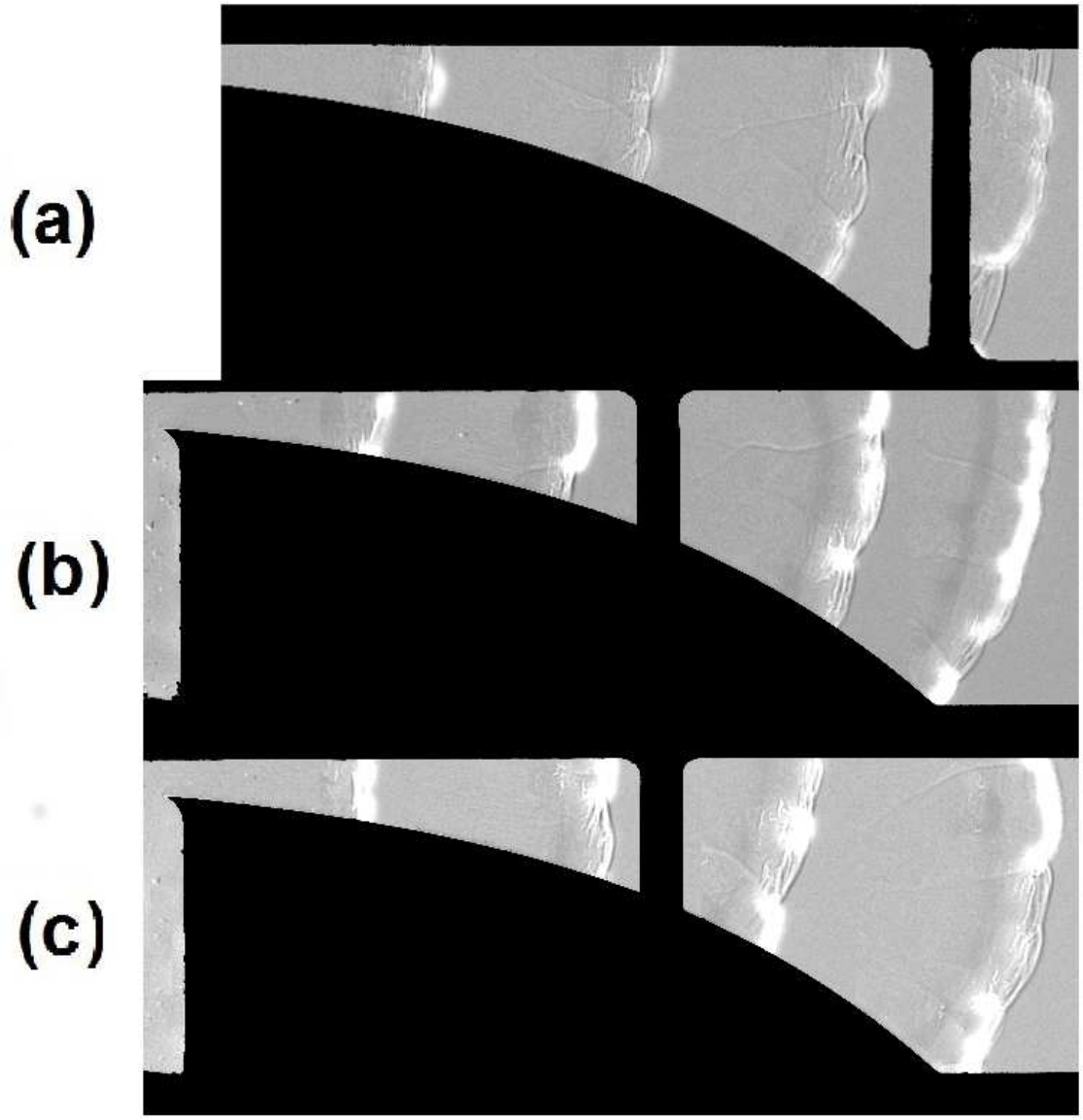

Figure 3.7: Shadowgraph images of detonation wave structure along the small ramp (0.5-m-length) at sequential time frames for $2C_2H_2 + 5O_2 + 21Ar$ mixture at (a) 8.3 kPa, (b) 7.6 kPa and (c) 6.9 kPa.

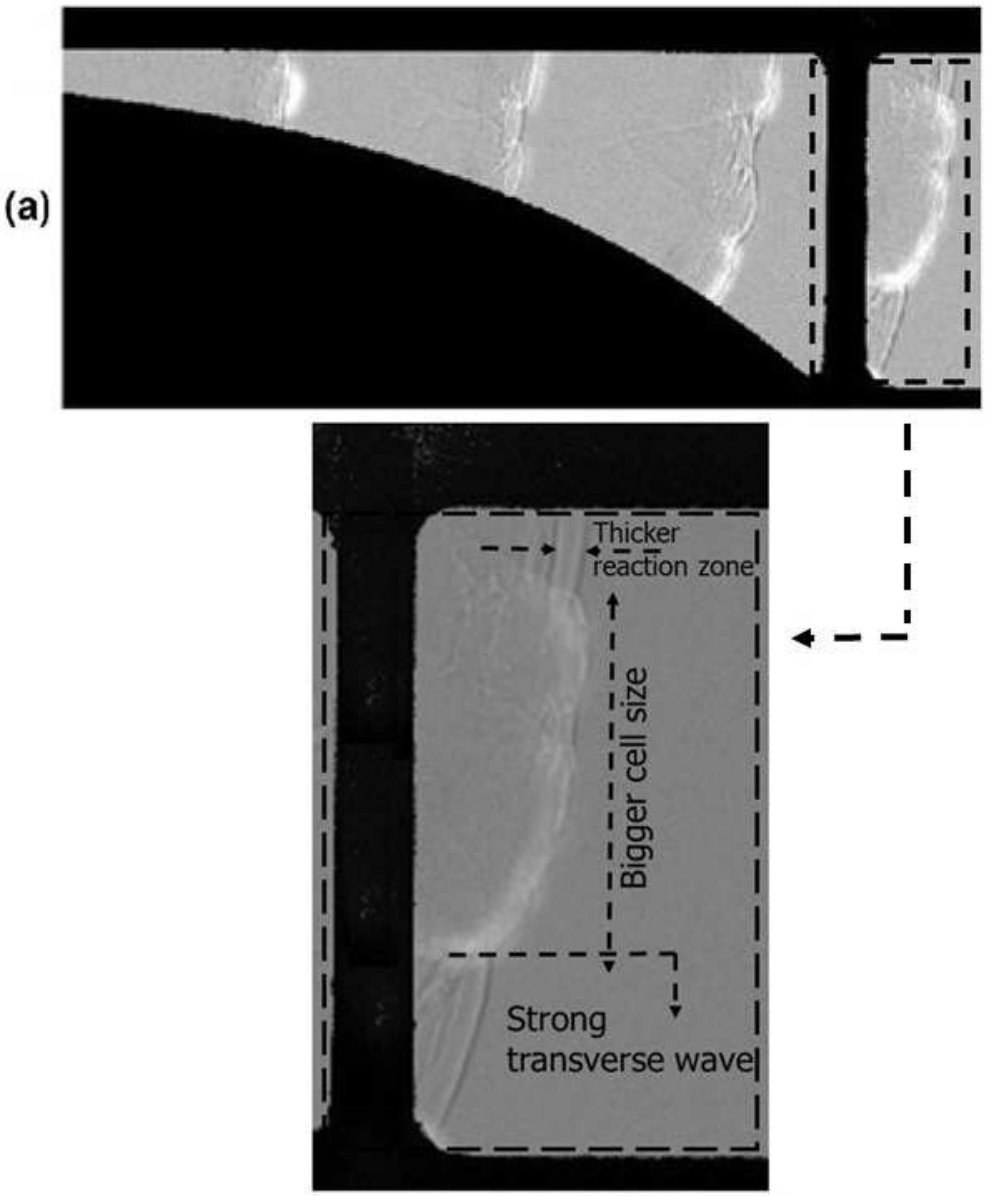

Figure 3.8: Strong transverse wave along with thick reaction zone and enlarged cellular structure for $2C_2H_2+5O_2+21Ar$ mixture at 8.3 kPa (an enlarged view with more details of Figure 3.7 (a).

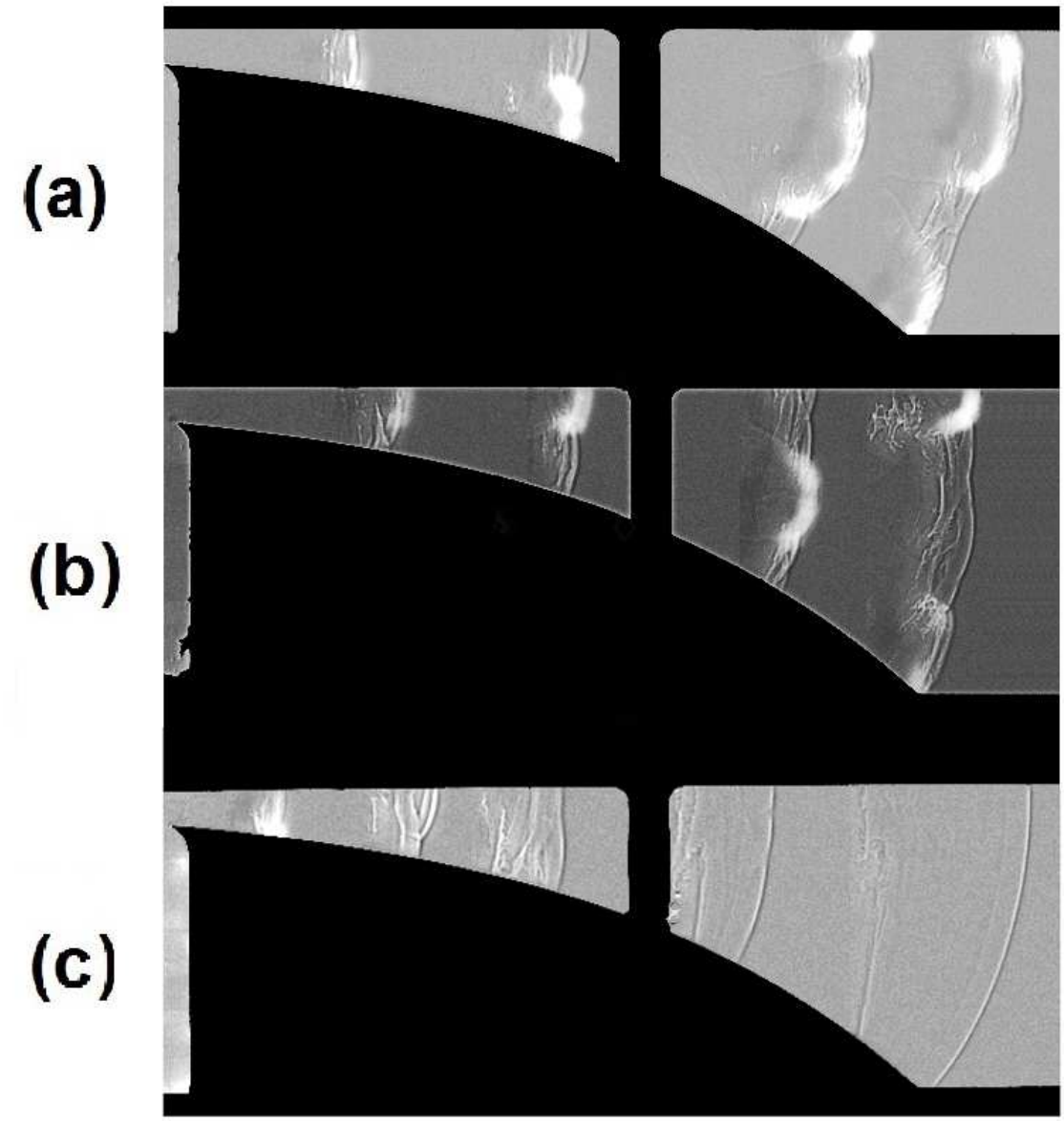

Figure 3.9: Shadowgraph images of detonation wave structure along the small ramp (0.5-m-length) at sequential time frames for $2C_2H_2 + 5O_2 + 21Ar$ mixture at (a) 6.2 kPa, (b) 6.0 kPa and (c) 4.8 kPa.

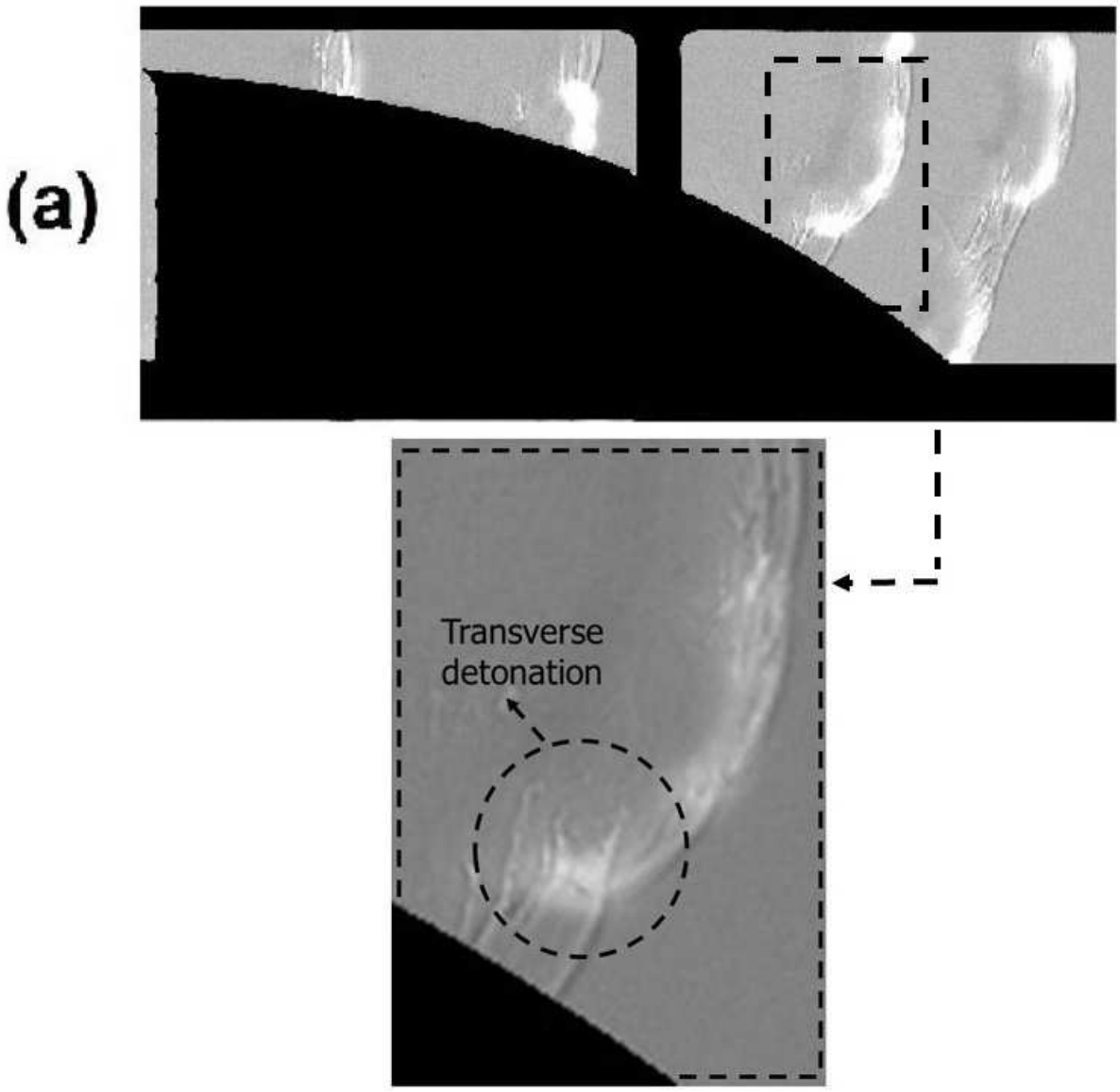

Figure 3.10: Transverse detonation wave happening at the triple point location for $2C_2H_2 + 5O_2 + 21Ar$ mixture at 6.2 kPa (an enlarged view with more details of Figure 3.9 (a).

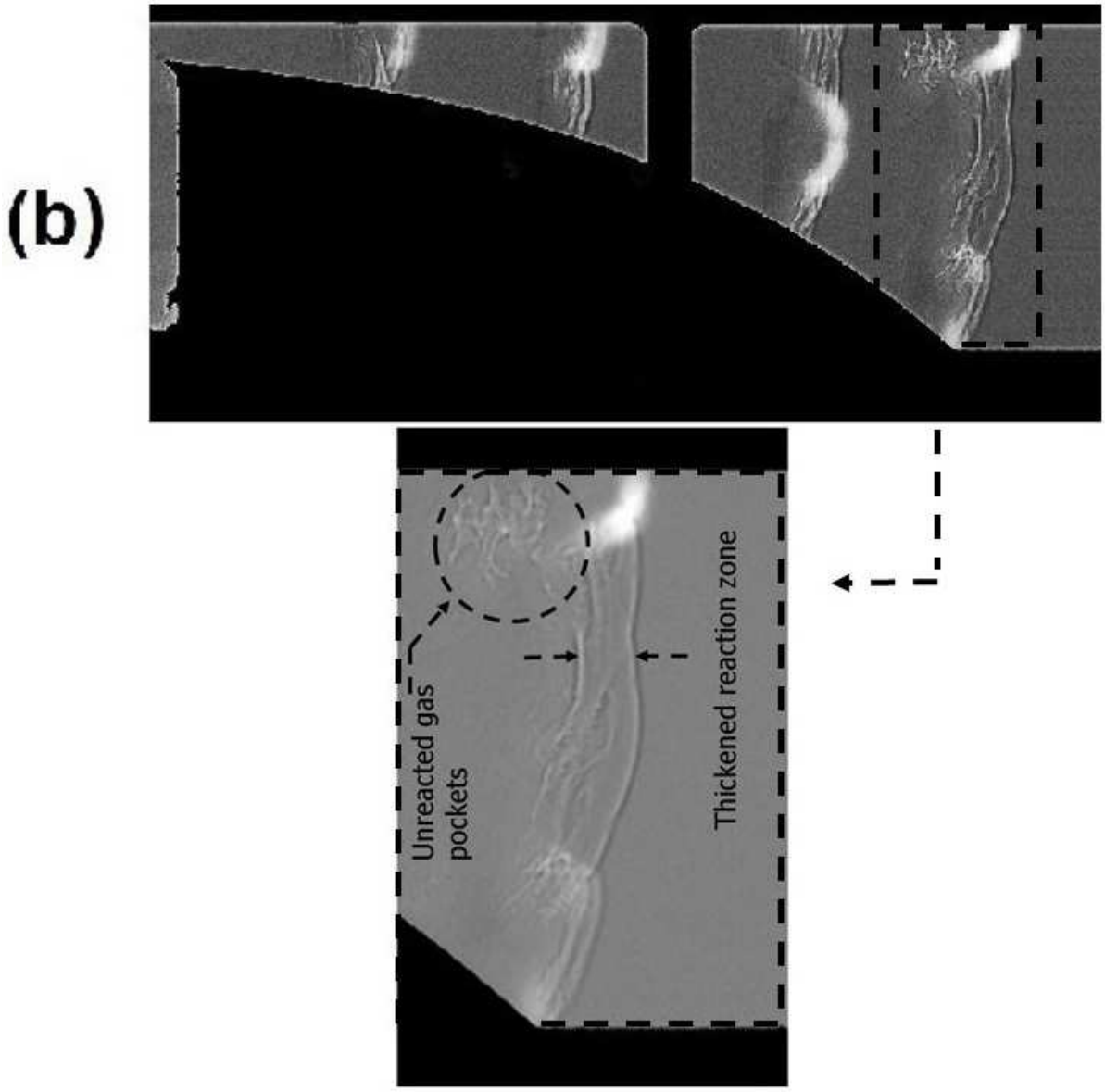

Figure 3.11: Thickened reaction zone and unreacted gas pockets behind the detonation front for $2C_2H_2 + 5O_2 + 21Ar$ mixture at 6.0 kPa (an enlarged view with more details for Figure 3.9 (b)).

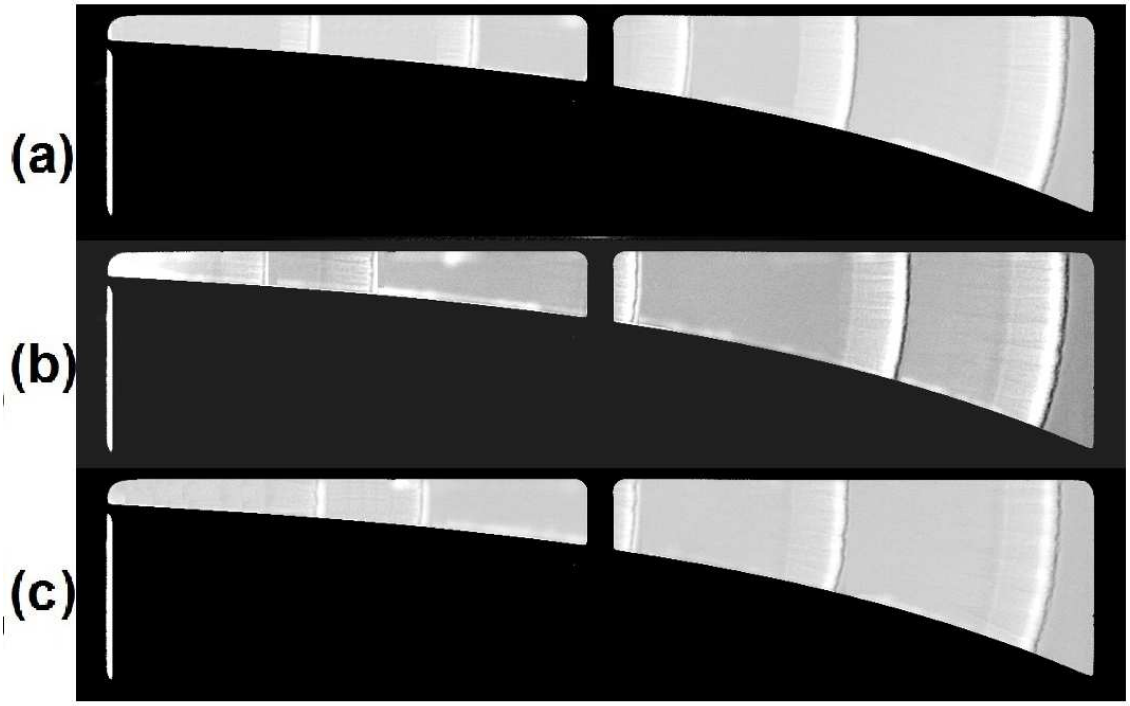

Figure 3.12: Shadowgraph images of detonation wave structure along the large ramp (1-m-length) at sequential time frames for $C_3H_8 + 5O_2$ mixture at (a) 13.8 kPa, (b) 12.1 kPa and (c) 10.3 kPa.

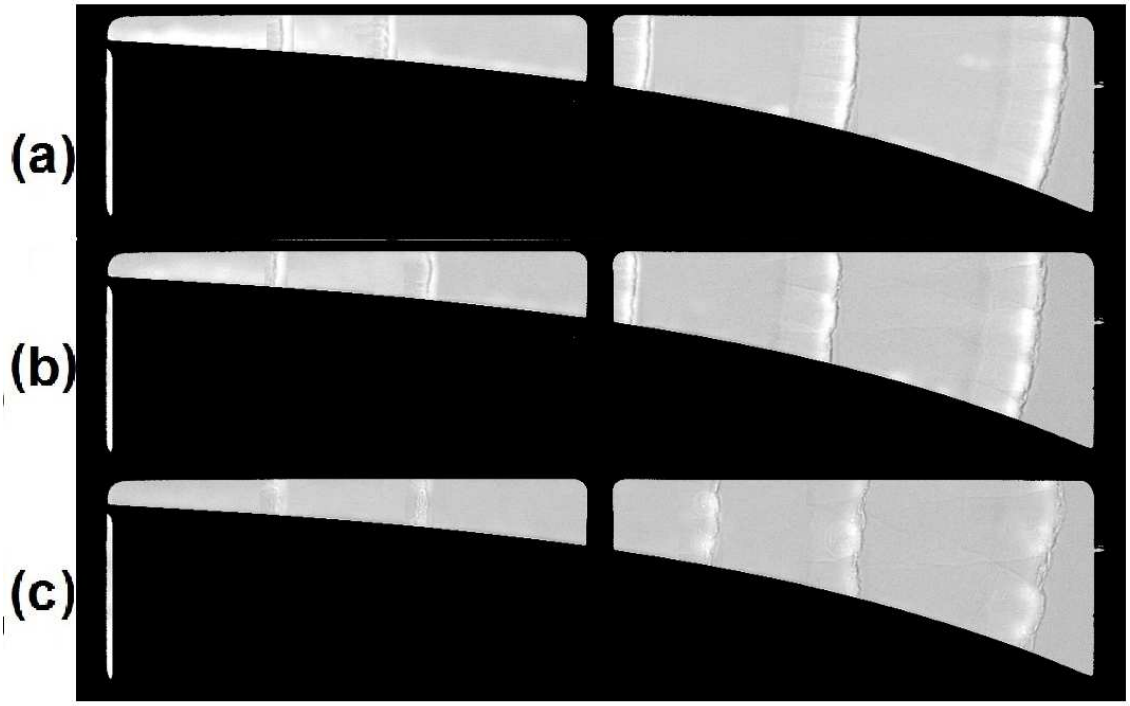

Figure 3.13: Shadowgraph images of detonation wave structure along the large ramp (1-m-length) at sequential time frames for $C_3H_8 + 5O_2$ mixture at (a) 8.7 kPa, (b) 6.9 kPa and (c) 5.2 kPa.

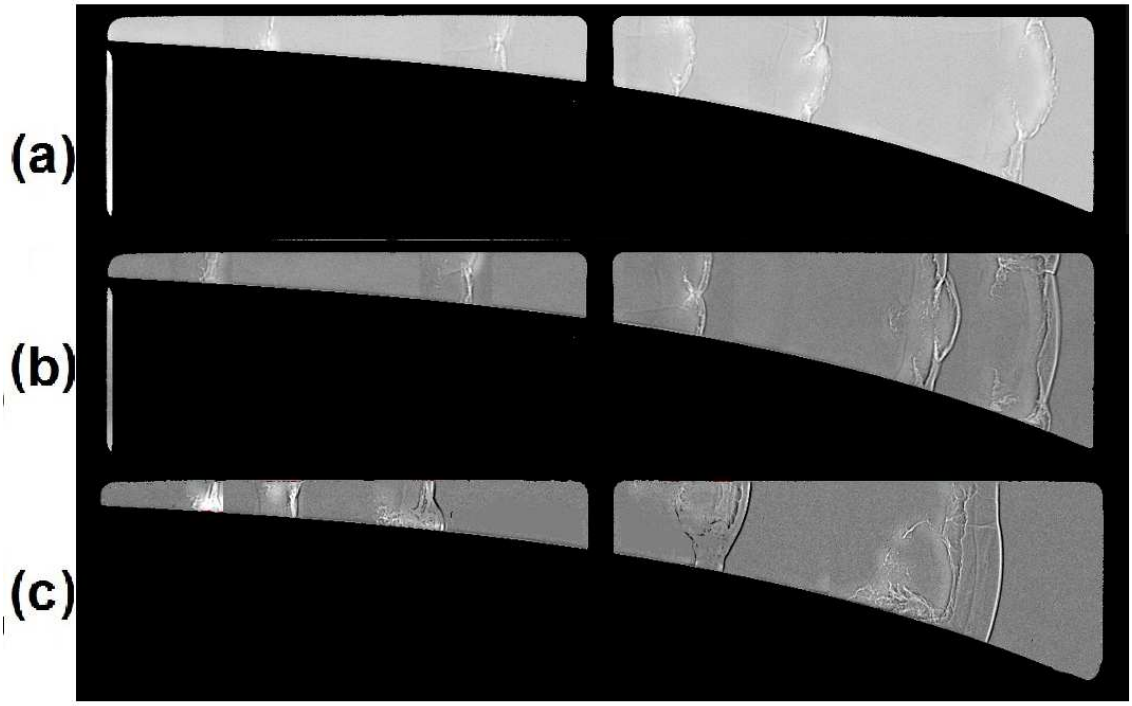

Figure 3.14: Shadowgraph images of detonation wave structure along the large ramp (1-m-length) at sequential time frames for $C_3H_8 + 5O_2$ mixture at (a) 4.1 kPa, (b) 3.4 kPa and (c) 2.1 kPa.

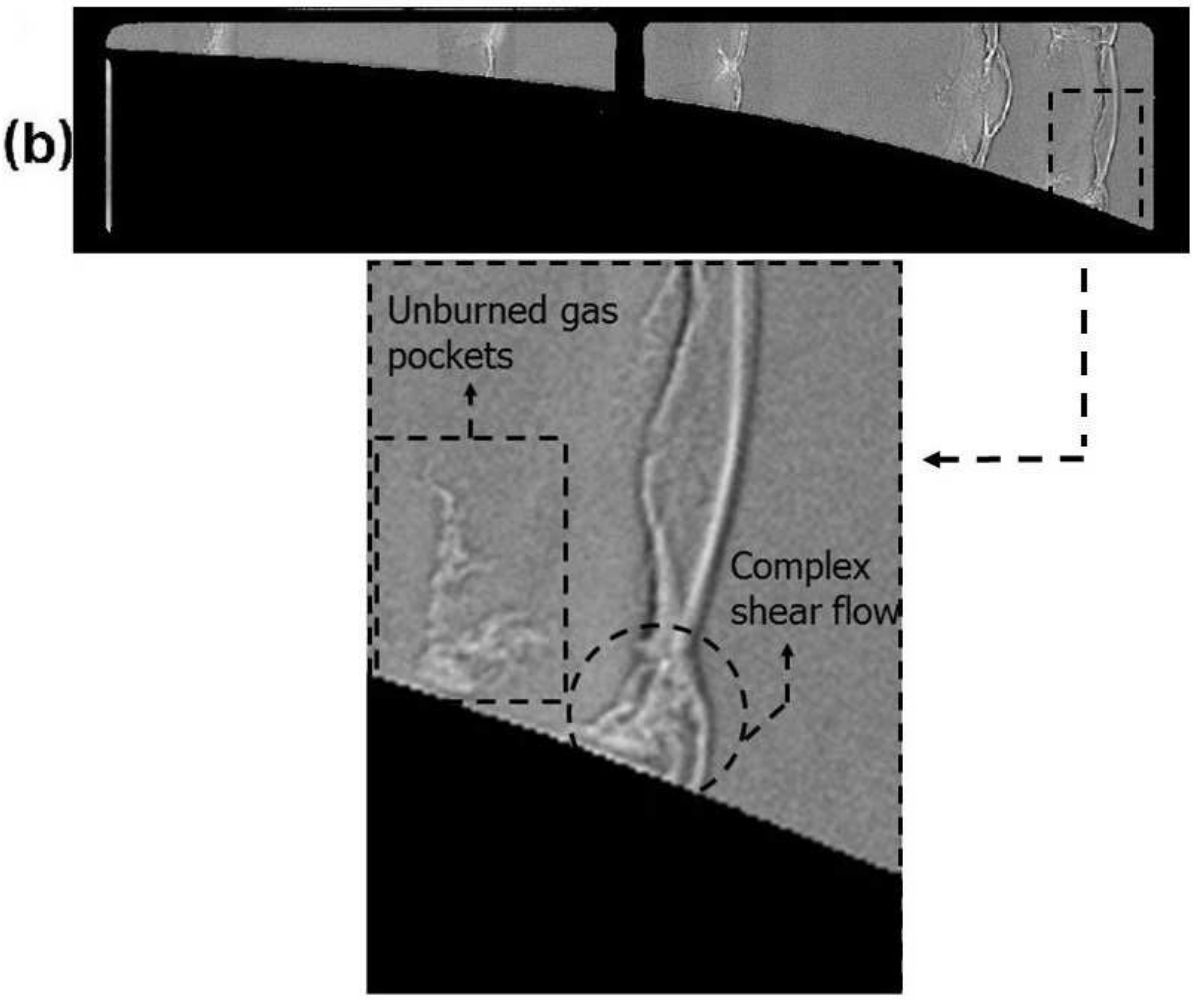

Figure 3.15: Complex pattern of shear flow and pockets of unburned gas behind the detonation front for $C_3H_8 + 5O_2$ at 3.4 kPa (an enlarged view with more details for Figure 3.14 (b)).

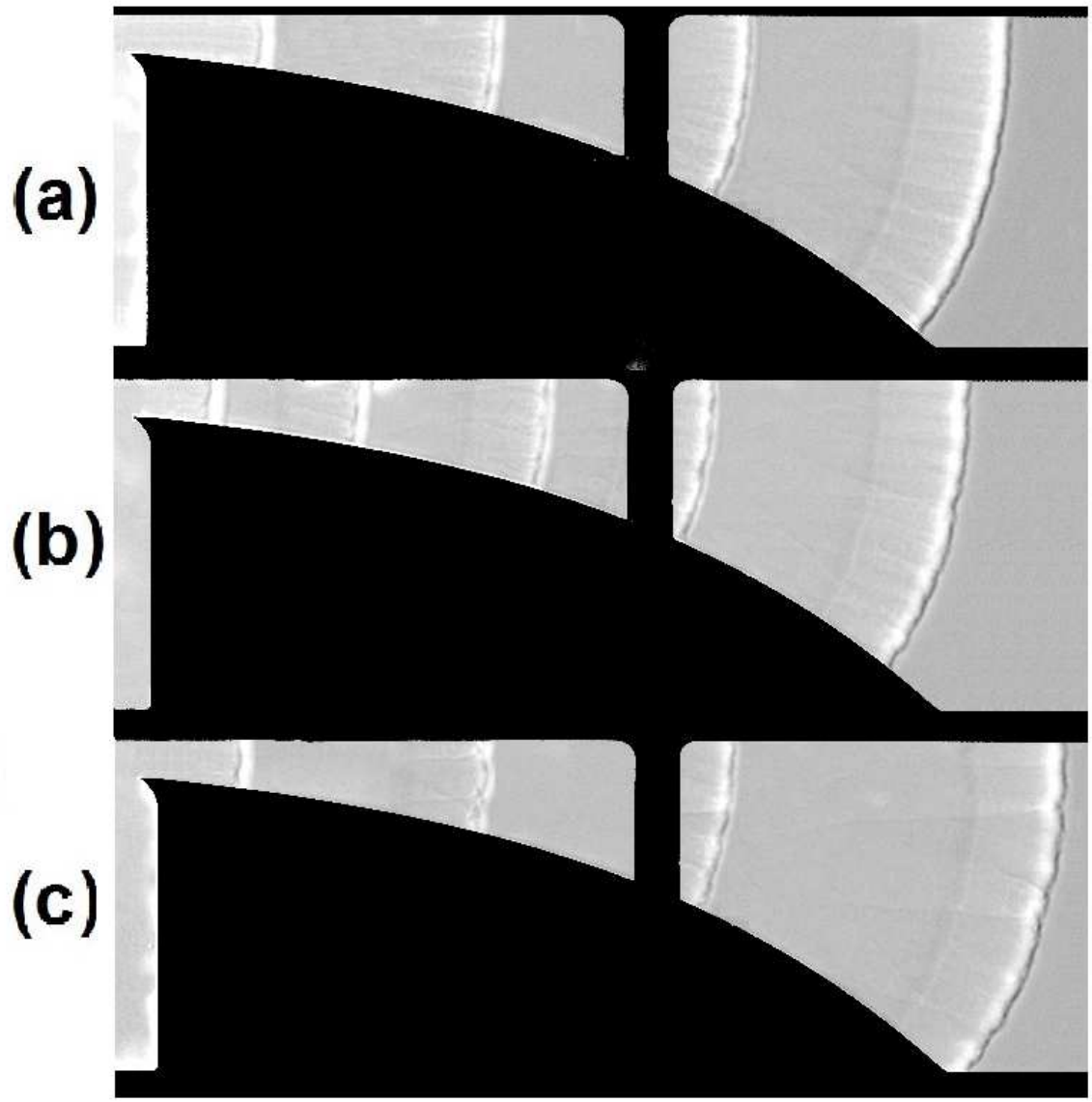

Figure 3.16: Shadowgraph images of detonation wave structure along the small ramp (0.5-m-length) at sequential time frames for $C_3H_8 + 5O_2$ mixture at (a) 12.1 kPa, (b) 10.3 kPa and (c) 8.6 kPa.

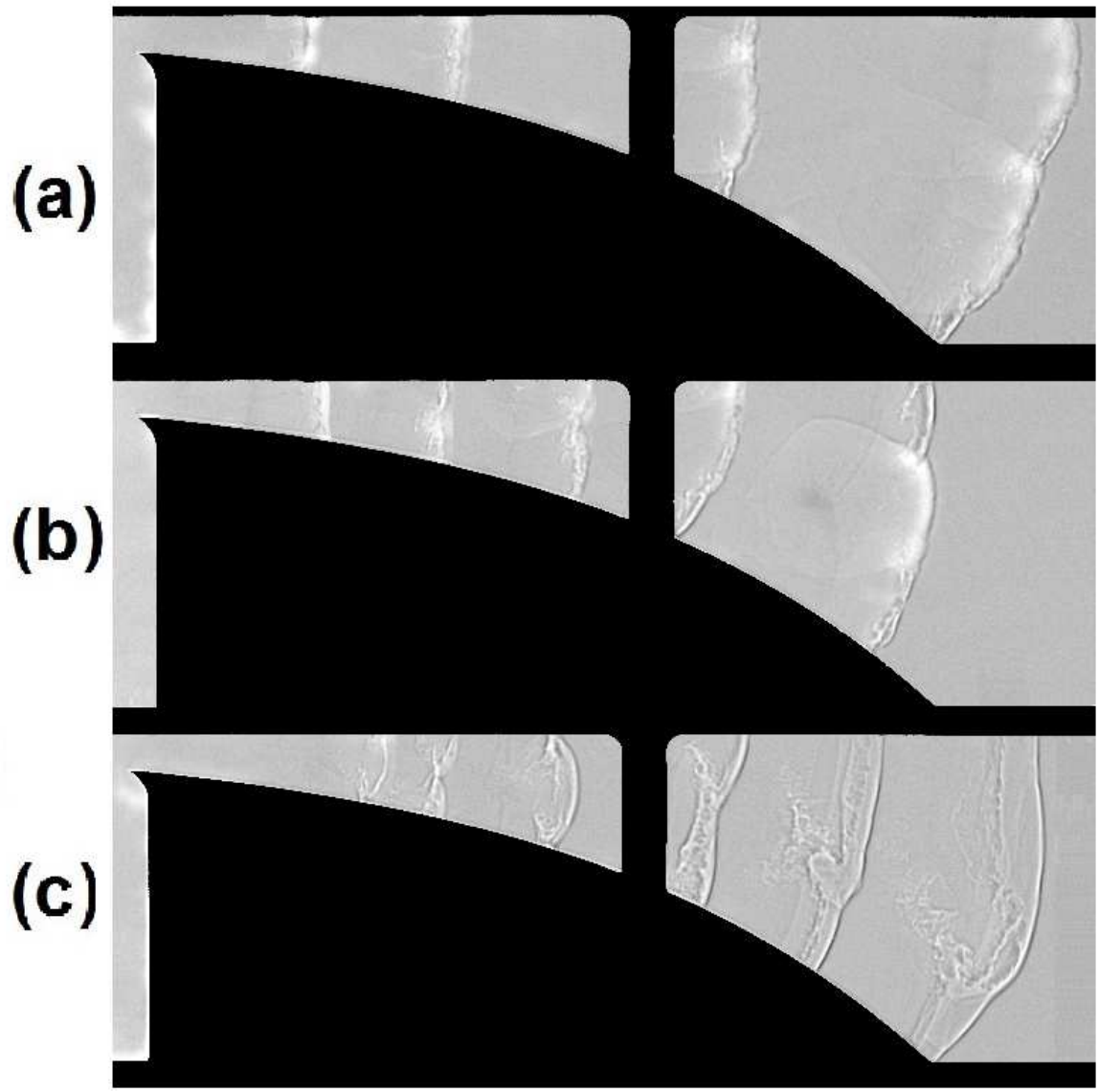

Figure 3.17: Shadowgraph images of detonation wave structure along the small ramp (0.5-m-length) at sequential time frames for $C_3H_8 + 5O_2$ mixture at (a) 6.2 kPa, (b) 5.5 kPa and (c) 4.5 kPa.

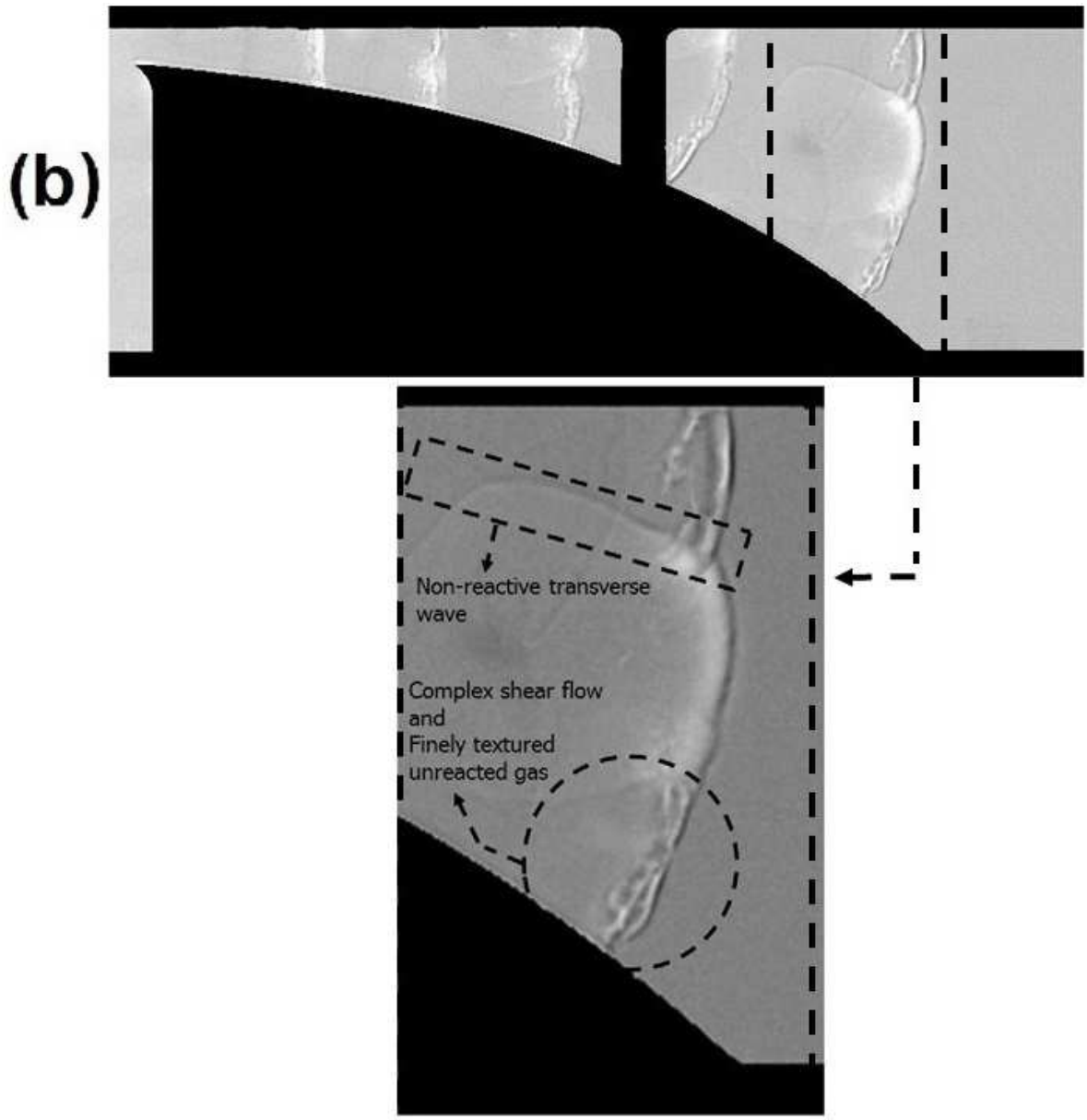

Figure 3.18: Non-reactive transverse wave and finely textured unreacted gas behind the detonation front propagating along the small ramp for $C_3H_8 + 5O_2$ mixture at 5.5 kPa (An enlarged view with more details for Figure 3.17 (b)).

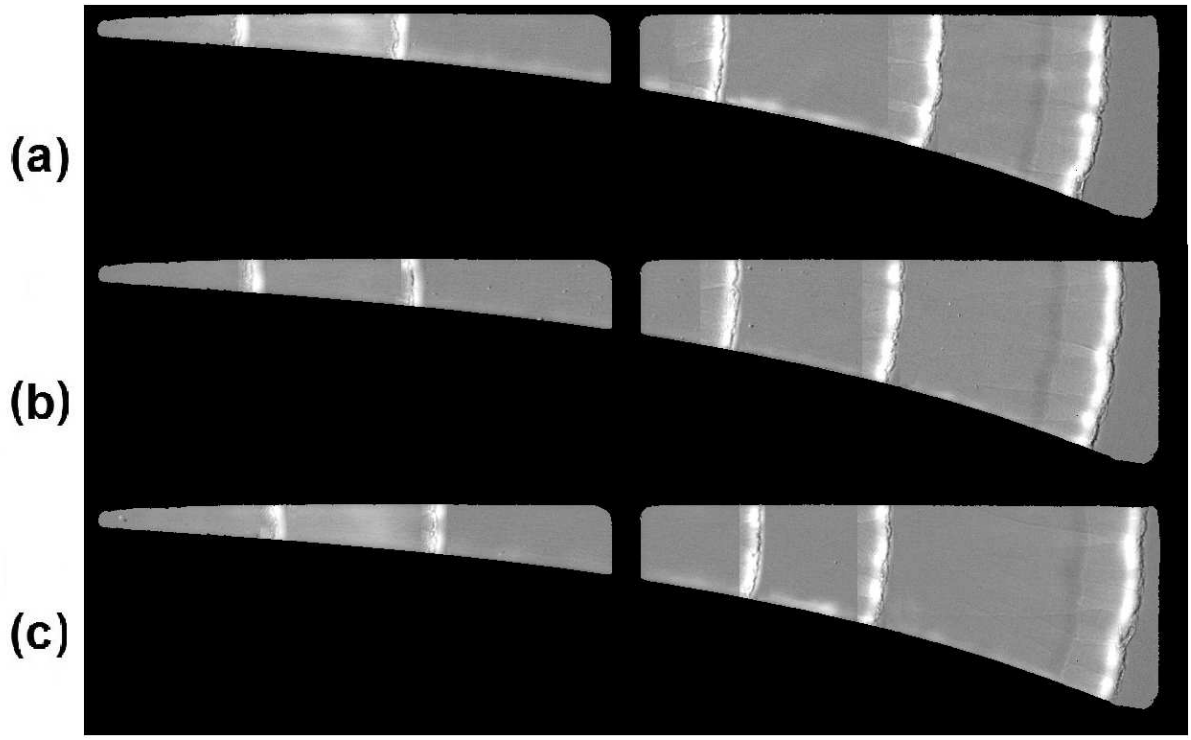

Figure 3.19: Shadowgraph images of detonation wave structure along the large ramp (1-m-length) at three repeated experiments for $C_3H_8 + 5O_2$ mixture at 5.2 kPa.

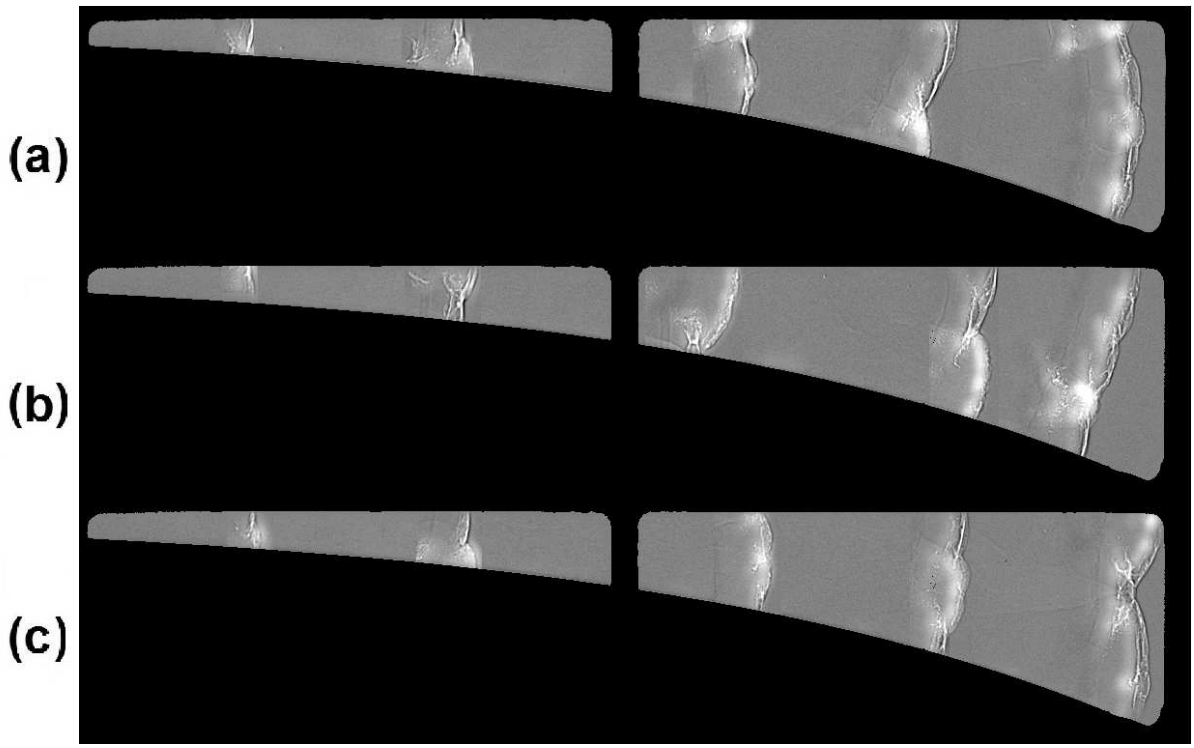

Figure 3.20: Shadowgraph images of detonation wave structure along the large ramp (1-m-length) at three repeated experiments for $C_3H_8 + 5O_2$ mixture at 2.8 kPa.

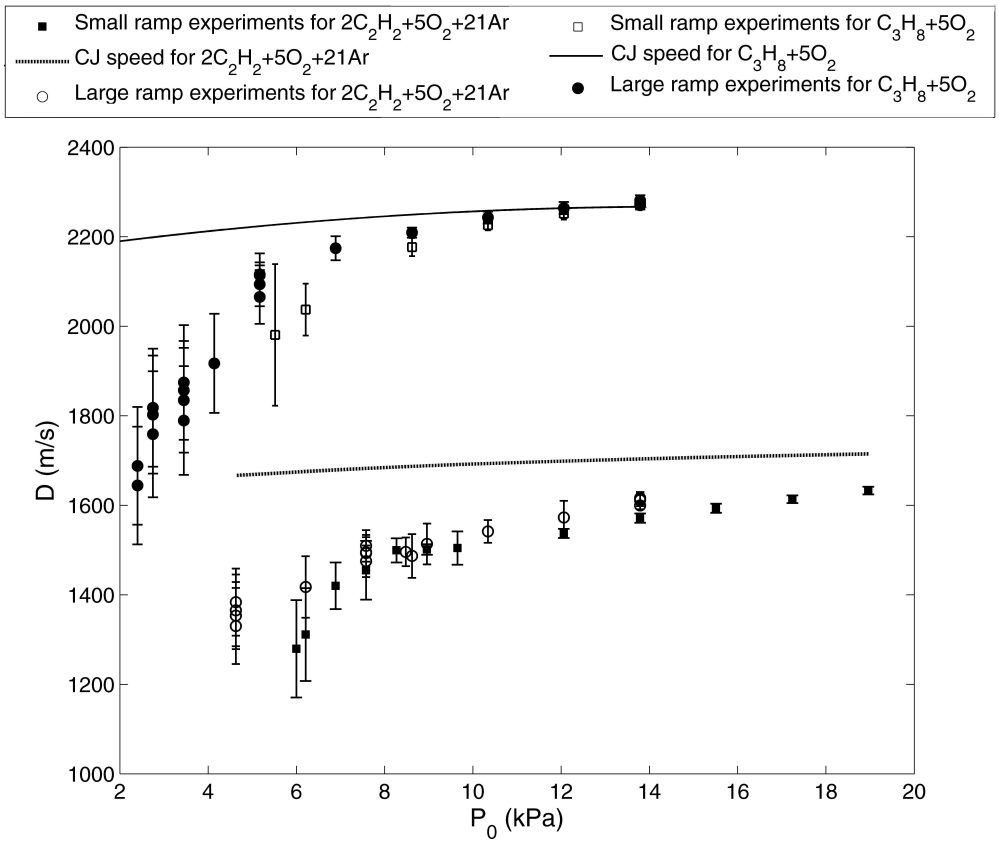

Figure 3.21: Average detonation wave speed measured along the top wall of the diverging domain with respect to initial pressure of the $2C_2H_2 + 5O_2 + 21Ar$ and $C_3H_8 + 5O_2$ mixtures compared to the CJ speed.

Chapter 4

Quasi-one-dimensional model for detonations with mass divergence

4.1 Overview

This chapter presents the solution for the steady traveling wave in a reactive system with constant mass divergence, also known as the quasi-one-dimensional ZND theory. On this basis, the equations governing the quasi-one-dimensional motion of the fluid are presented, for which we seek the traveling wave solution. The model is closed by prescribing a two-step reaction model, for which its parameters are extracted for both acetylene and propane mixtures from chemical kinetic calculations using the state-of-the-art chemical kinetic database. The steady ZND solutions with constant mass divergence are hence obtained. These are further compared to experiments in the following chapters of the thesis.

4.2 Governing equations of motion

Consider a detonation wave propagating in a geometry with variable cross-sectional area such as that shown in Figure 4.1. The Figure also shows the subsequent expansion of a stream tube of the fluid, coming through the shock front. The most general form of the governing equations of motion for such a nozzle flow can be expressed by the reactive Euler equations [3, 54, 55]:

$$\frac{D\rho}{Dt} + \rho\frac{\partial u}{\partial x} + \rho\frac{u}{A}\frac{dA}{dx} = 0 \tag{4.1}$$

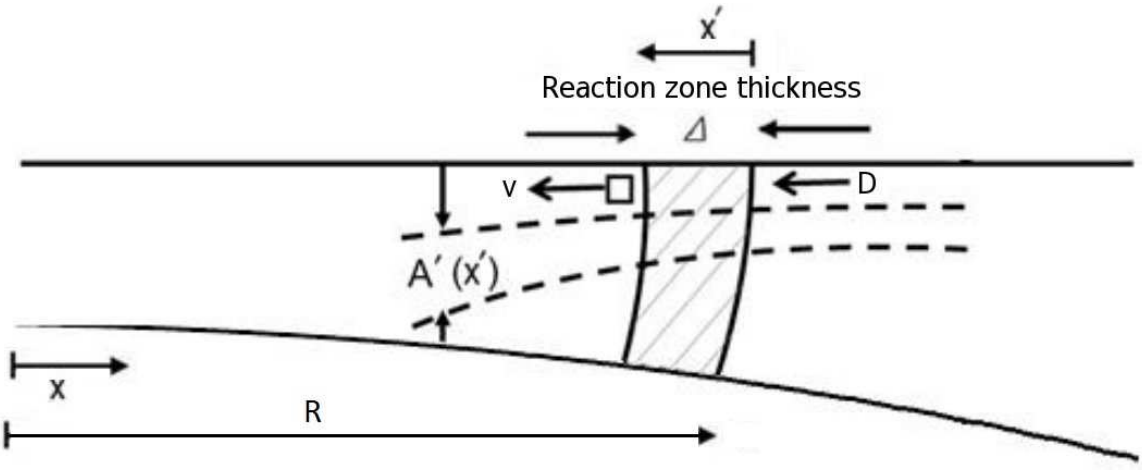

Figure 4.1: Schematic for propagation of a detonation wave in a diverging domain including the absolute and shock attached frames of reference (v denotes the fluid speed in the shock frame of reference).

$$\rho\frac{Du}{Dt}+\frac{\partial p}{\partial x}=0 \tag{4.2}$$

$$\frac{Dp}{Dt}-c^2\frac{D\rho}{Dt}=\rho c^2\dot{\sigma} \tag{4.3}$$

$$\rho\frac{DY_i}{Dt}=\dot{\omega}_i \tag{4.4}$$

where ρ, u, p and c denote the density, speed along the x direction, pressure and the sound speed of the fluid, respectively. The variables x, t and A denote the space coordinates in the lab frame of reference, time coordinate and cross-sectional area of the channel, respectively. Symbols Y_i and $\dot{\omega}_i$ are the mass fraction and net rate of creation for the i^{th} species of the reactive mixture. Derivative D/Dt is the material derivative along the path of a fluid particle expressed by $D/Dt = \partial/\partial t + u\partial/\partial x$. Finally, $\dot{\sigma}$ denotes the thermicity, defined as the chemical energy release rate and expressed by [3, 28, 56, 57]:

$$\dot{\sigma}=\sum_{i=1}^{N}(\frac{W}{W_i}-\frac{h_i}{c_pT})\frac{Dy_i}{Dt} \tag{4.5}$$

where W_i and h_i denote the molar mass and specific enthalpy of the i^{th} species, respectively. Symbols W, c_p and T denote the mean molar mass, specific heat at constant

pressure and the absolute temperature of the mixture, respectively. The total number of species that has been specified is characterized by N.

4.2.1 Conservation laws in the wave frame of reference

The governing Equations (4.1)-(4.4) can also be rewritten in a reference coordinate system attached to the shock wave. As shown in Figure 4.1, x' is the coordinate of space in the shock attached frame of reference. The transformation equations is expressed by

$$x' = R - x \tag{4.6}$$

where R is the location of the wave in the lab frame of reference and is obtained from detonation speed D by

$$R = \int_0^t D(t')dt' \tag{4.7}$$

and

$$\frac{\partial}{\partial t} = \frac{\partial}{\partial x'}\frac{\partial x'}{\partial t} = D\frac{\partial}{\partial x'} + \frac{\partial}{\partial t} \tag{4.8}$$

$$\frac{\partial}{\partial x} = \frac{\partial}{\partial x'}\frac{\partial x'}{\partial x} + \frac{\partial}{\partial t}\frac{\partial t}{\partial x} = -\frac{\partial}{\partial x'}. \tag{4.9}$$

Rewriting (4.1) using (4.8) and (4.9) yields

$$\frac{\partial \rho}{\partial t} + \frac{\partial}{\partial x'}(\rho(D-u)) + \rho\frac{u}{A}\frac{dA}{dx} = 0. \tag{4.10}$$

Let $v = D - u$ be the speed in the shock attached frame of reference. Equation (4.10) would then read

$$\frac{\partial \rho}{\partial \tau} + \frac{\partial}{\partial x'}(\rho v) + \rho\frac{(D-v)}{A}\frac{dA}{dx} = 0. \tag{4.11}$$

In the same fashion, the other conservation Equations (4.2) to (4.4) could also be transformed to the wave frame of reference as

$$\frac{\partial}{\partial t}(D+v) + v\frac{\partial}{\partial x'}(D+v) - \frac{1}{\rho}\frac{\partial p}{\partial x'} = 0 \tag{4.12}$$

$$\frac{\partial p}{\partial t} + v\frac{\partial p}{\partial x'} - c^2(\frac{\partial \rho}{\partial \tau} + v\frac{\partial \rho}{\partial x'}) = \rho c^2 \dot{\sigma} \tag{4.13}$$

$$\rho(\frac{\partial Y_i}{\partial t} + v\frac{\partial Y_i}{\partial x'}) = \dot{\omega}_i. \tag{4.14}$$

4.2.2 Steady traveling wave solution

The steady traveling wave solution to the conservation laws is obtained by setting the terms with derivative of the time to zero in Equations (4.11)-(4.14), yielding:

$$\frac{d}{dx'}(\rho v) + \rho\frac{(D-v)}{A}\frac{dA}{dx} = 0 \tag{4.15}$$

$$v\frac{d}{dx'}(D+v) - \frac{1}{\rho}\frac{dp}{dx'} = 0 \tag{4.16}$$

$$v\frac{dp}{dx'} - c^2 v\frac{d\rho}{dx'} = \rho c^2\dot{\sigma} \tag{4.17}$$

$$\rho v\frac{dY_i}{dx'} = \dot{\omega}_i. \tag{4.18}$$

Since $\frac{1}{A}\frac{dA}{dx}$ is not a function of time and constant in our problem, Equations (4.15)-(4.18) express the steady traveling wave solution for the problem. Note that this departs from previous treatments, where the area divergence term is never a constant, but assumed to be so in various approximations, as discussed in the introduction. In our case, it is constant by the formulation of the problem.

4.2.3 Alternate view

An equivalent description can be obtained by directly writing the governing equations of motion for steady flow in a stream tube of the fluid coming through the shock front (see Figure 4.1). In this alternate view of the problem, the conservation of mass reads as

$$\frac{d}{dx'}(\rho v) + \rho\frac{v}{A'}\frac{dA'}{dx'} = 0 \tag{4.19}$$

where A' is the area of the fluid stream tube as shown in Figure 4.1. Comparing Equations (4.15) and (4.19) a relation between the area divergence of the channel and the stream tube area divergence is obtained as follows:

$$\alpha = \frac{1}{A'}\frac{dA'}{dx'} = K(\frac{D}{v} - 1) \tag{4.20}$$

where α expresses the rate of stream tube area divergence and

$$K = \frac{1}{A}\frac{dA}{dx} \tag{4.21}$$

denotes the rate of diverging geometry area change.

To obtain the solution for the quasi-one-dimensional flow field, the governing Equations (4.16)-(4.19) should be integrated with their appropriate boundary conditions. However, a more convenient form for integration would be in terms of each of the variables in the equations. This form is obtained by differentiating and combining Equations (4.16) to (4.19) together yielding Equations (4.22)-(4.25), known as the ZND equations for detonations with mass divergence [28, 56, 57].

$$\frac{dp}{dx'} = -\rho v\frac{(\dot{\sigma} - v\alpha)}{\eta} \tag{4.22}$$

$$\frac{d\rho}{dx'} = -\frac{\rho}{v}\frac{(\dot{\sigma} - vM^2\alpha)}{\eta} \tag{4.23}$$

$$\frac{dv}{dx'} = \frac{(\dot{\sigma} - v\alpha)}{\eta} \tag{4.24}$$

$$\frac{dY_i}{dx'} = \frac{\omega_i}{\rho v} \tag{4.25}$$

where η denotes the sonic parameter expressed by

$$\eta = 1 - M^2 \tag{4.26}$$

and M is the flow Mach number in the shock wave's frame of reference that is defined by ratio

$$M = \frac{v}{c}. \tag{4.27}$$

4.2.4 Boundary conditions

In order to integrate Equations (4.22) to (4.25), a key issue is prescribing the appropriate boundary conditions. On this basis, the boundary conditions for the problem are described in the following.

Boundary conditions at the shock

The boundary condition at the shock location is the prescription of the flow properties immediately after the shock. These properties are computed from the shock jump conditions evaluated at fixed composition [58, 57, 59].

$$\frac{\rho_2}{\rho_1} = \frac{(\gamma+1)M_s^2}{(\gamma-1)M_s^2+2} \tag{4.28}$$

$$\frac{p_2}{p_1} = 1 + \frac{2\gamma(M_s^2-1)}{\gamma+1} \tag{4.29}$$

$$\frac{v_2}{D} = \frac{2(M_s^2-1)}{(\gamma+1)M_s^2} \tag{4.30}$$

where M_s is the shock wave Mach number expressed by

$$M_s = \frac{D}{c_1} \tag{4.31}$$

In the above Equations, state 1 denotes the reactant conditions upstream of the shock front and $v_1 = D$. State 2 denotes the Von Neumann [VN] conditions just downstream of the shock (beginning of the reaction zone). These properties are evaluated for state 2 with a given shock speed D and upstream state 1. Since the post-shock state variables are a function of detonation speed D, therefore the entire solution to the problem will be parametrized by D. Only a single value of D, the so-called detonation speed *eigenvalue*, will simultaneously satisfy the downstream boundary conditions, described next.

Generalized CJ condition

The downstream boundary condition is the so-called generalized Chapman-Jouguet condition that requires the flow to be non-singular. The flow is initially subsonic behind the shock. The exothermicity drives the flow towards the sonic flow condition. Eventually the flow becomes supersonic in the wave frame. The sonic parameter η must thus pass through zero within the reaction zone. Inspection of the structure equations indicates that the only way in which this can occur and still have a non-singular solution is for the numerator $\dot{\sigma} - v\alpha$ to vanish at the same location as η, i.e., at the sonic point $M = 1$ in Equations (4.22)-(4.24). This will occur only for particular values of the shock speed D_s for each value of the curvature K. The appearance of a sonic point in this flow can be attributed to the competing effects of chemical energy release $\dot{\sigma}$ and area change

$v\alpha$. Therefore, the numerator of the governing equations $\dot{\sigma} - v\alpha$ must vanish with the denumerator at the sonic point $M = 1$. This is called the generalized Chapman-Jouguet criterion for detonations with losses.

4.3 Reaction model

In order to solve Equations (4.22)-(4.25), a chemistry model is needed to establish the link between the chemical reactions and chemical energy release rate and define the thermicity $\dot{\sigma}$. Such calculations, especially in multi-dimensions, may be computationally demanding, so the model for the chemical reactions must be both fast and accurate enough for the problem at hand. A first approach might be to try to use a detailed chemical model consisting of a very large number of chemical reactions among many chemical species. The drawbacks of such an approach are the computational costs, and the fact that very rarely are all the individual elementary reactions known well enough to justify their use [60]. Therefore, this approach may not be practical or justified for multi-dimensional flows or flows with complicated chemical reaction mechanisms. To be usable in practical applications, numerical simulations should be inexpensive enough to permit rapid calculations for a wide range of the governing parameters for a given problem. This has led to a number of approaches to determining suitable simplified chemical models.

One common approach is to replace the full reaction set by a simplified reaction mechanism, the simplest consisting of a single irreversible Arrhenius reaction. This type of one-step reaction model has been used extensively in simulating a wide range of detonation problems, from the early works on one-dimensional pulsating detonations [61] to multi-dimensional detonations with cellular structure [43, 62, 63].

In the meanwhile, systematic methods of replacing the full set of chemical reactions by a reduced reaction set have been further introduced [60, 64]. For instance, in high-speed compressible flows with sudden heating of reactive mixtures by shock waves, the chemical reactions are found to consist of two distinct periods [65]. Such chemical reactions essentially consist of a thermally neutral induction period, characterized by an induction time t_i and a reaction time t_r. During this induction period, the reactant molecules dissociate to form free radicals with negligible changes in the temperature and pressure of the mixture. This is followed by a zone of recombination of the generated radicals into product molecules and consequent energy release (within a reaction zone). During this reaction period, the final combustion products are generated [65].

Such observations have resulted in the development of two-step induction-reaction models to represent these two phases of combustion. An early example of a two-step reaction model is the work of Korobeinikov *et al.*, [66]. Two-step models for reaction, have been used successfully in numerical simulations to reproduce observed characteristics of detonations and their structure in various problems. Some examples include the work of Oran *et al.* [67], Taki and Fujiwara [68], He and Clavin [69], Oran *et al.* [70] and Kailasanath *et al.* [71].

4.3.1 Two-step model

Although full chemistry models are affordable for steady wave calculations, multi-dimensional unsteady calculations, such as those presented in the next chapter, are very costly and are presently not possible. In the current study, in order to avoid the difficulties and drawbacks of performing the detonation simulations with full chemistry, the two-step reaction model used by Short and Sharpe [47] was adopted with the following equations for the induction and reaction progress variables.

$$\frac{D\lambda_i}{D\tilde{t}} = -\tilde{K}_i H(\lambda_i) e^{-\frac{\tilde{E}_a}{\tilde{R}\tilde{T}}} \tag{4.32}$$

$$\frac{D\lambda_r}{D\tilde{t}} = \tilde{K}_r (1 - H(\lambda_i))(1 - \lambda_r)^{\nu} \tag{4.33}$$

where λ_i denotes a progress variable for the induction zone, with a value of 1 in reactants and 0 at the end of the induction zone and $\tilde{K}_i$ is a rate constant and $H()$ is the Heaviside function which turns off the progress variable λ_i at the end of the induction zone. Likewise, $\tilde{K}_r$, λ_r and ν are the reaction zone rate constant, progress variable and reactions order, respectively. The reaction zone progress variable λ_r is also assumed to be 0 in the induction zone and take a value of 1 in the burned products.

In the two-step model considered, there is no energy release in the induction zone and all of the heat release occurs in the reaction zone. The residual chemical energy $\tilde{q}$ can then be written in terms of the progress variable of the reaction zone λ_r as

$$\tilde{q} = \lambda_r \tilde{Q} \tag{4.34}$$

where $\tilde{Q}$ represents the total chemical energy that is released during the reaction. The thermicity, representing the effective rate of energy release, was expressed as [3, 72]

$$\dot{\sigma} = (\gamma - 1)\frac{\tilde{Q}}{\tilde{c}^2}\frac{D\lambda_r}{D\tilde{t}} \tag{4.35}$$

where γ is the specific heat ratio.

This Equation (4.35) is used instead of (4.5) along with Equations (4.22) to (4.25) to obtain the structure for quasi-one-dimensional detonations with mass divergence in the framework of the two-step reaction model.

4.3.2 Extracting the parameters for the reaction model

Induction and reaction time scales

While there are numerous methods that can be used to extract meaningful values for detonation kinetic parameters in the framework of the reaction model chosen [28, 73, 74, 75], the present research adopted the method of Radulescu *et al.* [28, 75]. The induction and reaction times of the mixture are calculated by performing constant volume ignition calculations with the full chemistry for the reactive mixture at the Von Neumann (VN) shock state. In this regard, the VN state was found through chemical equilibrium calculations performed using the NASA CEA code [53]. The calculations also provided the shock speed. The post shock conditions were obtained assuming the composition remains frozen across the shock.

The constant volume calculations were performed using the CANTERA package [76]. In this regard, for both acetylene and propane mixtures the Sandiego mechanism [77] optimized for the combustion of these fuels was used. In the calculations, the ignition delay time $\tilde{t}_{ign}$, was taken as the delay to the point of maximum rate of temperature changes with respect to time $(d\tilde{T}/d\tilde{t})_{Max}$. The characteristic reaction time $\tilde{t}_e$ was also taken as the characteristic time scale for the rise, i.e., the inverse of the maximum rate of the heat release [5, 28]:

$$\tilde{t_e} = (d(ln\tilde{T})/d\tilde{t})^{-1}_{Max}. \tag{4.36}$$

Effective activation energy

The activation energy was extracted from the approximate dependence of the ignition delay $\tilde{t}_{ign}$ on initial temperature, which can be approximated by [28]

$$\tilde{t}_{ign} \propto \exp(\frac{\tilde{E}_a}{\tilde{R}\tilde{T}}). \tag{4.37}$$

The activation energy can thus be obtained by calculating the ignition delays at two different temperatures bracketing the VN state. We chose the bracketing temperatures as $\tilde{T}_{vN}$ and $\tilde{T}_{vN} + 100K$ to get the corresponding ignition delay times. As a consequence, we obtained

$$\frac{\tilde{E}_a}{\tilde{R}\tilde{T}_{vN}} = \frac{1}{\tilde{T}_{vN}}\left(\frac{ln(\tilde{t}_{ign+}) - ln(\tilde{t}_{ign})}{\frac{1}{\tilde{T}_{vN+}} - \frac{1}{\tilde{T}_{vN}}}\right). \tag{4.38}$$

Heat Release

The heat release parameter was extracted from equilibrium calculations so that a perfect gas model using this value of energy release and the ratio of specific heats evaluated at the VN point yielded the exact CJ detonation Mach number [5], i.e.,

$$\frac{\tilde{Q}}{\tilde{R}\tilde{T}_0} = \frac{\gamma}{2(\gamma^2 - 1)}(M_{CJ} - \frac{1}{M_{CJ}})^2. \tag{4.39}$$

Stability parameter

In the literature, detonability of reactive mixtures and their propensity to establish detonation waves, have been assessed by a parameter called the stability parameter, expressed as the following [28, 75, 47, 78, 72]:

$$\chi = \frac{\tilde{E}_a}{\tilde{R}\tilde{T}_{vN}}\frac{\tilde{t}_{ign}}{\tilde{t}_e}. \tag{4.40}$$

After calculating the values for activation energy, ignition delay and reaction time, and as the next step in the extracting two-step model parameters for the mixture, the stability parameter χ was calculated using Equation (4.40).

Induction rate constants K_i

In extracting the induction and reaction rate constants, an appropriate scaling has been performed using the reference scales in the two-step model framework. In this regard, the length was scaled by the length of the induction stage $\tilde{\Delta}_i$ so that

$$x = \frac{\tilde{x}}{\tilde{\Delta}_i}. \tag{4.41}$$

Pressure, density and velocity were also normalized by the upstream state to be

$$p = \frac{\tilde{p}}{\tilde{p_0}} \quad \rho = \frac{\tilde{\rho}}{\tilde{\rho_0}} \quad u = \frac{\tilde{u}}{\sqrt{\frac{\tilde{p_0}}{\tilde{\rho_0}}}} \tag{4.42}$$

and, finally the time was scaled by ratio

$$t = \frac{\tilde{t}\sqrt{\frac{\tilde{p_0}}{\tilde{\rho_0}}}}{\tilde{\Delta}_i}. \tag{4.43}$$

Using the above mentioned normalization, the induction rate constant $\tilde{K}_i$ was found in the following way. Integrating the equation for evolution of the induction zone (4.32) through the whole induction period yields

$$\lambda_i(\tilde{t})\Big|_{\tilde{t}=0}^{\tilde{t}=\tilde{t_i}} = -\tilde{K}_i H(1-\lambda_i)e^{-\tilde{E_a}/\tilde{R}\tilde{T}}\Big|_{\tilde{t}=0}^{\tilde{t}=\tilde{t_i}} \tag{4.44}$$

and therefore

$$\tilde{t_i} = {\tilde{K}_i}^{-1} e^{\tilde{E_a}/\tilde{R}\tilde{T_s}}. \tag{4.45}$$

The induction time in the frame work of two-step model can also be obtained from

$$\tilde{t_i} = \frac{\tilde{\Delta}_i}{\tilde{D} - \tilde{u_s}} \tag{4.46}$$

where $\tilde{D}$ and $\tilde{u_s}$ denote the shock speed and the speed of the gas behind the shock, respectively. Combining Equations (4.45), (4.46), the shock jump condition for the speed (4.30) and using the described scaling, the induction rate parameter can be obtained as

$$K_i = \frac{\sqrt{\gamma}[2+(\gamma-1)M^2]}{(\gamma+1)M} e^{\tilde{E_a}/\tilde{R}\tilde{T_s}} \tag{4.47}$$

and the scaled time for the induction period follows from (4.45) as

$$t_i = \frac{(\gamma+1)M}{\sqrt{\gamma}[2+(\gamma-1)M^2]}. \tag{4.48}$$

Reaction rate constants K_r

For the two-step model used, the maximum thermicity occurs at the beginning of the reaction zone when the induction zone terminates. Therefore, at the beginning of the reaction zone and based on Equation (4.33)

$$(\frac{D\lambda_r}{Dt})_{Max} = K_r \tag{4.49}$$

Table 4.1: Values of the kinetic parameters in the framework of the reduced chemistry model for the acetylene and propane mixtures

Mixture	γ	$\tilde{E}_a/\tilde{R}\tilde{T}_0$	$\tilde{Q}/\tilde{R}\tilde{T}_0$	K_i	K_r
$2C_2H_2 + 5O_2 + 21Ar$	1.42	27.75	18.3	86.05	8.13
$C_3H_8 + 5O_2$	1.14	56	99	84727.8	5.13

by using Equations (4.35) and (4.36), the scaled reaction time in the framework of the two step model is obtained as

$$t_e = [(\gamma - 1)\frac{\tilde{Q}}{\tilde{c}^2}K_r]^{-1} = (\frac{1}{\dot{sigma}})_{Max}. \tag{4.50}$$

The calculated value for χ in the previous steps was used to extract the value for the reaction rate parameter K_r. Combining Equations (4.40), (4.48) and (4.50), the reaction rate parameter is given by

$$K_r = \chi\frac{\gamma}{\gamma - 1}(t_i\frac{\tilde{E}_a}{\tilde{R}\tilde{T}_s}\frac{\tilde{Q}}{\tilde{R}\tilde{T}_s})^{-1}. \tag{4.51}$$

Parameters for acetylene and propane mixtures

The parameters of the two-step reaction model were extracted for both acetylene and propane mixtures using the above mentioned steps. The values are reported in Table 4.1. Comparison was performed between the full chemistry and the two-step model used for calculations. Figures 4.2, 4.3 and 4.4 show the pressure, density and speed profiles behind a steady detonation wave, respectively. The profiles with the full chemistry were obtained by using the shock and detonation toolbox developed by Joseph Shepherd and adopting the Sandiego mechanism [77] for the combustion of the gases. It can be seen that the hydrodynamics captured by the two-step model is in good agreement with the full chemistry model.

4.4 Results

In order to obtain the dynamics of quasi-one-dimensional detonations with mass divergence, the governing Equations (4.22)-(4.24) along with the two-step reaction model Equations (4.32) and (4.33), were solved numerically with their appropriate boundary

conditions described in Section 4.2.4. Numerical integration of the equations was performed using the Mathematica software that chose the appropriate ODE solver based on the stiffness of the equations. Calculations were performed for different values of the detonation speed and by searching for singularity in the solution within the machine precision, the corresponding value for area divergence rate was obtained.

Numerical solution finally provided the relationship between the shock speed and the area divergence rate K. The calculations were performed using the parameters obtained from kinetic calculations for each mixture (see Table 4.1). The results of the calculations for both acetylene-oxygen-argon and propane-oxygen mixtures are shown in Figure 4.5. In this Figure, the detonation speed normalized with the CJ speed is plotted with respect to the area divergence rate of the channel. It can be seen that when the value of the area divergence is zero, the detonation propagates with the CJ speed as expected. For both mixtures, by increasing the value of the area divergence, the corresponding speed deficit for the shock increases until the curve reaches an inflection point where the detonation wave extinguishes. A Further increase in the area divergence does not allow a steady state solution. The reason for this is the inability for the weaker exothermicity to drive the flow to the sonic condition, as the mass divergence, having the opposite effect, is stronger. It can be seen that the critical rate of area divergence required for the extinction of the detonation wave is bigger in the acetylene mixture. Also the critical velocity deficit in the acetylene mixture (86%) is more substantial than in propane mixture (94%). Finally, it should be noted that the numerical solution has provided a double valued relation between the detonation speed and the divergence rate where the bottom branch of the curve is the nonphysical part of the solution.

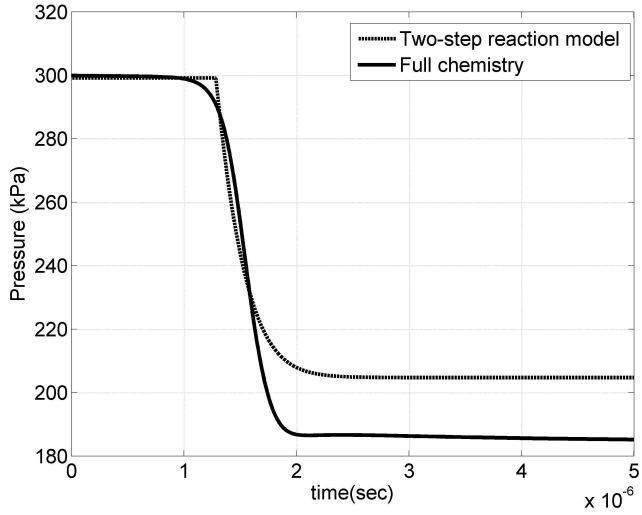

Figure 4.2: Pressure profiles behind a steady detonation wave as a function of time obtained by using full chemistry and two-step reaction model.

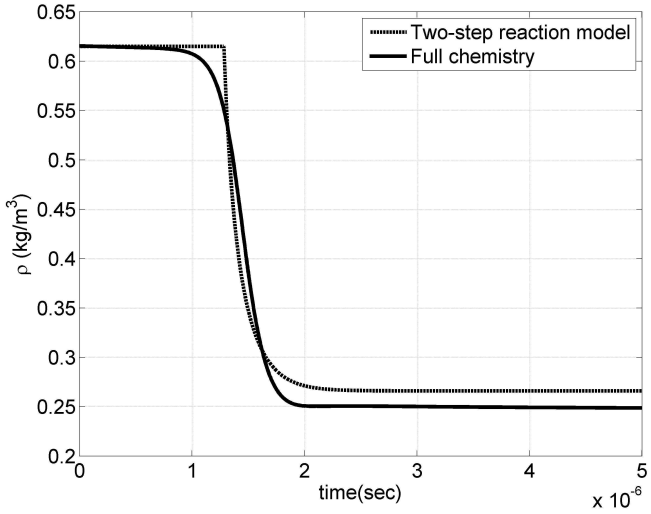

Figure 4.3: Density profiles behind a steady detonation wave as a function of time obtained by using full chemistry and two-step reaction model.

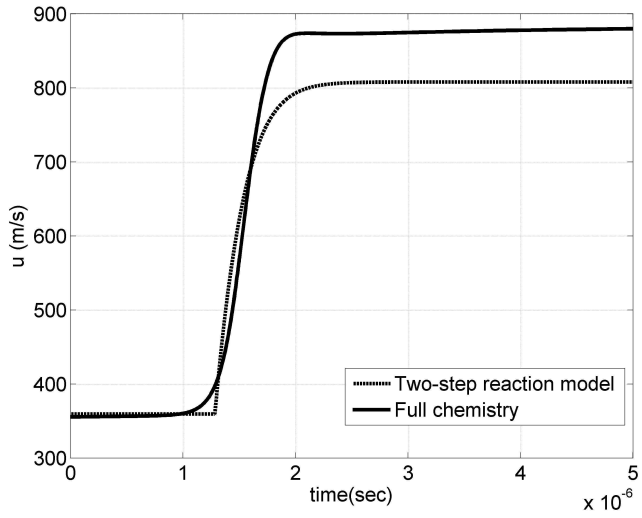

Figure 4.4: Speed profiles behind a steady detonation wave as a function of time obtained by using full chemistry and two-step reaction model.

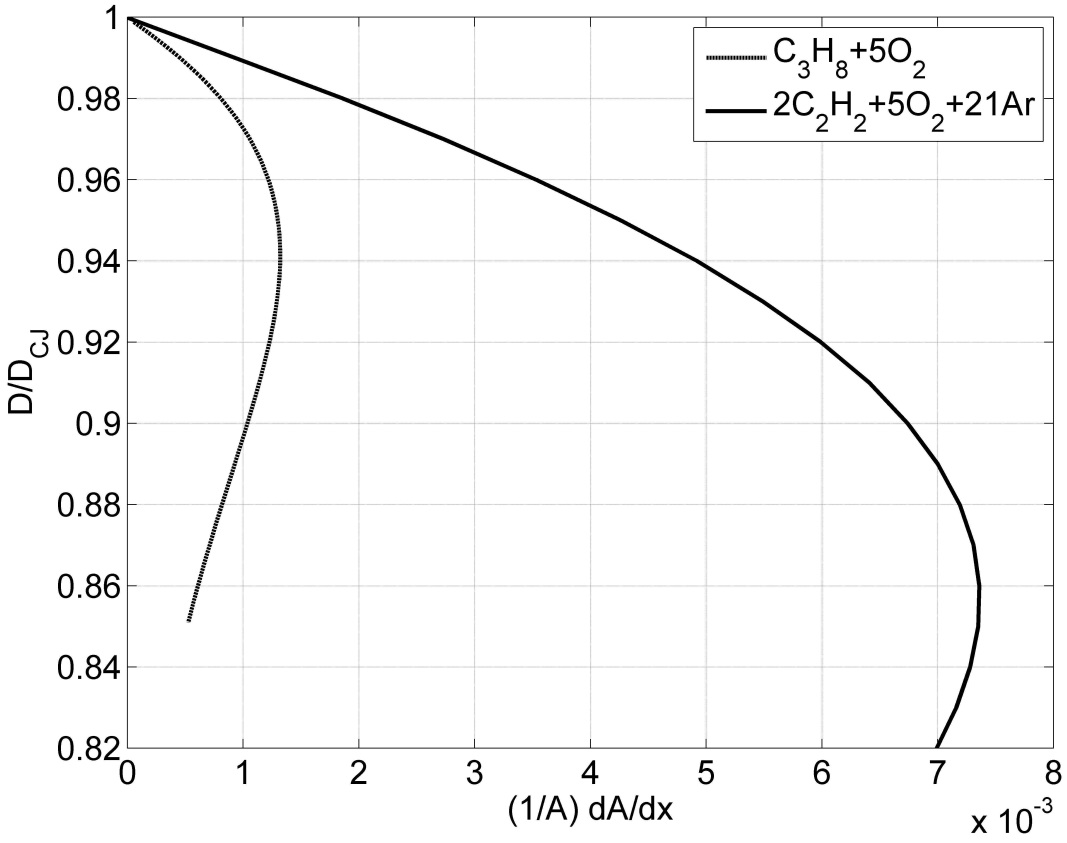

Figure 4.5: Detonation speed changes with respect to area divergence rate for quasi-one-dimensional detonations with mass divergence for the $2C_2H_2{+}5O_2{+}21Ar$ and $C_3H_8{+}5O_2$ mixtures.

Chapter 5

Cellular dynamics of detonations with constant mass divergence

5.1 Overview

In this chapter, the results of the numerical investigation of the dynamics for two-dimensional cellular detonations with constant mass divergence are presented for the acetylene-oxygen-argon mixture. The governing equations are described. The numerical platform used for solving the flow is introduced and benchmarked with a known solution. Finally, the solution to the flow field is sought and discussed in the diverging domain.

5.2 Governing equations

Consider the motion of a compressible fluid with chemical energy content in a two-dimensional domain. The dynamics of the fluid motion are governed by the two-dimensional reactive Navier-Stokes equations. For fast high Mach number detonation wave solutions, diffusive terms can be neglected and thus the reactive Euler equations can be taken as the set of the equations governing the flow motion [3, 6, 72]. The conservation of mass, linear momentum, and energy equations therefore read

$$\frac{D\tilde{\rho}}{D\tilde{t}} + \tilde{\rho}(\frac{\partial \tilde{u}}{\partial \tilde{x}} + \frac{\partial \tilde{v}}{\partial \tilde{y}}) = 0 \tag{5.1}$$

$$\frac{D\tilde{u}}{D\tilde{t}} + \frac{1}{\tilde{\rho}}\frac{\partial \tilde{p}}{\partial \tilde{x}} = 0 \tag{5.2}$$

$$\frac{D\tilde{v}}{D\tilde{t}} + \frac{1}{\tilde{\rho}}\frac{\partial \tilde{p}}{\partial \tilde{y}} = 0 \tag{5.3}$$

$$\frac{D}{D\tilde{t}}(\tilde{e} - \lambda\tilde{Q}) + \tilde{p}\frac{D}{D\tilde{t}}(\frac{1}{\tilde{\rho}}) = 0. \tag{5.4}$$

In the above set of Equations, $\tilde{\rho}$, $\tilde{p}$, $\tilde{u}$ and $\tilde{v}$ denote the density, pressure and fluid velocity components in x and y directions, respectively. Also, $\tilde{x}$ and $\tilde{y}$ represent the space coordinates and $\tilde{t}$ is the time coordinate. Likewise, $\tilde{e}$ and $\tilde{Q}$ denote the specific internal energy of the material and residual chemical energy available in it. Finally, $D/D\tilde{t} = \partial/\partial\tilde{t} + \tilde{u}\partial/\partial\tilde{x} + \tilde{v}\partial/\partial\tilde{y}$ denotes the material derivative and symbols with tildes represent dimensional quantities.

The fluid is assumed to be as a calorically perfect gas described by the equation of state

$$\tilde{e} = \frac{1}{\gamma - 1}\frac{\tilde{p}}{\tilde{\rho}} \tag{5.5}$$

where γ is the isentropic exponent.

For the evolution of the chemical reactions, once again the two-step reaction model with the following separate equations for the induction and reaction stages used by Short and Sharpe [47] (described in Section 4.3.1 by Equations (4.32) and (4.33)), is adopted.

5.2.1 The non-dimensional form

In the numerical simulations of this thesis, the pre-shock state in the steady ZND solution was adopted as the state to scale the flow variables by. Therefore, the pressure and density are non-dimensionalized by the initial pressure and density, respectively.

$$p = \frac{\tilde{p}}{\tilde{p_0}} \ , \ \rho = \frac{\tilde{\rho}}{\tilde{\rho_0}} \tag{5.6}$$

In order to keep the consistency of scales, the reference scales for flow motion and energy becomes $\sqrt{\tilde{p_0}/\tilde{\rho_0}} = \sqrt{\tilde{R}\tilde{T_0}} = \tilde{c_0}/\sqrt{\gamma}$ and $\tilde{p_0}/\tilde{\rho_0} = \tilde{R}\tilde{T_0} = \tilde{c_0^2}/\gamma$, respectively. Hence, the non-dimensional speed and energy are obtained as

$$u = \frac{\tilde{u}}{\sqrt{\tilde{p_0}/\tilde{\rho_0}}} \ , \ e = \frac{\tilde{e}}{\tilde{p_0}/\tilde{\rho_0}} = \frac{\tilde{e}}{\tilde{R}\tilde{T_0}}. \tag{5.7}$$

The space coordinates were also scaled by the induction length of the steady ZND wave Δ_i (defined as the distance from the shock front to the point where λ_i becomes 1.0) yielding the non-dimensional space coordinates as

$$x = \frac{\tilde{x}}{\tilde{\Delta}_i} \ , \ y = \frac{\tilde{y}}{\tilde{\Delta}_i} \tag{5.8}$$

To keep the governing equations invariant under the non-dimensionalization, the time coordinate should be scaled by $\tilde{\Delta}_i/\sqrt{\tilde{p}_0/\tilde{\rho}_0}$ yielding the non-dimensional time as

$$t = \frac{\tilde{t}\sqrt{\tilde{p}_0/\tilde{\rho}_0}}{\tilde{\Delta}_i} \tag{5.9}$$

and the non-dimensional variables for activation energy and chemical heat release are obtained as

$$E_a = \frac{\tilde{E}_a}{\tilde{R}\tilde{T}_0} \ , \ Q = \frac{\tilde{Q}}{\tilde{R}\tilde{T}_0}. \tag{5.10}$$

5.3 The numerical platform

A numerical solution to the non-dimensional form of the governing system of Equations (5.1) to (5.4) along with (4.32) and (4.33) was obtained using the MG code developed by Professor Sam Falle of the University of Leeds [79, 80]. To solve the partial differential equations and to treat the convective terms, the code uses a second-order accurate exact Godunov scheme. The scheme solves Riemann problems at each inter-cell boundary. Also, the Van Leer limiter is used to correct the fluxes at the cell boundaries.

The reactive dynamics were added to the otherwise inert source code by defining two scalars. These were advected conservatively using the fluxes evaluated from the Riemann solvers. Their respective sources were evaluated by directly evaluating the right hand sides of equations (4.32) and (4.33). Likewise, the energy addition source term was added to the energy equation. This essentially amounted to an explicit formulation for the reactive source terms. Since a high resolution of the reaction zone was otherwise required to capture the cellular dynamics (as described below), the explicit formulation was not restrictive.

The time evolution of the chemical source terms is performed explicitly and coupled to the hydrodynamics by the method of fractional time steps [79]. The appropriate time step is subject to the Courant stability condition by considering the maximum

wave speed in the cell. To make the scheme second order, the code introduces some structure inside the cells to allow the variation of conserved variables U_{ij} over the time step. second order time accuracy is obtained by using the first order scheme to obtain an intermediate solution $U_{ij+\frac{1}{2}}$ at the half-time $t = (t_k + t_{k+1})/2$. This intermediate solution gives a better estimate on the derivatives to solve the flow field across the whole time step. The intermediate solution is then used as input to evolve the solution across the whole time step [80].

The code also features adaptive mesh refinement controlled by user defined differences between the solutions computed at different grid levels. In this regard, a hierarchical series of rectangular Cartesian grids, $G^0, ...G^n$, are used so that grid G^n has the mesh spacing $h/2^n$ where h is the coarse grid size. The advanced solution on the grids G^{n-1} and G^n are compared on a cell-by-cell basis, to decide whether cells on the latter need to be refined. Refinement also occurs in time, so that if the time step on G^0 is Δt, then it is $\Delta t/2^n$ for G^n.

All the solid surfaces are treated by a symmetry boundary condition. The internal boundaries, like the curved wall used in the problem of this thesis, are also implemented directly on the Cartesian grid in a staircase fashion. This appeared as adequate when a sufficiently high resolution was used, as described below. This method is suitable to handle irregular geometries while the computational domain is discretized using a regular Cartesian grid. The method imposes a symmetry boundary condition on each cell surface representing a gas-solid interface.

5.3.1 Benchmarking the code

The modifications to the MG code to include the reactive dynamics were first benchmarked with the results existing in the literature for the pulsating instability of one-dimensional detonations with a two-step chain-branching reaction model previously performed by Short and Sharpe [47]. However, the non-dimensionalization used in this thesis (see Section 5.2.1) differs from those used by Short and Sharpe, and therefore a conversion between the scalings was needed in order to compare the results. The details of the conversion is presented in Appendix B.

In the study of Short and Sharpe [47], the nonlinear dynamics of Chapman-Jouguet pulsating detonations were studied both numerically and theoretically using an asymptotic treatment for the same two-step reaction model used in the present thesis. They performed a parameter study and obtained the stability boundary for the pulsating in-

Table 5.1: Parameters for the stability boundary of one-dimensional pulsating detonations (scalings are with respect to those used in this study)

	E_a	Q	γ	K_r
Short and Sharpe [47]	23.55	4.0	1.4	0.635
This work	23.55	4.0	1.4	0.638

stabilities in terms of the parameters of the problem. The stability boundary found in Short and Sharpe's study is shown in Table 5.1 in terms of the scaling used in this thesis. Short and Sharpe used the parameters $\gamma = 1.4$, $Q = 4.0$, $\nu = 0.5$ and found the stability boundary for a given activation energy E_a by varying K_r. The resolution used by Short and Sharpe typically corresponded to 256 points for the detonation reaction zone length. The resolution used in this study was 64 points per induction length. For parameters $E_a = 23.55$, $\gamma = 1.4$, $Q = 4.0$ and $\nu = 0.5$, the ZND profile is 5.647 times the induction length, and therefore the resolution of 64 points per induction length, corresponds to 361 grid points over the entire detonation reaction zone length. This is slightly more points than was used by Short and Sharpe [47].

Very good agreement was found between the results generated by the code used in this thesis and those generated by Short and Sharpe [47]. Figures 5.1, 5.2 and 5.3 show the evolution of the shock pressure for the K_r values of 0.5, 0.638 and 0.7, respectively. It can be seen that instabilities start to grow at $K_r = 0.638$ and are both amplified and period doubled by increasing the value of K_r to 0.7.

5.4 Cellular detonations in diverging domain

5.4.1 Numerical domain

In the numerical simulations, a diverging domain was adopted. The domain consisted of a constant area zone which was connected to a channel with a diverging cross-sectional area (see Figure 5.4). The length and the height of the domain were 1000 and 100 induction zone lengths, respectively. The length and the height of the constant area zone were 400 and 10 induction zone lengths, respectively. Similar to the experiments performed in Chapter 3, the diverging section of the domain had a cross-sectional area varying exponentially. The channel height in the diverging section was given by:

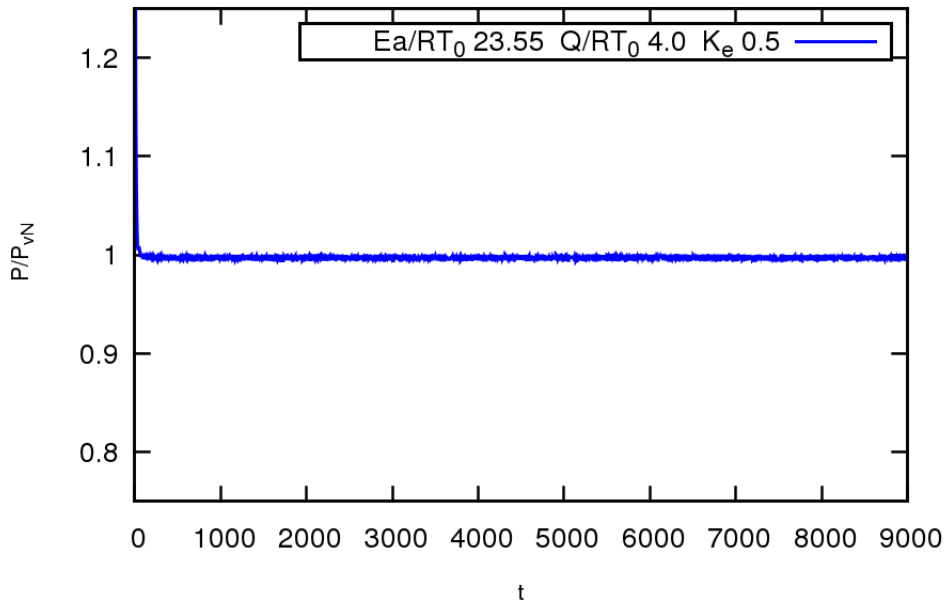

Figure 5.1: The variation of shock pressure normalized by the Von Neumann pressure with respect to time for $E_a = 23.55$, $Q = 4$ and $K_r = 0.5$.

$$y = y_0 e^{K(x-x_0)} \tag{5.11}$$

where K was the area divergence rate of the ramp as defined in Equation (4.21) and x_0 and y_0 denote the coordinates at the beginning of the diverging domain with the values of 400 and 10, respectively.

5.4.2 Initial and boundary conditions

The acetylene-oxygen-argon mixture, with the two-step kinetic parameters extracted and reported in Table 4.1, was adopted for the simulations. A planar blast wave originating from a plane source of energy was prescribed at the beginning of the constant area zone. The energy source was a thin band of gas given a high pressure of 1000 times the initial pressure. Symmetric boundary conditions were prescribed for the walls. As time step progresses, the blast wave originating from the high pressure band decays towards a self-sustained detonation wave. Eventually, a cellular detonation wave propagating in a self-supported manner was established before the beginning of the diverging domain. During the propagation in the diverging section, the dynamics of the detonation wave

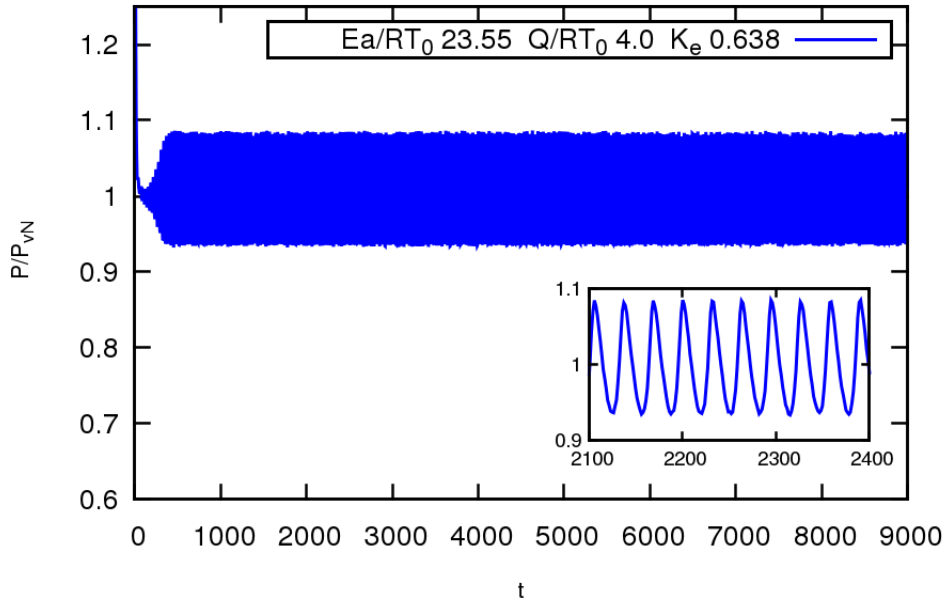

Figure 5.2: The variation of shock pressure normalized by the Von Neumann pressure with respect to time for $E_a = 23.55$, $Q = 4$ and $K_r = 0.638$.

were investigated. Simulations were repeated for different values of the curvature K of the ramp in order to reach the detonation wave extinction limits and the speed measurements were performed for each case. This is equivalent to changing the sensitivity of the mixture by varying its initial pressure in the experiments.

5.4.3 Resolution and grid convergence

Figure 5.5 shows an enlarged view of the mesh used in the simulations. The coarse grid fills the entire domain, but refinement only exists where it is needed. Refinement depends on how rapidly the solution varies. For example, whether a level 2 cell is refined to level 3 depends upon the fractional difference between the level 1 and level 2 solution. If this exceeds a tolerance set to 0.01 in this study, then the cell is refined to level 3. Similarly, refinement to level 4 depends on the difference between levels 2 and 3, and so on. Figures 5.6 and 5.7 show the density and the density gradient plots for the region shown in Figure 5.5. The details of the detonation front, reaction zone and the flow field are shown in these Figures. Comparing Figures 5.5, 5.6 and 5.7 together, it can be seen that in the regions very close to the shock, due to the sharp gradients of the changes in the solution,

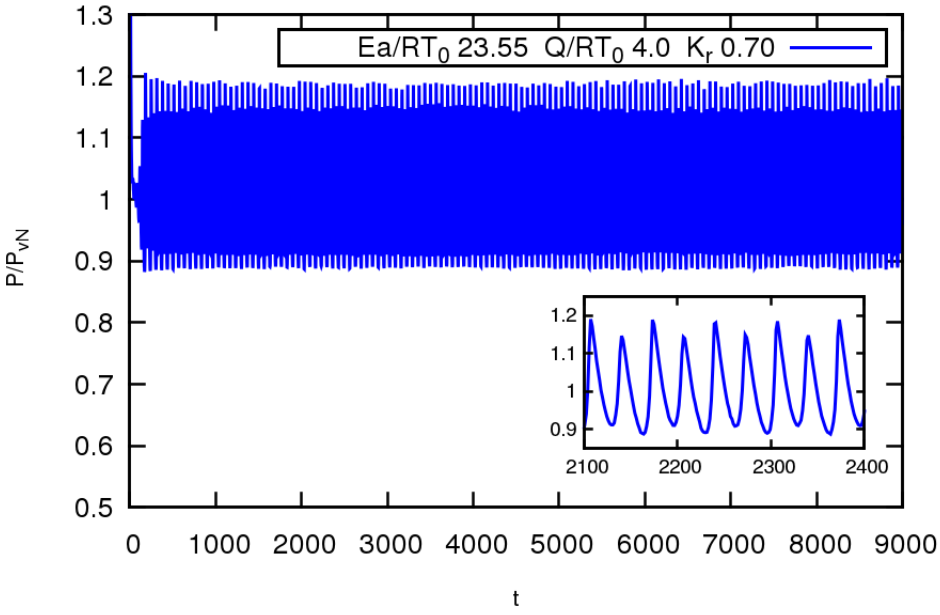

Figure 5.3: The variation of shock pressure normalized by the Von Neumann pressure with respect to time for $E_a = 23.55$, $Q = 4$ and $K_r = 0.7$.

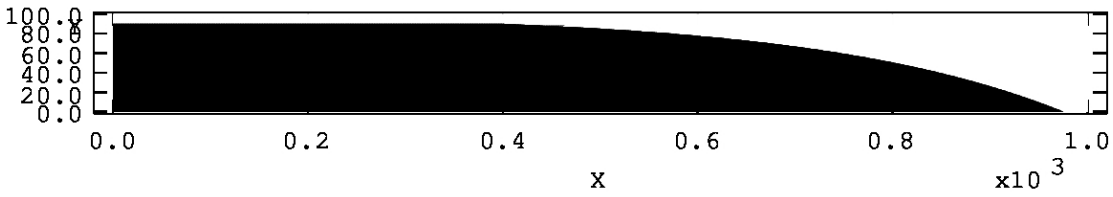

Figure 5.4: The diverging domain adopted for numerical simulations for a value of K=0.003.

the most refined level of grids are employed. As the reaction zone terminates, based on the tolerance adopted for the refinement, less refinement and more coarse grids are employed. As the detonation travels in the diverging domain, the effective resolution per reaction zone length increases due to the enlargement of the reaction zone. It can be seen that for such sufficiently high resolutions no artificially generated wave reflection due to the staircase boundary treatment is observed in the solution and thus the internal boundary treatment is adequate.

To choose the appropriate mesh resolution for the problem, a grid convergence study was performed. In the convergence study, the solution was obtained using different levels of refinement. The characteristic features of the cellular structure obtained for the detonation wave and the speed measurements for the detonation front were compared at these different resolutions. For example, Figure 5.8 shows the numerical open shutter images taken by tracking the maximum rate of chemical energy release rate and thus illustrating the time history of the cellular instabilities for the detonation front. The images were obtained with 3, 4, 5 and 6 levels of refinement in the most refined grid corresponding to 8, 16, 32 and 64 cells per induction zone length, respectively.

As can be seen in Figures 5.8 (a) and (b), resolutions containing 8 and 16 grid point per induction length, have revealed an almost similar sequence of events in terms of the cellular instabilities. In the solutions obtained with these resolutions, for a major part of the diverging section, a single triple point has been captured for the detonation front that is propagating up and down between the domain walls. The solutions obtained using 32 and 64 grid points per induction length have good qualitative level of similarity to each other, revealing more highly resolved events required for the goal of this thesis. For instance, in Figures 5.8 (c) and (d), it can be seen that towards the end of the diverging section, the birth of some newly generated fine scale cells are uncovered which are not seen in Figures 5.8 (a) and (b).

To have a more quantitative comparison, a speed measurement was performed for the solutions obtained using the above mentioned resolutions. Table 5.2 shows the average speed of the detonation front measured along the top wall of the diverging domain for resolutions using 8, 16, 32 and 64 grid points per induction length. It can be seen that the results obtained for the 32 and 64 grid points are identical to the precision reported.

The performed convergence study showed that five refinement levels corresponding to the resolution of 32 grids per induction zone of the non-attenuated detonation permitted me to obtain grid-converged solutions for the acetylene mixture. Based on the above qualitative and quantitative observations about the solutions at different resolutions, the

Table 5.2: Average non-dimensional speed for the two-dimensional cellular detonation wave along the top wall of the diverging domain with K=0.003 at different levels of resolution

Resolution (GPI)	D/D_{CJ}
8	0.93
16	0.94
32	0.92
64	0.92

resolution of 32 grids per induction zone length was adopted for the study. The mesh plot of Figure 5.5 and the flow field solutions of Figures 5.6 and 5.7 correspond to this resolution.

5.5 Simulation results

5.5.1 Flow field evolution

Figure 5.9 shows the numerical density gradient plot (pseudo-Schlieren image) at five sequential time frames of the wave propagation in a channel with divergence rate of $K = 0.002$. The image was obtained by plotting the density gradient for the whole numerical domain. The dark tones in the image therefore correspond to high density gradients. Accordingly, the shock front, the end of the induction zone and the transverse waves are visualized with the dark tone in the image. This Figure shows that the detonation wave was propagating from the left to the right of the channel as required. It can be seen that at the beginning of the ramp, the detonation front has a relatively planar front. As the wave continues to propagate along the domain, due to the flow divergence, it starts to take a small but sensible curvature compared to the early frames.

Increasing the area divergence rate of the channel in another simulation to $K = 0.003$ (see Figure 5.10), reveals that the curvature of the front becomes more obvious. In the early frames, it can be seen that the wave front consists of a single triple point that maintains the detonation mechanism for the wave. However, in the last frame of this sequence, the birth of a new triple point is also observed, which supports the detonation wave even more against the cooling expansion effects that try to quench the detonation. The bulged detonation front of the last frame, with its cellular instabilities can be seen

with more details in the enlarged view of Figure 5.11.

Figure 5.12 shows the evolution of the detonation in a channel with higher area divergence rate, i.e., $K = 0.0035$. The Figure shows that as the detonation wave moves toward the end of the channel, cellular instabilities grow along the front. For instance, in the first three frames, a curved wave with just one cell is seen. The number of the cells increases in the fourth frame. Finally at the end of the ramp, a detonation wave with many cellular instabilities established along its front is observed. In this last frame, a relatively big pocket of unburned gas is seen behind the wave. This can be seen in more detail in Figure 5.13. In this case, the increase in the divergence rate has emphasized the cooling effects and consequently, some gas particles have escaped from being ignited by the shock. These particles have formed a big pocket of unburned gas behind the shock. However, the increase in the birth rate of the triple points still makes the chemical energy release rate more successful in overcoming the cooling effects.

By further increasing the divergence rate of the channel to $K = 0.004$ (see Figures 5.14 and 5.15), the cooling effects become more important. It can be seen in the last frames of the Figure 5.14 that the number of unburned gas pockets has increased. This is shown better in the enlarged view of Figure 5.15. The fourth frame shows a detonation front that experiences a substantial curvature due to the high rate of the flow divergence. In the last frame, some portions of the wave have noticeably thickened reaction zones.

Finally Figure 5.16 shows that by increasing the area divergence rate to $K = 0.006$, the expansion effects completely surpass the chemical energy release rate and succeeds in decoupling the shock front from its reaction zone. The Figure shows that even from the third frame, a big portion of the detonation wave is having a substantially large reaction zone. In the last two frames, the detonation is quenched and just an inert shock wave, very far from its reaction zone, is traveling toward the end of the domain.

Figure 5.17 shows the open shutter images visualizing the evolution of the cellular structure in the mixture for different values of the area divergence rate of the domain. It can be seen that at the beginning of the diverging section, that the cellular structure is textured with very small sized cells. As the detonation travels inside the diverging domain, these small cells enlarge into a bigger half cell. This half cell almost continues toward the end in Figure 5.17 (a). However, in Figures 5.17 (b) and (c)($K = 0.002$ and $K = 0.0035$), at the ending section of the channel, the birth of some newly generated smaller cells within this large cell is observed. This corresponds to the generation of some new high temperature triple points that are favoring the chemical reactions and energy release rates to overcome the divergence. Figure 5.17 (d) shows that after the detonation

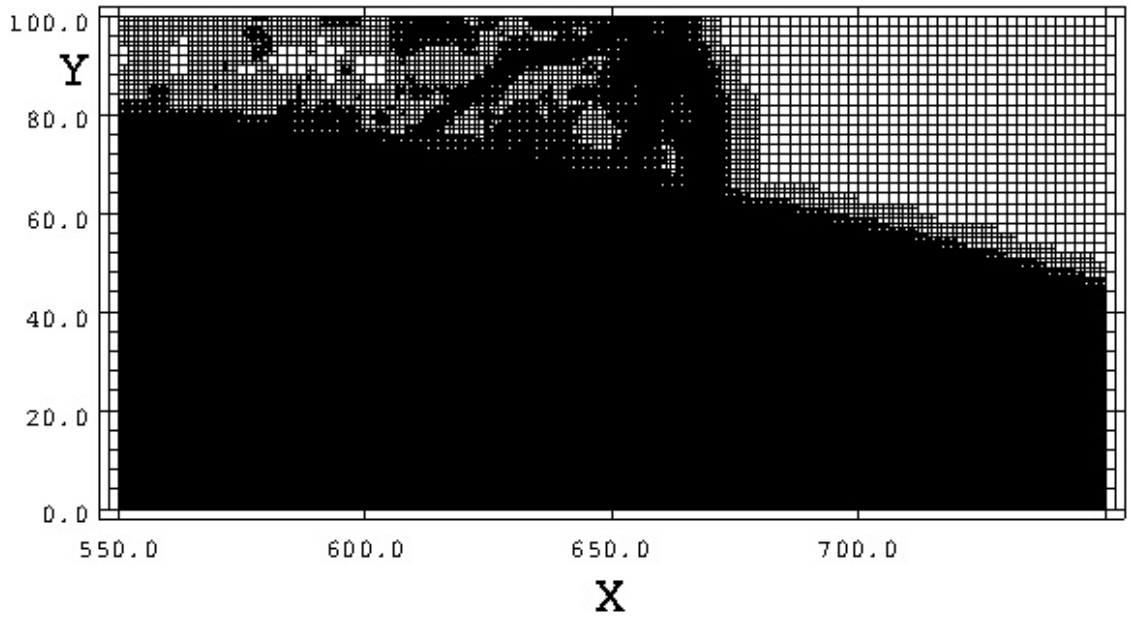

Figure 5.5: The structure of the mesh and the stair-case solid boundary used for the numerical simulation of two-dimensional cellular detonations in the diverging domain.

wave travels a certain distance in the diverging section, that the cells start to disappear. The disappearance of the cellular structure corresponds to the shock front being deprived of any cellular instabilities. Consequently, the shock front is unable to sustain the necessary detonation mechanisms and therefore the disappearance or quenching of the cellular structure marks the extinction of the detonation.

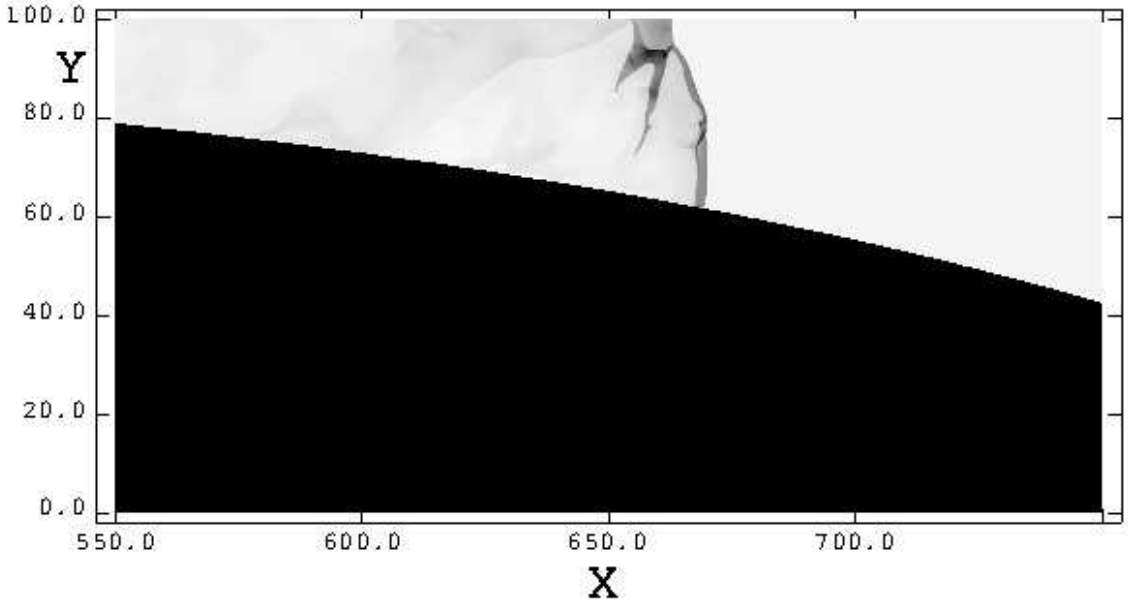

Figure 5.6: The two-dimensional density plot for a region surrounding the cellular detonation wave while propagating in the diverging domain.

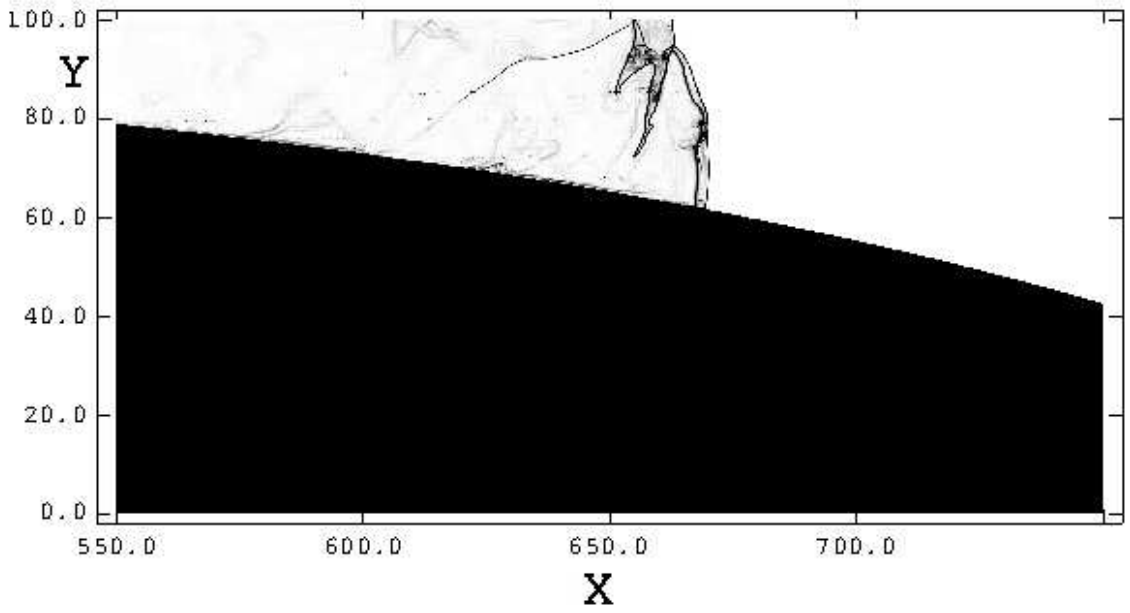

Figure 5.7: The two-dimensional density gradient plot for a region surrounding the cellular detonation wave while propagating in the diverging domain.

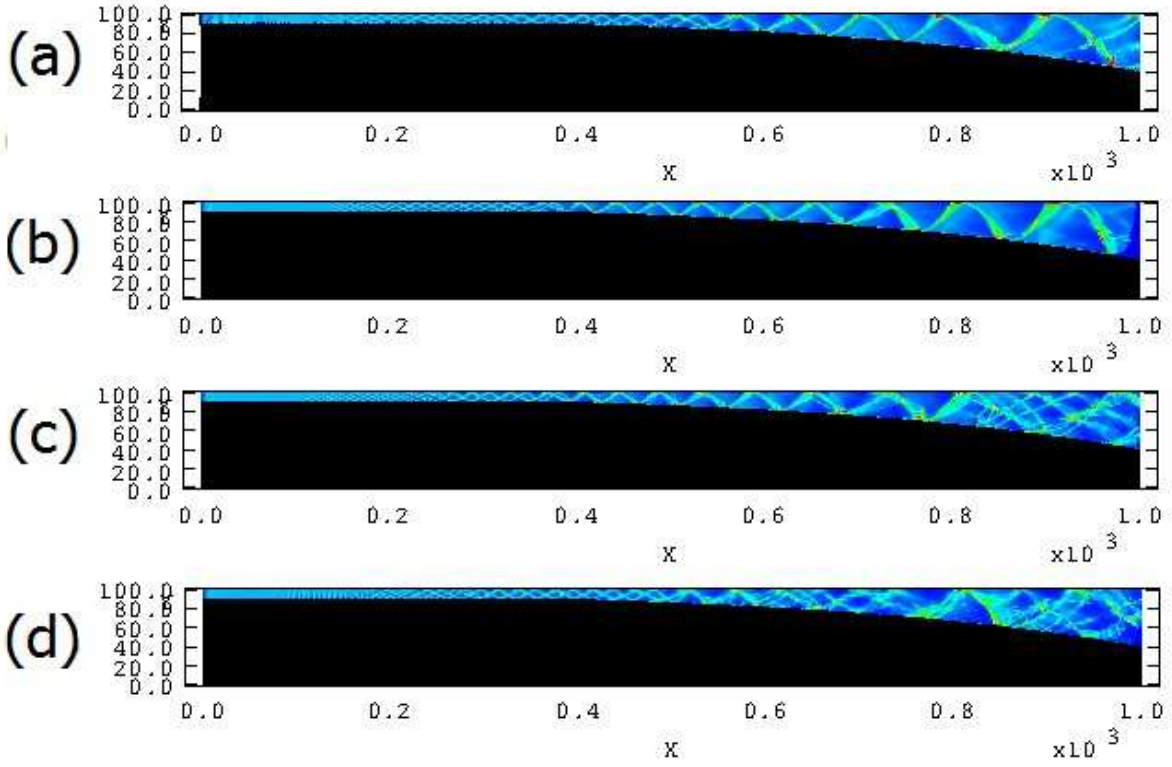

Figure 5.8: The open shutter images (tracks of maximum rate of energy release) for K=0.003 obtained at resolutions with (a) 8, (b) 16, (c) 32, (d) 64 grid points per induction zone length.

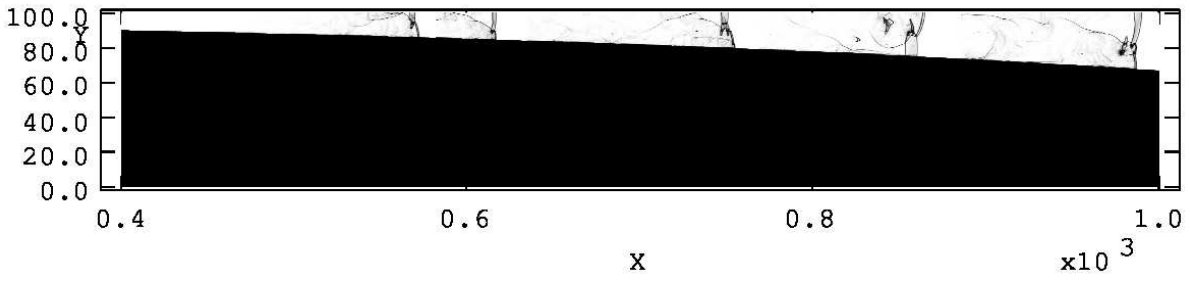

Figure 5.9: The evolution of the detonation wave dynamics in the diverging channel with $K = 0.002$ obtained by superpositioning of Schlieren images at different time steps.

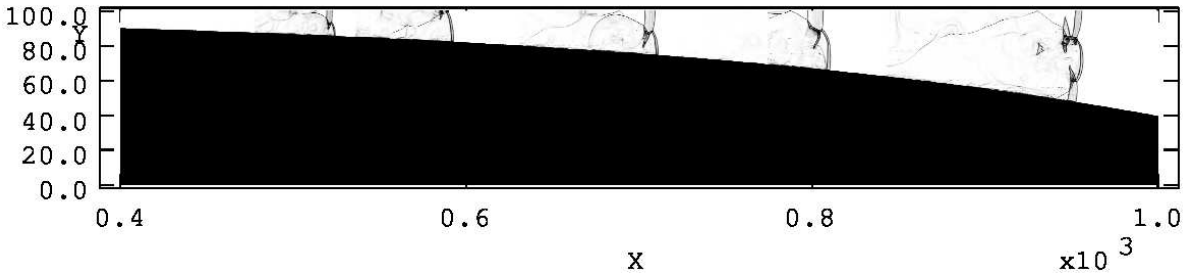

Figure 5.10: The evolution of the detonation wave dynamics in the diverging channel with $K = 0.003$ obtained by superpositioning of Schlieren images at different time steps.

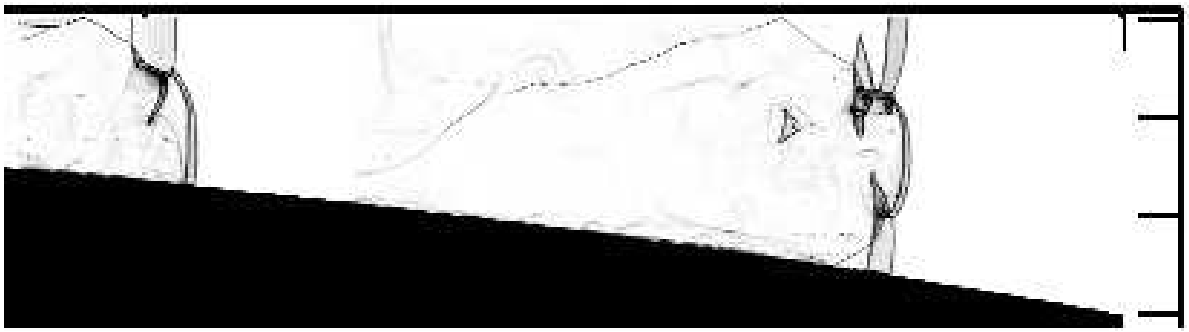

Figure 5.11: A zoomed view with more details for the last frames of Figure 5.10.

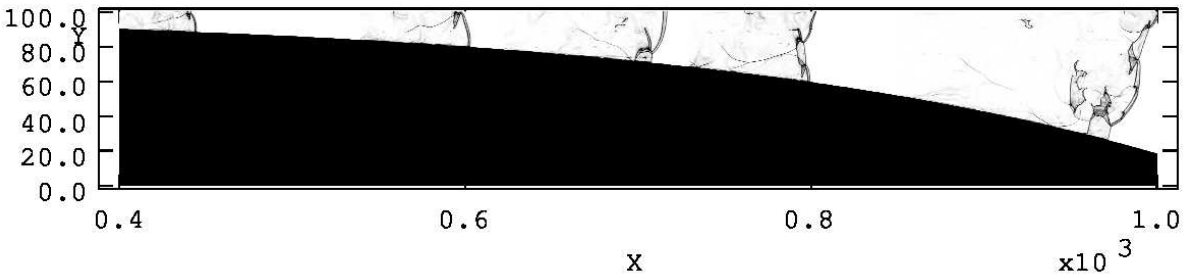

Figure 5.12: The evolution of the detonation wave dynamics in the diverging channel with $K = 0.0035$ obtained by superpositioning of Schlieren images at different time steps.

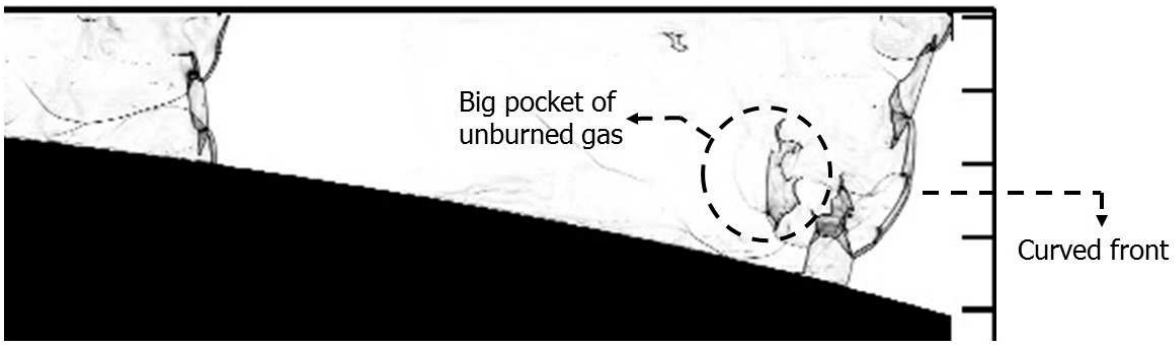

Figure 5.13: Curved detonation front with a big pocket of unburned gas behind it for the detonation wave close to the end of diverging domain with $K = 0.0035$ (a zoomed view with more details for the last frames of Figure 5.12).

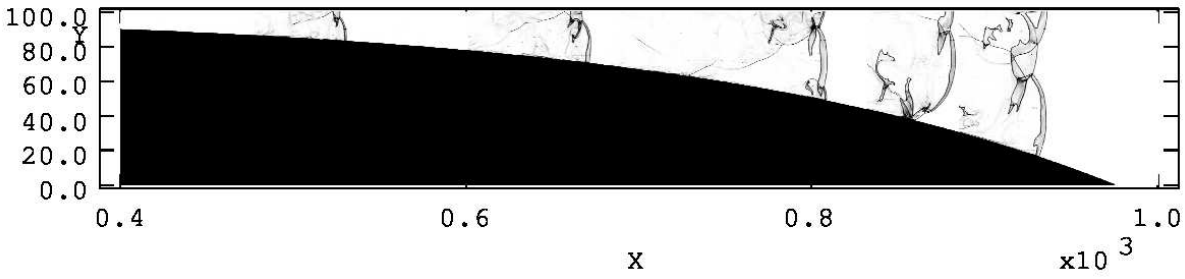

Figure 5.14: The evolution of the detonation wave dynamics in the diverging channel with $K = 0.004$ obtained by superpositioning of Schlieren images at different time steps.

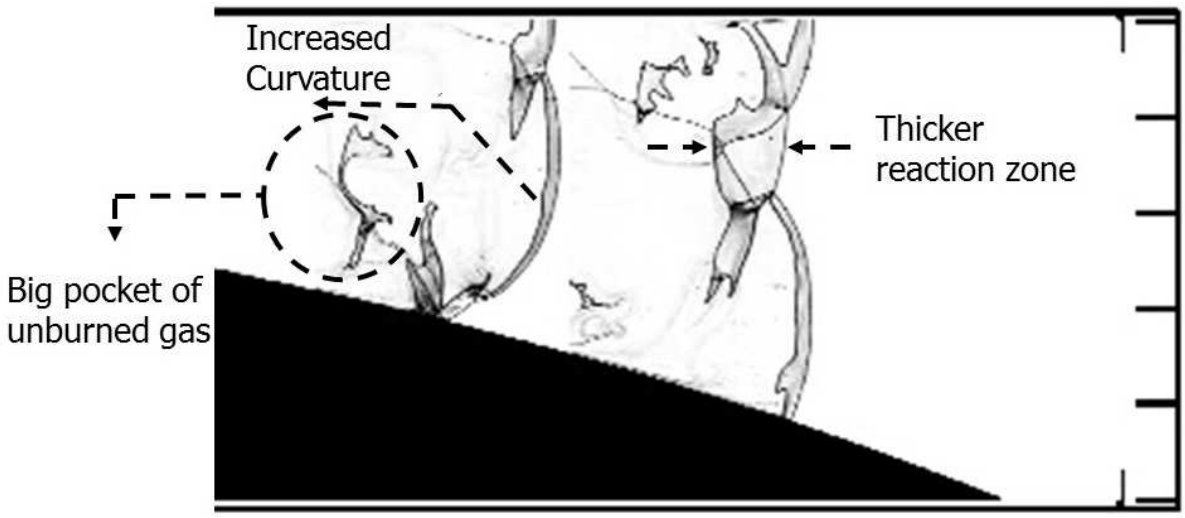

Figure 5.15: Thickening of reaction zone and increase in front curvature for the detonation wave close to the end of diverging domain with $K = 0.004$ (a zoomed view with more details for the last frames of Figure 5.14).

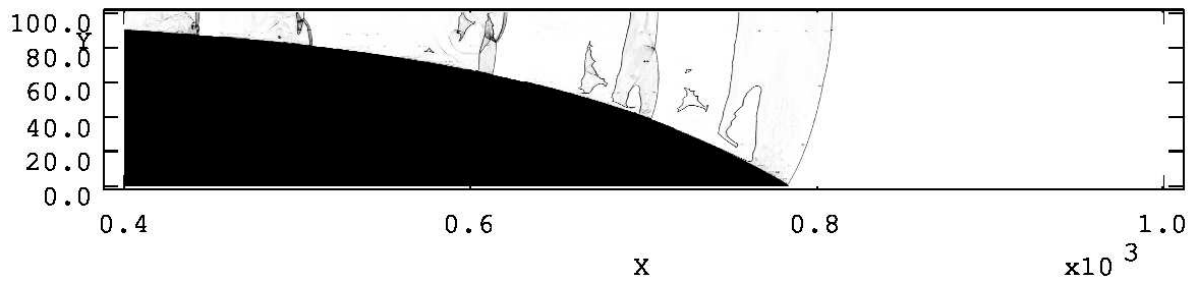

Figure 5.16: The extinction of the detonation wave in the diverging channel with $K = 0.006$ (image obtained by superpositioning of Schlieren images at different time steps).

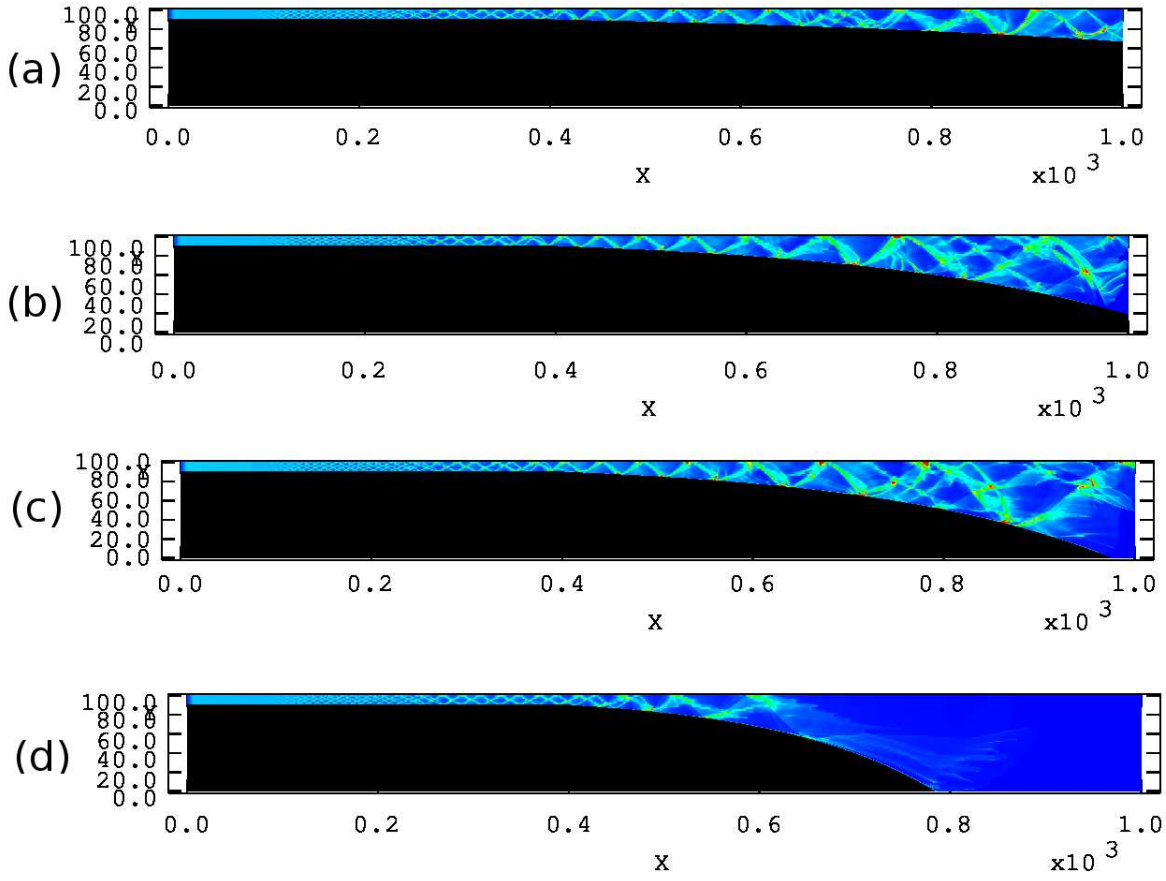

Figure 5.17: Time history of the cellular detonation structure obtained by tracking the maximum energy release rate for (a) $K = 0.002$, (b) $K = 0.0035$, (c) $K = 0.004$ and (d) $K = 0.006$ for the acetylene mixture.

Chapter 6

Discussion of the results

6.1 Overview

This chapter provides a comparison of the experimental results with the steady model formulated and the results of the non-steady cellular-dynamics simulations. The quantitative comparison between the detonation speed dependence on mass divergence is performed. On this basis, arguments on the role of the cellular structure in promoting the dynamics of detonations with mass divergence are presented. Finally, the contributions to original knowledge are presented and recommendations for future work are provided.

6.2 $D - K$ characteristic curves

The dynamics of detonations with constant mass divergence were investigated using different methods. In Chapter 3, detonations with constant mass divergence were studied experimentally for a weakly unstable and a highly unstable reactive mixture. In Chapter 4, a steady one-dimensional solution for the dynamics of detonations with mass divergence was obtained. Chapter 5 presented results of a numerical study on two-dimensional cellular detonations in diverging channels. Having a quantitative comparison between the results of these different methods would give a better insight and understanding on the influence of cellular structure of detonations with mass divergence, on their dynamics and propagation.

For instance, since the quasi-one-dimensional ZND model presented in Chapter 4 neglected the existence of cellular structure of detonations, comparing its predictions of

dynamics with what observed experimentally in Chapter 3 isolates the role of the cellular structure on the dynamics. Comparing these two sets of results with the ones obtained from numerical simulations of cellular detonations also gives a better estimate on how the predictions change by adding the unstable cellular features of detonations to the model.

6.2.1 Reduction of experimental data

Mass divergence rate due to boundary layers

The results of Chapter 4 showed that the dynamics of detonations with mass divergence can be uniquely scaled to obtain a non-dimensional detonation speed - mass divergence relation, as anticipated from literature [58, 56, 57, 59]. The experimental results were thus reduced in the same fashion.

The total mass divergence rate experienced by the detonation wave in the experiments described herein is due to the area divergence due to the diverging channel and the divergence of the flow to the boundary layers on the channel walls. In this regard, and in addition to the expansion losses, the contribution of the boundary layer losses inherent in a thin channel should be considered in this analysis. This is done by introducing an effective mass divergence rate to include both the expansion and boundary layer losses as

$$K_{eff} = \frac{1}{A}\frac{dA}{dx} + \phi_{BL} \tag{6.1}$$

where $\frac{1}{A}\frac{dA}{dx}$ denotes the expansion loss rate due to the area divergence of the channel and ϕ_{BL} represents the mass divergence rate due to the boundary layers' effect on the walls of the channel.

In this analysis, the contribution of the boundary layers losses' ϕ_{BL} has been obtained experimentally by comparing the experiments performed on the two ramps (in the same mixture) and calibrating the effective rate of mass divergence K_{eff} to obtain a unique relation between speed deficit and loss rate. Figure 6.1 shows the detonation speed normalized by the CJ speed plotted with respect to the non-dimensional expansion loss rate $\frac{1}{A}\frac{dA}{dx}\Delta_i$ for the acetylene experiments. It can be seen that since the influence of the boundary layer losses has not been considered in this plot, there is not a unique identical relation between the speed deficit and the loss rate for both large and small ramp data points. However, Figure 6.2 shows that by calibrating the effective rate of mass divergence with an appropriate value for the boundary layers losses ϕ_{BL}, a unique

and identical relation can be found between the speed deficit and the non-dimensional mass divergence rate $K_{eff}\Delta_i$ for all the experimental data obtained. In this work, the value of $\phi_{BL} = 5.48m^{-1}$ was found to offer the best fitting for the experimental data obtained from both the small and the large ramps. Figure 6.2 shows that, as expected, by increasing the total mass divergence rate the speed of the detonation wave decays. Based on the experiments performed for the acetylene mixture, the graph shows that the extinction limits of the detonation wave in the acetylene mixture is met by reaching $K_{eff}\Delta_i = 7.6 \times 10^{-3}$, which corresponds to a 24% speed deficit with respect to the CJ speed.

In the same fashion, Figure 6.3 shows the variation of the detonation speed with respect to the expansion rate $\frac{1}{A}\frac{dA}{dx}\Delta_i$ for the propane mixture experiments. To account for the boundary layer mass divergence in propane mixture, the same value of $\phi_{BL} = 5.48m^{-1}$ offered the unique fit between the experimental results. The $\frac{D}{D_{CJ}} - K_{eff}\Delta_i$ characteristic curve obtained for the propane mixture is presented in Figure 6.4. Figure 6.4 shows that the experimental extinction limit found for the propane mixture happens at $K_{eff}\Delta_i = 7.9 \times 10^{-3}$, which corresponds to 25% of speed deficit with respect to the CJ speed.

6.2.2 Quantitative comparison

After accounting for the boundary layer losses in the experiments, the experimental results were compared with the predictions of dynamics based on the quasi-one-dimensional ZND model and the two-dimensional cellular simulations. The $\frac{D}{D_{CJ}} - K$ characteristic curves were obtained and presented in Chapter 4 for both mixtures. Also, for the cellular simulations performed in Chapter 5, the $\frac{D}{D_{CJ}} - K$ characteristic curves were constructed. This was done by measuring the average shock front speed along the top wall from the beginning of the diverging section toward the end of the numerical domain.

The results of such comparison can be seen in Figure 6.5 for the acetylene mixture. The Figure shows that for such a weakly unstable mixture that there is a relatively good agreement between the experimental limiting value of the mass divergence K^* and its prediction in the ZND model. However, it can be seen that for a given mass divergence, the ZND model predicts a higher value of detonation speed compared to the experimental values by about $2 \sim 5\%$. Such a quantitative agreement between the experiments and the ZND predictions indicates that the failure mechanism in the weakly unstable mixtures in the experiments is consistent with the limits of curved ZND detonations, where the

Table 6.1: Qunatitative comparison between the experimental and the predicted mass divergence limits for acetelyne and propane mixtures

Mixture	$(K_{eff}\Delta_i)^*_{experiment}$	K^*_{ZND}	$\frac{K^*_{ZND}-(K_{eff}\Delta_i)^*_{experiment}}{(K_{eff}\Delta_i)^*_{experiment}} \times 100\%$
$2C_2H_2 + 5O_2 + 21Ar$	7.6×10^{-3}	7.4×10^{-3}	2.6%
$C_3H_8 + 5O_2$	7.9×10^{-3}	1.3×10^{-3}	92.6%

existence of cellular structure is neglected. For smaller values of the mass divergence rate, a good agreement between the experiments and the predictions of the two-dimensional cellular simulations can be seen.

A similar comparison for the highly unstable (propane) mixture has also been performed. For the unstable mixture, inviscid simulations have not been attempted in this thesis, owing to the intrinsic difficulties associated with numerical diffusion in highly unstable detonations [9]. Such simulations for the highly unstable detonations could be performed in the future by adopting appropriate turbulence models which could provide the correct burn rates. Accordingly, Figure 6.6 shows the $\frac{D}{D_{CJ}} - K_{eff}\Delta_i$ characteristic curves constructed using the experiments and the quasi-one-dimensional ZND model for the propane mixture. It can be seen that there is a substantial difference between the experiments and the ZND model prediction for this mixture. The experimental speed is larger than predicted for a given mass divergence. The experimental limiting value of the mass divergence is systematically higher than the predicted one by 75%, while maximum speed deficit is also much larger in the experiment. These large discrepancies, and the fact that the losses are over-predicted by the quasi-one-dimensional model indicates that another mechanism such as the cellular structure plays a more important role. This indicates the inadequacy of the steady ZND model, which neglects cellular instabilities, to capture the failure mechanism in highly unstable mixtures. Tables 6.1 and 6.2 summarize the quantitative comparison performed in Figures 6.5 and 6.6.

6.3 Summary

The present research studied the influence of the cellular structure on the dynamics of detonations with constant mass divergence. In this regard and in order to quantify this influence, the dynamics of real detonations with constant mass divergence were com-

Table 6.2: Qunatitative comparison between the experimental and the predicted detonation velocity limits for acetelyne and propane mixtures

Mixture	$(\frac{D_{exp}}{D_{CJ}})^*$	$(\frac{D_{ZND}}{D_{CJ}})^*$	$\left\lvert\frac{(\frac{D_{exp}}{D_{CJ}})^* - (\frac{D_{ZND}}{D_{CJ}})^*}{(\frac{D_{exp}}{D_{CJ}})^*}\right\rvert \times 100\%$
$2C_2H_2 + 5O_2 + 21Ar$	0.77	0.86	10.5%
$C_3H_8 + 5O_2$	0.75	0.94	25.3%

pared with the predictions based on the quasi-one-dimensional ZND model and multi-dimensional cellular simulations. Since the ZND model neglects the existence of cellular structure of detonations, such comparison permitted to assess the role of cellular structure on the dynamics of detonations with constant mass divergence. Accordingly, the dynamics of real detonations with constant mass divergence were studied through experiments with acetylene-oxygen-argon ($2C_2H_2 + 5O_2 + 21Ar$) and propane-oxygen ($C_3H_8 + 5O_2$), as mixtures representing weakly unstable and highly unstable detonations. To study the dynamics quantitatively, the speed deficit of the detonation wave was studied with respect to the non-dimensional rate of mass divergence in the experiments. Accordingly, by accounting for both the expansion and boundary layer losses, the $\frac{D}{D_{CJ}} - K_{eff}\Delta_i$ characteristic curves were constructed for each of the mixtures. Quantitative analysis of the experiments showed that the speed deficit increases with the rate of mass divergence. Both mixtures showed approximately the same behaviour, with maximum speed deficits of approximately 20%. The limiting maximum mass divergence rates beyond which detonations are quenched were also similar for both mixtures.

The speed deficits measured in the experiments were then compared with an estimate of the speed deficit obtained from the quasi-one-dimensional ZND model with lateral mass divergence. In this regard, the ZND appraisal of the speed deficit with respect to the rate of mass divergence was calculated for both mixtures. Finally, to focus in more detail on the influence of cellular structure on the dynamics and limits of the detonation waves, numerical simulations of the cellular simulations were added to provide the comparison of the cellular structure effect.

The ZND model was found to predict well the extinction limit obtained experimentally, although the speed deficits were poorly estimated. However, for the more unstable propane mixture, a much more substantial difference between the experiments and the model prediction was observed. Such observations clearly highlight the inadequacy of the ZND model to predict the dynamics of detonations with mass divergence. For un-

stable mixtures, the predictions are significantly different. This indicates the failure of quasi-one-dimensional ZND model to adequately capture the physics and chemistry of the process.

6.4 Contributions to original knowledge

As reviewed in Chapter 1, previous attempts to isolate the role of the cellular dynamics have been performed in geometries like narrow tubes, porous walled tubes and weakly confined media. These attempts have been successful in demonstrating that a global hydrodynamic description appears worthwhile for weakly unstable detonations. They have also indicated that departures are expected for more unstable detonations. However, they have all been associated with difficulties of being able to precisely quantify the loss mechanism. Such difficulties limit their comparisons between the theory and experiments to qualitative ones.

The current thesis has contributed to the original knowledge by formulating a problem in which the loss mechanism can be easily accounted for and unambiguous experiments, simulations and analytical models can be formulated in order to evaluate the utility of the global models for detonation dynamics. Performing the experiments in the presence of a controlled rate of loss by adopting the diverging geometry introduced in this thesis also provided a meaningful framework for comparison of the results with the currently existing quasi-steady models and with direct numerical simulations.

The results of the quantitative appraisal performed in this thesis clearly showed that only a very special class of detonations can be relatively well approximated by the classical ZND model, i.e, mixtures characterized by regular cellular structures (or weakly unstable mixtures). The fundamentally different burning mechanisms in highly unstable detonations from what is assumed by the ZND model result in remarkable discrepancies between reality and ZND predictions of the dynamics.

In addition, the current thesis also presented a quantitative comparison between the real dynamics, predictions of the ZND model for a typical weakly unstable mixture and cellular detonation simulations. The simulations showed a good agreement for weakly curved detonations, but larger departures were found near the limits.

6.5 Suggestions and recommendations for future works

In view of the main contributions of the present thesis, the author makes the following recommendations for future work:

1. Numerical simulations of highly unstable detonations.
   Owing to the intrinsic difficulties associated with numerical diffusion in highly unstable detonations, the current thesis has not attempted to conduct inviscid calculations for the numerical simulations for highly unstable cellular detonations. Accordingly, performing cellular simulations which prescribe burning rates recovered by appropriate turbulent models could also contribute to this study. Adding such results to the comparisons performed in this thesis, could give a quantitative estimate on the accuracy and/or validity of such numerical simulations predictions of the dynamics of highly unstable detonations.

2. Developing/calibrating meso-scale models for the detonation structure.
   The above mentioned deficiencies for one-dimensional models and the impossibility of DNS for large scale problems necessitate the formulation of meso-scale models for the reaction zone structure of detonations, inherently accounting for the wave instability [81]. The experimental technique introduced in the present thesis can generate well defined $\frac{D}{D_{CJ}} - K_{eff}\Delta_i$ curves for a range of reactive mixtures. These experimental results would then permit one to validate and/or calibrate models for the reaction zone structure.

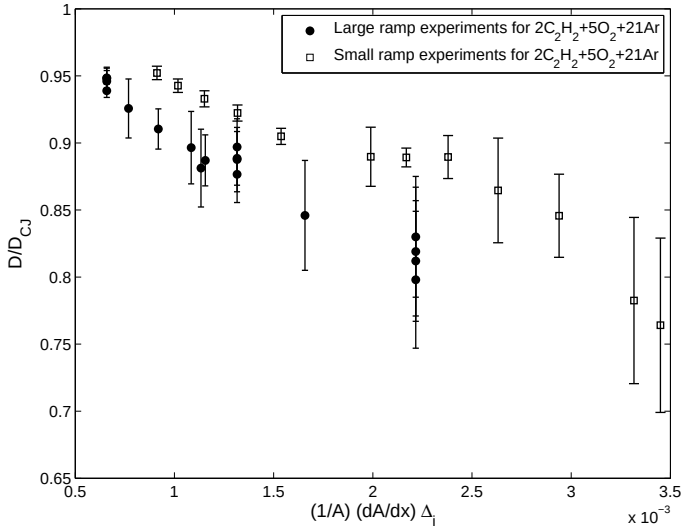

Figure 6.1: Normalized detonation speed $\frac{D}{D_{CJ}}$with respect to normalized expansion loss rate $\frac{1}{A}\frac{dA}{dx}\Delta_i$ for $2C_2H_2 + 5O_2 + 21Ar$ experiments.

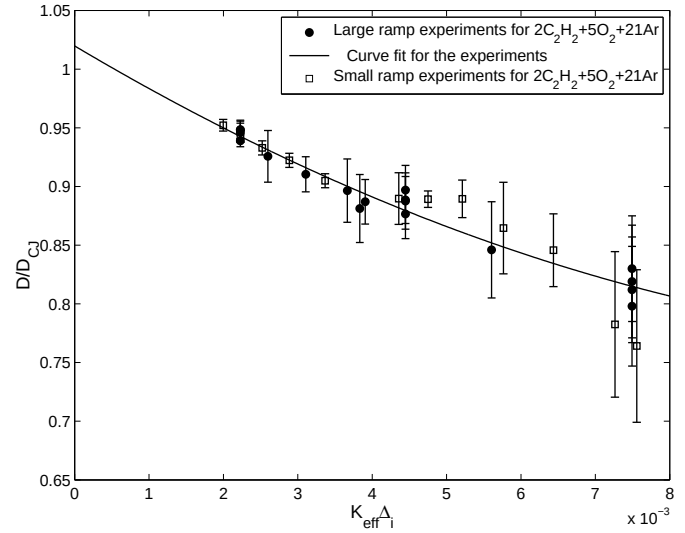

Figure 6.2: Normalized detonation speed $\frac{D}{D_{CJ}}$with respect to non-dimensional effective mass divergence rate $K_{eff}\Delta_i$ for $2C_2H_2 + 5O_2 + 21Ar$ experiments.

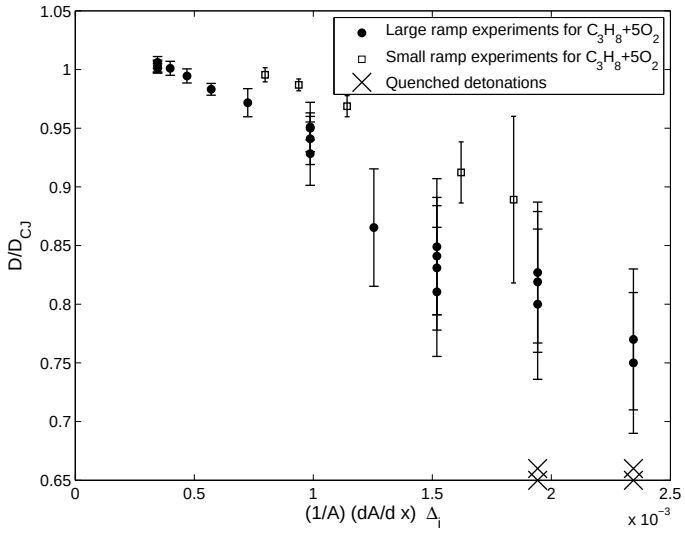

Figure 6.3: Normalized detonation speed $\frac{D}{D_{CJ}}$with respect to normalized expansion loss rate $\frac{1}{A}\frac{dA}{dx}\Delta_i$ for $C_3H_8 + 5O_2$ experiments.

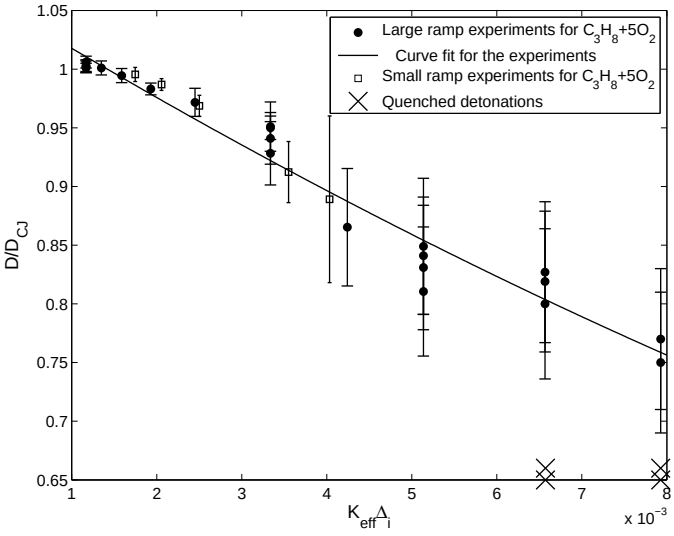

Figure 6.4: Normalized detonation speed $\frac{D}{D_{CJ}}$with respect to non-dimensional effective mass divergence rate $K_{eff}\Delta_i$ for $C_3H_8 + 5O_2$ experiments.

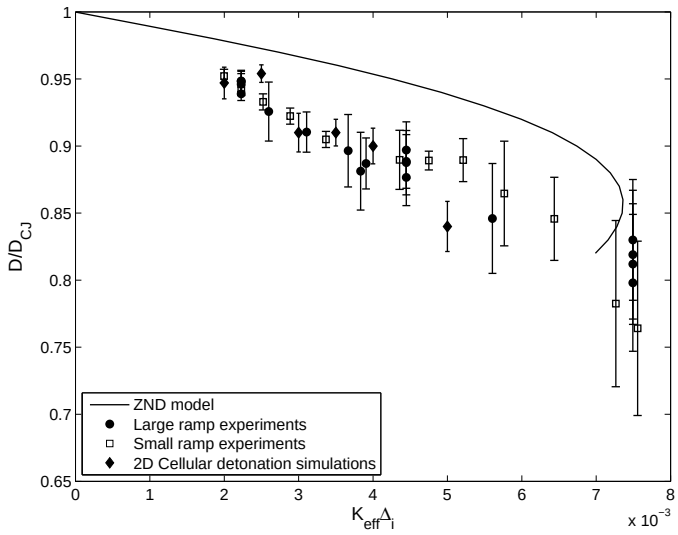

Figure 6.5: The $\frac{D}{D_{CJ}} - K_{eff}\Delta_i$ characteristic curves for the $2C_2H_2 + 5O_2 + 21Ar$ mixture constructed using the experimental data, quasi-one-dimensional ZND model and cellular simulations.

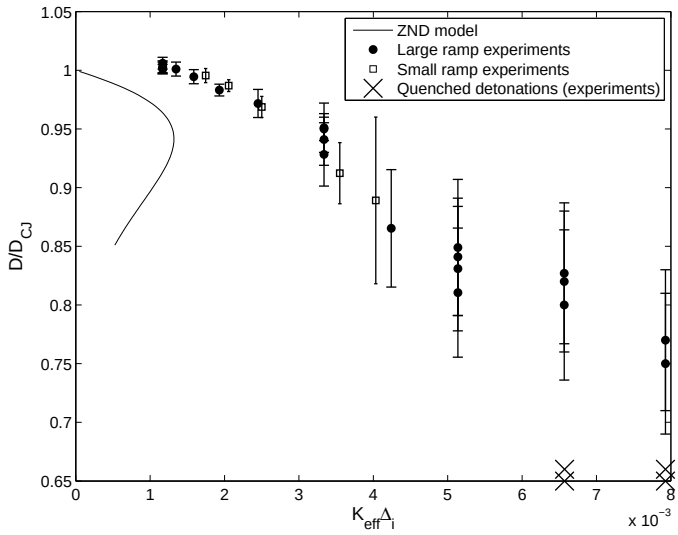

Figure 6.6: The $\frac{D}{D_{CJ}} - K_{eff}\Delta_i$ characteristic curves for the $C_3H_8 + 5O_2$ mixture constructed using the experimental data and the quasi-one-dimensional ZND model predictions.

Appendix A

Detonation speed measurement for the experiments

A.1 Overview

This Appendix presents details of the analysis performed on my experiments to study the dynamics of detonations with constant mass divergence. Accordingly, the details of the method used for the speed measurements along with the detonation wave speed measured for the experiments are reported in this appendix.

A.2 Detonation wave speed measurements

As explained in Chapter 2, in order to investigate the dynamics of detonations with constant mass divergence quantitatively, detonation wave speed measurements were performed in the analysis of the experiments. In order to measure the detonation wave speed, the videos taken from the experiments were dissected to their combinatory frames. Through processing of these images, the shock front location was detected in each of the frames. Also, the time interval between the frames was obtained from the frame per second rate used for capturing the video. Knowing the shock location in each frame along the top wall and the time interval between the frames, permitted me to estimate the shock speed using two subsequent frames.

The calculation sheets shown in Figures A.1 to A.33 show the details of such speed measurements. It can be seen that the frame per second rate of the videos are reported in the calculation sheet. In these calculation sheets, each row, represents a single frame

of the video taken from the experiments. In each frame, the location of the shock is detected in pixels along the top wall of the diverging channel and its location is denoted by the x symbol in the first column (e.g. x=147, 190, etc.). Also, the shock front displacement is measured by calculating the distance between its location in sequential frames. The distances in pixels are also converted to a physical scale by using a known reference length in the images (e.g. ramp length, etc.). The speed obtained by dividing the displacement by the time interval between the frames was also normalized by the CJ speed. The variation of this shock front speed with respect to the front's relative position along the ramp is shown for each of the experiments in Figures A.1 to A.33. Also an average speed along the top wall of the diverging domain was calculated for each experiment. This value is also reported in the calculation sheet of the experiments.

X	Y	Delta_x	Delta_x(m)	FPS	V	Ramp End_X	Ramp End_y	Delta_x_Relative to ramp	D_CJ
147	14			42049		1136	236	0.113	1703.7
190	14	43	0.039	42049	0.952	1136	236	0.151	
233	14	43	0.039	42049	0.952	1136	236	0.190	V_ave
275	14	42	0.038	42049	0.930	1136	236	0.228	0.938915597
318	14	43	0.039	42049	0.952	1136	236	0.266	
360	14	42	0.038	42049	0.930	1136	236	0.304	x_ref
402	14	42	0.038	42049	0.930	1136	236	0.342	1130
444	14	42	0.038	42049	0.930	1136	236	0.379	592
486	14	42	0.038	42049	0.930	1136	236	0.417	Deltax_ref (pixels)
528	14	42	0.038	42049	0.930	1136	236	0.455	538
612	14	84	0.075	21025	0.930	1136	236	0.530	
655	14	43	0.039	42049	0.952	1136	236	0.569	y_ref
698	14	43	0.039	42049	0.952	1136	236	0.607	45
741	14	43	0.039	42049	0.952	1136	236	0.646	45
783	14	42	0.038	42049	0.930	1136	236	0.683	Deltax_ref (inches)
826	14	43	0.039	42049	0.952	1136	236	0.722	19
869	14	43	0.039	42049	0.952	1136	236	0.760	
911	14	42	0.038	42049	0.930	1136	236	0.798	pxl -> m conv. Rate
953	14	42	0.038	42049	0.930	1136	236	0.836	0.000897026
995	14	42	0.038	42049	0.930	1136	236	0.874	
1038	14	43	0.039	42049	0.952	1136	236	0.912	
1080	14	42	0.038	42049	0.930	1136	236	0.950	

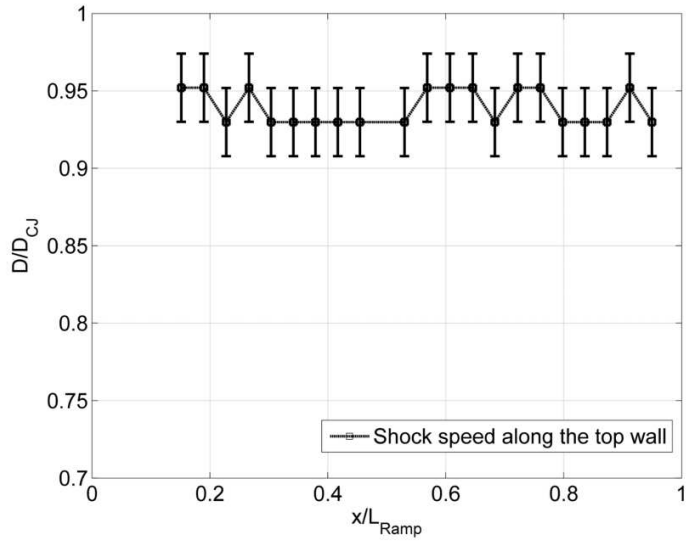

Figure A.1: Normalized detonation speed $\frac{D}{D_{CJ}}$ calculation and variation along the large ramp for acetylene mixture $2C_2H_2 + 5O_2 + 21Ar$ at 13.8 kPa.

X	Y	Delta_x	Delta_x(m)	FPS	V	Ramp End_X	Ramp End_y	Delta_x_Relative to ramp	D_CJ
132	14			42049		1136	236	0.099	1698.9
174	14	42	0.038	42049	0.932	1136	236	0.137	
216	14	42	0.038	42049	0.932	1136	236	0.175	V_ave
257	14	41	0.037	42049	0.910	1136	236	0.212	0.967807145
298	14	41	0.037	42049	0.910	1136	236	0.248	
339	14	41	0.037	42049	0.910	1136	236	0.285	x_ref
381	14	42	0.038	42049	0.932	1136	236	0.323	1130
424	14	43	0.039	42049	0.955	1136	236	0.361	592
467	14	43	0.039	42049	0.955	1136	236	0.400	Deltax_ref (pixels)
509	14	42	0.038	42049	0.932	1136	236	0.438	538
634	14	125	0.112	14016	0.925	1136	236	0.550	
674	14	40	0.036	42049	0.888	1136	236	0.586	y_ref
714	14	40	0.036	42049	0.888	1136	236	0.621	45
760	14	46	0.041	42049	1.021	1136	236	0.663	45
801	14	41	0.037	42049	0.910	1136	236	0.699	Deltax_ref (inches)
841	14	40	0.036	42049	0.888	1136	236	0.735	19
881	14	40	0.036	42049	0.888	1136	236	0.771	
924	14	43	0.039	42049	0.955	1136	236	0.810	pxl -> m conv. Rate
965	14	41	0.037	42049	0.910	1136	236	0.847	0.000897026
1006	14	41	0.037	42049	0.910	1136	236	0.883	
1048	14	42	0.038	42049	0.932	1136	236	0.921	
1091	14	43	0.039	42049	0.955	1136	236	0.960	

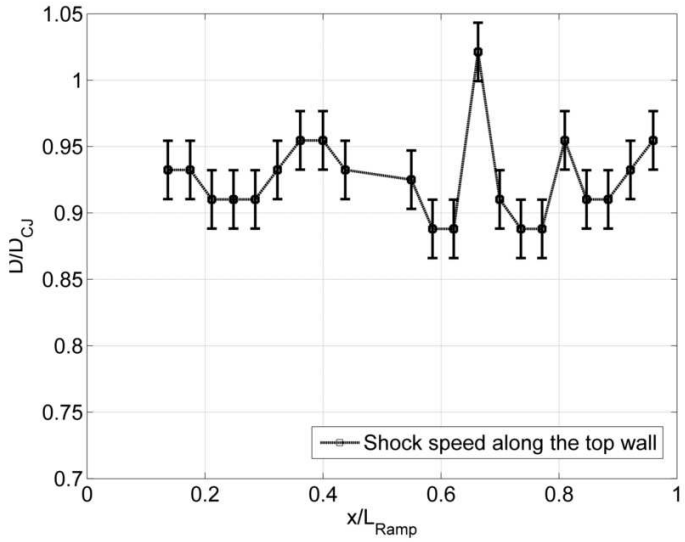

Figure A.2: Normalized detonation speed $\frac{D}{D_{CJ}}$ calculation and variation along the large ramp for acetylene mixture $2C_2H_2 + 5O_2 + 21Ar$ at 12.1 kPa.

X	Y	Delta_x	Delta_x(m)	FPS	V	Ramp End_X	Ramp End_y	Delta_x_Relative to ramp	D_CJ
114	14			42049		1136	236	0.083	1693.5
156	14	42	0.038	42049	0.935	1136	236	0.121	
198	14	42	0.038	42049	0.935	1136	236	0.159	V_ave
240	14	42	0.038	42049	0.935	1136	236	0.196	0.910402158
281	14	41	0.037	42049	0.913	1136	236	0.233	
322	14	41	0.037	42049	0.913	1136	236	0.270	x_ref
363	14	41	0.037	42049	0.913	1136	236	0.307	1130
404	14	41	0.037	42049	0.913	1136	236	0.343	592
445	14	41	0.037	42049	0.913	1136	236	0.380	Deltax_ref (pixels)
486	14	41	0.037	42049	0.913	1136	236	0.417	538
527	14	41	0.037	42049	0.913	1136	236	0.454	
609	14	82	0.074	21025	0.913	1136	236	0.527	y_ref
647	14	38	0.034	42049	0.846	1136	236	0.561	45
688	14	41	0.037	42049	0.913	1136	236	0.598	45
731	14	43	0.039	42049	0.958	1136	236	0.637	Deltax_ref (inches)
771	14	40	0.036	42049	0.891	1136	236	0.673	19
809	14	38	0.034	42049	0.846	1136	236	0.707	
848	14	39	0.035	42049	0.869	1136	236	0.742	
892	14	44	0.039	42049	0.980	1136	236	0.781	
933	14	41	0.037	42049	0.913	1136	236	0.818	pxl -> m conv. Rate
973	14	40	0.036	42049	0.891	1136	236	0.854	0.000897026
1010	14	37	0.033	42049	0.824	1136	236	0.887	
1053	14	43	0.039	42049	0.958	1136	236	0.926	
1095	14	42	0.038	42049	0.935	1136	236	0.963	

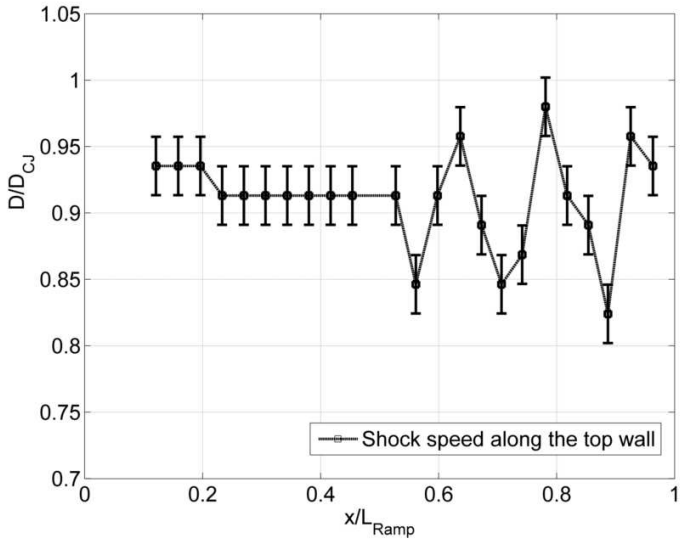

Figure A.3: Normalized detonation speed $\frac{D}{D_{CJ}}$ calculation and variation along the large ramp for acetylene mixture $2C_2H_2 + 5O_2 + 21Ar$ at 10.3 kPa.

X	Y	Delta_x	Delta_x(m)	FPS	V	Ramp End_X	Ramp End_y	Delta_x_Relative to ramp	D_CJ
170	10			42049		1190	255	0.085	1688.4
210	10	40	0.036	42049	0.894	1190	255	0.121	
251	10	41	0.037	42049	0.916	1190	255	0.158	V_ave
291	10	40	0.036	42049	0.894	1190	255	0.194	0.898461076
332	10	41	0.037	42049	0.916	1190	255	0.230	
372	10	40	0.036	42049	0.894	1190	255	0.266	x_ref
411	10	39	0.035	42049	0.871	1190	255	0.301	1145
453	10	42	0.038	42049	0.938	1190	255	0.339	607
492	10	39	0.035	42049	0.871	1190	255	0.374	Deltax_ref (pixels)
534	10	42	0.038	42049	0.938	1190	255	0.412	538
616	10	82	0.074	21025	0.916	1190	255	0.485	
652	10	36	0.032	42049	0.804	1190	255	0.517	y_ref
695	10	43	0.039	42049	0.961	1190	255	0.556	43
734	10	39	0.035	42049	0.871	1190	255	0.591	43
773	10	39	0.035	42049	0.871	1190	255	0.626	Deltax_ref (inches)
814	10	41	0.037	42049	0.916	1190	255	0.663	19
854	10	40	0.036	42049	0.894	1190	255	0.699	
887	10	33	0.030	42049	0.737	1190	255	0.728	
932	10	45	0.040	42049	1.005	1190	255	0.769	
973	12	41	0.037	42049	0.916	1190	255	0.805	pxl -> m conv. Rate
1007	12	34	0.030	42049	0.760	1190	255	0.836	0.000897026
1053	12	46	0.041	42049	1.028	1190	255	0.877	
1095	12	42	0.038	42049	0.938	1190	255	0.915	

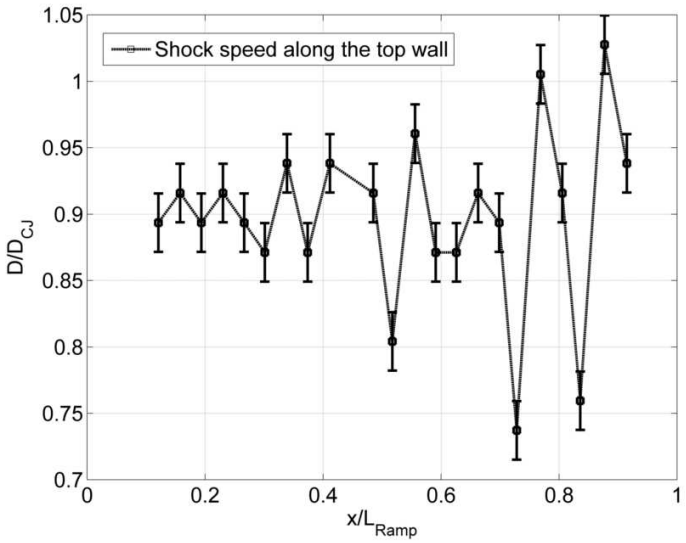

Figure A.4: Normalized detonation speed $\frac{D}{D_{CJ}}$ calculation and variation along the large ramp for acetylene mixture $2C_2H_2 + 5O_2 + 21Ar$ at 9.0 kPa.

X	Y	Delta_x	Delta_x(m)	FPS	V	Ramp End_X	Ramp End_y	Delta_x_Relative to ramp	D_CJ
148	12			42049		1190	255	0.065	1687.1
190	12	42	0.038	42049	0.939	1190	255	0.103	
231	12	41	0.037	42049	0.917	1190	255	0.140	V_ave
272	12	41	0.037	42049	0.917	1190	255	0.177	0.881251325
312	12	40	0.036	42049	0.894	1190	255	0.212	
352	12	40	0.036	42049	0.894	1190	255	0.248	x_ref
392	12	40	0.036	42049	0.894	1190	255	0.284	1145
432	12	40	0.036	42049	0.894	1190	255	0.320	607
471	12	39	0.035	42049	0.872	1190	255	0.355	Deltax_ref (pixels)
510	12	39	0.035	42049	0.872	1190	255	0.390	538
549	12	39	0.035	42049	0.872	1190	255	0.425	
629	12	80	0.072	21025	0.894	1190	255	0.497	y_ref
669	12	40	0.036	42049	0.894	1190	255	0.533	43
710	12	41	0.037	42049	0.917	1190	255	0.569	43
744	12	34	0.030	42049	0.760	1190	255	0.600	Deltax_ref (inches)
779	12	35	0.031	42049	0.783	1190	255	0.631	19
821	12	42	0.038	42049	0.939	1190	255	0.669	
862	12	41	0.037	42049	0.917	1190	255	0.706	
905	12	43	0.039	42049	0.961	1190	255	0.744	
944	12	39	0.035	42049	0.872	1190	255	0.779	pxl -> m conv. Rate
975	12	31	0.028	42049	0.693	1190	255	0.807	0.000897026
1008	12	33	0.030	42049	0.738	1190	255	0.837	
1053	12	45	0.040	42049	1.006	1190	255	0.877	
1094	12	41	0.037	42049	0.917	1190	255	0.914	

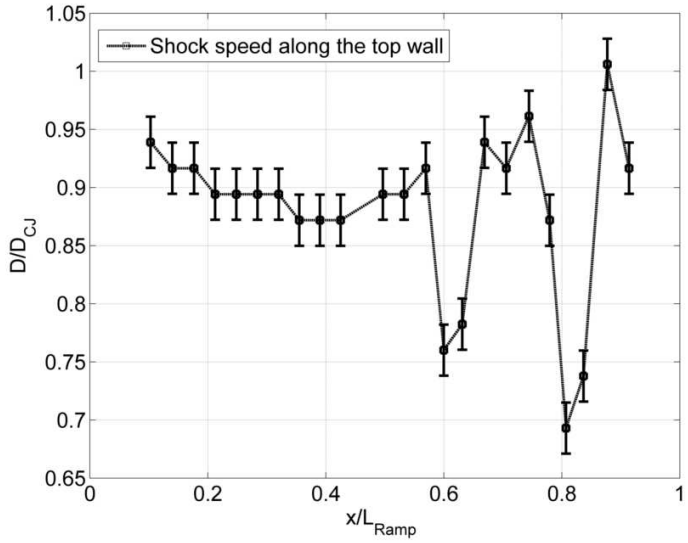

Figure A.5: Normalized detonation speed $\frac{D}{D_{CJ}}$ calculation and variation along the large ramp for acetylene mixture $2C_2H_2 + 5O_2 + 21Ar$ at 8.7 kPa.

X	Y	Delta_x	Delta_x(m)	FPS	V	Ramp End_X	Ramp End_y	Delta_x_Relative to ramp	D_CJ
89	18			42496		1131	229	0.065	1682.6
131	18	42	0.038	42496	0.952	1131	229	0.103	
170	18	39	0.035	42496	0.884	1131	229	0.138	V_ave
207	18	37	0.033	42496	0.838	1131	229	0.171	0.876590669
246	18	39	0.035	42496	0.884	1131	229	0.206	
283	18	37	0.033	42496	0.838	1131	229	0.239	x_ref
322	18	39	0.035	42496	0.884	1131	229	0.274	1130
361	18	39	0.035	42496	0.884	1131	229	0.309	592
400	18	39	0.035	42496	0.884	1131	229	0.344	Deltax_ref (pixels)
438	18	38	0.034	42496	0.861	1131	229	0.378	538
477	18	39	0.035	42496	0.884	1131	229	0.413	
515	18	38	0.034	42496	0.861	1131	229	0.447	y_ref
553	18	38	0.034	42496	0.861	1131	229	0.482	42
630	18	77	0.069	21248	0.872	1131	229	0.551	42
669	18	39	0.035	42496	0.884	1131	229	0.586	Deltax_ref (inches)
707	18	38	0.034	42496	0.861	1131	229	0.620	19
744	18	37	0.033	42496	0.838	1131	229	0.653	
784	18	40	0.036	42496	0.906	1131	229	0.689	
821	18	37	0.033	42496	0.838	1131	229	0.757	pxl -> m conv. Rate
860	18	39	0.035	42496	0.884	1131	229	0.798	0.000897026
906	18	46	0.041	42496	1.042	1131	229	0.830	
942	18	36	0.032	42496	0.816	1131	229	0.859	
974	18	32	0.029	42496	0.725	1131	229	0.897	
1016	18	42	0.038	42496	0.952	1131	229	0.933	
1095	18	39	0.035	42496	0.884	1131	229	0.968	

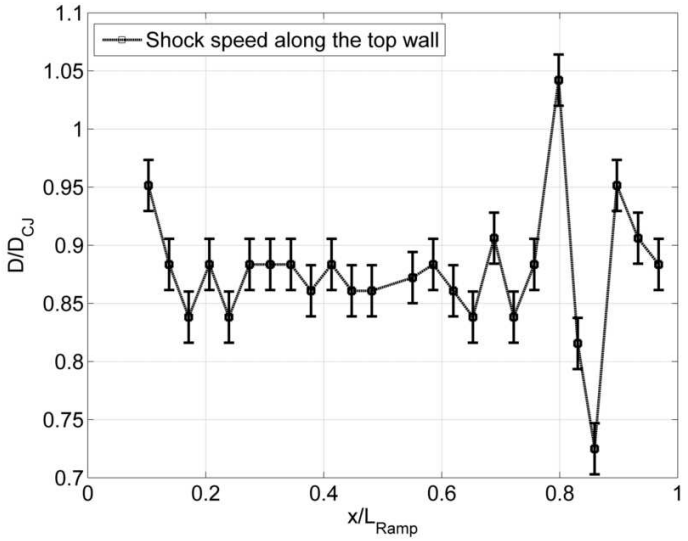

Figure A.6: Normalized detonation speed $\frac{D}{D_{CJ}}$ calculation and variation along the large ramp for acetylene mixture $2C_2H_2 + 5O_2 + 21Ar$ at 7.6 kPa.

X	Y	Delta_x	Delta_x(m)	FPS	V	Ramp End_X	Ramp End_y	Delta_x_Relative to ramp	D_CJ
111	18			42496		1131	229	0.085	1675.6
152	18	41	0.037	42496	0.933	1131	229	0.122	
190	18	38	0.034	42496	0.865	1131	229	0.156	V_ave
230	18	40	0.036	42496	0.910	1131	229	0.192	0.845965578
262	18	32	0.029	42496	0.728	1131	229	0.220	
301	18	39	0.035	42496	0.887	1131	229	0.255	x_ref
340	18	39	0.035	42496	0.887	1131	229	0.290	1130
369	18	29	0.026	42496	0.660	1131	229	0.316	592
399	18	30	0.027	42496	0.683	1131	229	0.343	Deltax_ref (pixels)
439	18	40	0.036	42496	0.910	1131	229	0.379	538
477	18	38	0.034	42496	0.865	1131	229	0.413	
515	18	38	0.034	42496	0.865	1131	229	0.447	y_ref
544	18	29	0.026	42496	0.660	1131	229	0.473	42
629	18	85	0.076	21248	0.967	1131	229	0.550	42
670	18	41	0.037	42496	0.933	1131	229	0.586	Deltax_ref (inches)
705	18	35	0.031	42496	0.796	1131	229	0.618	19
734	18	29	0.026	42496	0.660	1131	229	0.644	
763	18	29	0.026	42496	0.660	1131	229	0.670	
803	18	40	0.036	42496	0.910	1131	229	0.706	
842	18	39	0.035	42496	0.887	1131	229	0.741	
884	18	42	0.038	42496	0.956	1131	229	0.778	
923	18	39	0.035	42496	0.887	1131	229	0.813	
964	18	41	0.037	42496	0.933	1131	229	0.850	pxl -> m conv. Rate
995	18	31	0.028	42496	0.705	1131	229	0.878	0.000897026
1032	18	37	0.033	42496	0.842	1131	229	0.911	
1070	18	38	0.034	42496	0.865	1131	229	0.945	
1115	18	45	0.040	42496	1.024	1131	229	0.986	

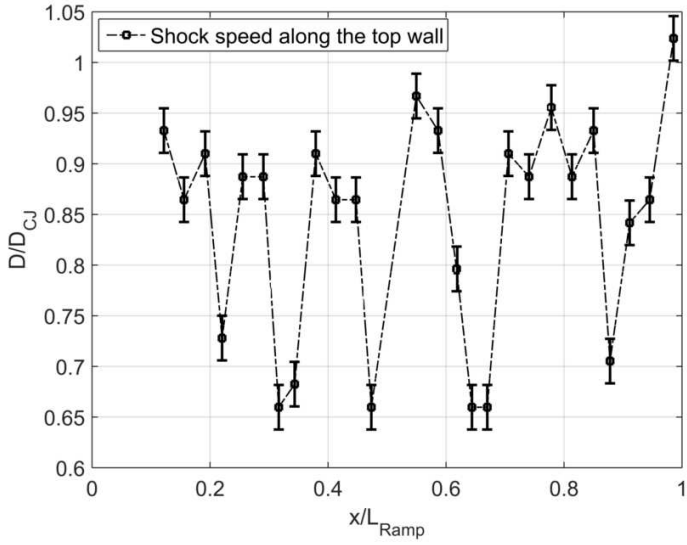

Figure A.7: Normalized detonation speed $\frac{D}{D_{CJ}}$ calculation and variation along the large ramp for acetylene mixture $2C_2H_2 + 5O_2 + 21Ar$ at 6.2 kPa.

X	Y	Delta_x	Delta_x(m)	FPS	V	Ramp End_X	Ramp End_y	Delta_x_Relative to ramp	D_CJ
95	19			42496		1131	229	0.071	1666.9
137	19	42	0.038	42496	0.960	1131	229	0.108	
167	19	30	0.027	42496	0.686	1131	229	0.135	V_ave
212	19	45	0.040	42496	1.029	1131	229	0.176	0.798042579
248	19	36	0.032	42496	0.823	1131	229	0.208	
279	19	31	0.028	42496	0.709	1131	229	0.236	x_ref
311	19	32	0.029	42496	0.732	1131	229	0.264	1130
347	19	36	0.032	42496	0.823	1131	229	0.297	592
384	19	37	0.033	42496	0.846	1131	229	0.330	Deltax_ref (pixels)
419	19	35	0.031	42496	0.800	1131	229	0.361	538
449	19	30	0.027	42496	0.686	1131	229	0.388	
488	19	39	0.035	42496	0.892	1131	229	0.423	y_ref
528	19	40	0.036	42496	0.915	1131	229	0.459	42
615	19	87	0.078	14165	0.663	1131	229	0.537	42
647	19	32	0.029	42496	0.732	1131	229	0.566	Deltax_ref (inches)
684	19	37	0.033	42496	0.846	1131	229	0.599	19
721	19	37	0.033	42496	0.846	1131	229	0.632	
762	19	41	0.037	42496	0.938	1131	229	0.669	
798	19	36	0.032	42496	0.823	1131	229	0.701	
827	19	29	0.026	42496	0.663	1131	229	0.727	
855	19	28	0.025	42496	0.640	1131	229	0.752	
879	19	24	0.022	42496	0.549	1131	229	0.774	
903	19	24	0.022	42496	0.549	1131	229	0.795	
945	19	42	0.038	42496	0.960	1131	229	0.833	pxl -> m conv. Rate
992	19	47	0.042	42496	1.075	1131	229	0.875	0.000897026
1029	19	37	0.033	42496	0.846	1131	229	0.909	
1072	19	43	0.039	42496	0.983	1131	229	0.947	
1107	19	35	0.031	42496	0.800	1131	229	0.978	

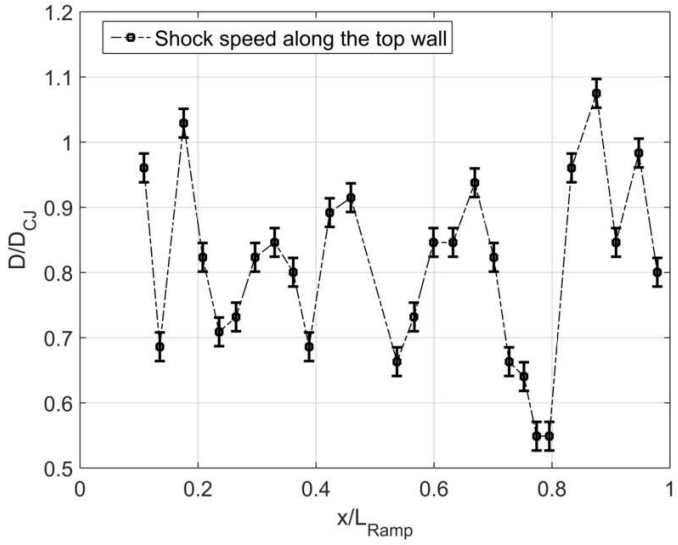

Figure A.8: Normalized detonation speed $\frac{D}{D_{CJ}}$ calculation and variation along the large ramp for acetylene mixture $2C_2H_2 + 5O_2 + 21Ar$ at 4.8 kPa.

X	Y	Delta_x	Delta_x(m)	FPS	V	Ramp End_X	Ramp End_y	Delta_x_Relative to ramp	D_CJ
142	16			42049		1118	231	0.106	2267.9
200	16	58	0.053	42049	0.985	1118	231	0.159	
259	16	59	0.054	42049	1.002	1118	231	0.213	V_ave
318	16	59	0.054	42049	1.002	1118	231	0.267	1.00599733
377	16	59	0.054	42049	1.002	1118	231	0.321	
437	16	60	0.055	42049	1.019	1118	231	0.376	x_ref
496	16	59	0.054	42049	1.002	1118	231	0.430	1118
615	16	119	0.109	21025	1.010	1118	231	0.539	591
674	16	59	0.054	42049	1.002	1118	231	0.593	Deltax_ref (pixels)
733	16	59	0.054	42049	1.002	1118	231	0.647	527
793	16	60	0.055	42049	1.019	1118	231	0.702	y_ref
852	16	59	0.054	42049	1.002	1118	231	0.756	52
912	16	60	0.055	42049	1.019	1118	231	0.811	52
971	16	59	0.054	42049	1.002	1118	231	0.865	Deltax_ref (inches)
1030	16	59	0.054	42049	1.002	1118	231	0.919	19
1090	16	60	0.055	42049	1.019	1118	231	0.974	0.00091575

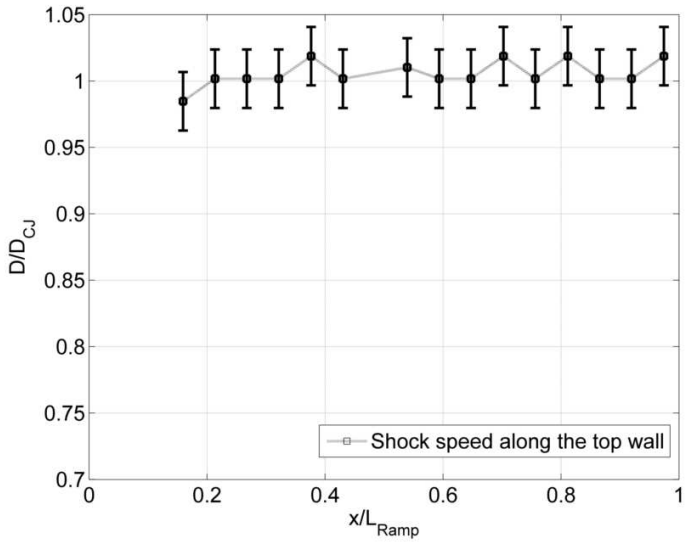

Figure A.9: Normalized detonation speed $\frac{D}{D_{CJ}}$ calculation and variation along the large ramp for propane mixture $C_3H_8 + 5O_2$ at 13.8 kPa.

X	Y	Delta_x	Delta_x(m)	FPS	V	Ramp End_X	Ramp End_y	Delta_x_Relative to ramp	D_CJ
150	16			42049		1118	231	0.114	2255.3
208	16	58	0.053	42049	0.990	1118	231	0.167	
266	16	58	0.053	42049	0.990	1118	231	0.220	V_ave
324	16	58	0.053	42049	0.990	1118	231	0.273	0.99454396
382	16	58	0.053	42049	0.990	1118	231	0.326	
440	16	58	0.053	42049	0.990	1118	231	0.379	x_ref
499	16	59	0.054	42049	1.007	1118	231	0.433	1118
615	16	116	0.106	21025	0.990	1118	231	0.539	591
672	16	57	0.052	42049	0.973	1118	231	0.592	Deltax_ref (pixels)
732	16	60	0.055	42049	1.024	1118	231	0.647	527
791	16	59	0.054	42049	1.007	1118	231	0.701	y_ref
849	16	58	0.053	42049	0.990	1118	231	0.754	52
908	16	59	0.054	42049	1.007	1118	231	0.808	52
966	16	58	0.053	42049	0.990	1118	231	0.861	Deltax_ref (inches)
1024	16	58	0.053	42049	0.990	1118	231	0.914	19
1082	16	58	0.053	42049	0.990	1118	231	0.967	0.00091575

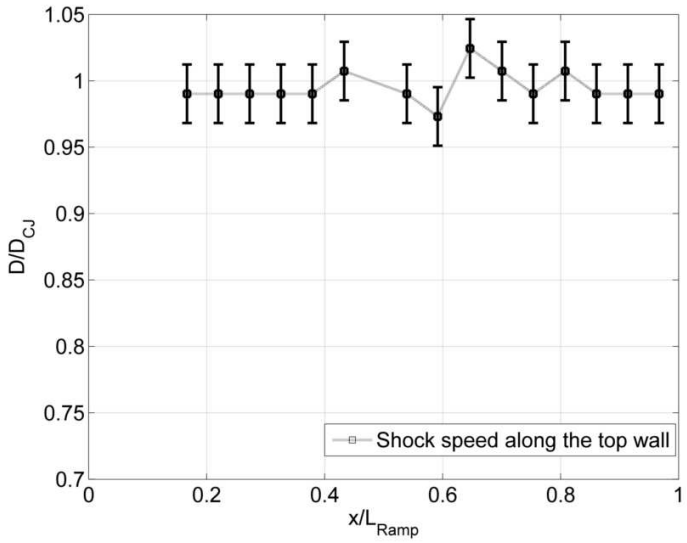

Figure A.10: Normalized detonation speed $\frac{D}{D_{CJ}}$ calculation and variation along the large ramp for propane mixture $C_3H_8 + 5O_2$ at 10.3 kPa.

X	Y	Delta_x	Delta_x(m)	FPS	V	Ramp End_X	Ramp End_y	Delta_x_Relative to ramp	D_CJ
173	16			42049		1118	231	0.135	2247.3
229	16	56	0.051	42049	0.960	1118	231	0.186	
286	16	57	0.052	42049	0.977	1118	231	0.238	V_ave
343	16	57	0.052	42049	0.977	1118	231	0.290	0.983091681
401	16	58	0.053	42049	0.994	1118	231	0.343	
459	16	58	0.053	42049	0.994	1118	231	0.397	x_ref
516	16	57	0.052	42049	0.977	1118	231	0.449	1118
631	16	115	0.105	21025	0.985	1118	231	0.554	591
689	16	58	0.053	42049	0.994	1118	231	0.607	Deltax_ref (pixels)
746	16	57	0.052	42049	0.977	1118	231	0.659	527
804	16	58	0.053	42049	0.994	1118	231	0.712	y_ref
861	16	57	0.052	42049	0.977	1118	231	0.765	52
919	16	58	0.053	42049	0.994	1118	231	0.818	52
976	16	57	0.052	42049	0.977	1118	231	0.870	Deltax_ref (inches)
1034	16	58	0.053	42049	0.994	1118	231	0.923	19
1091	16	57	0.052	42049	0.977	1118	231	0.975	0.00091575

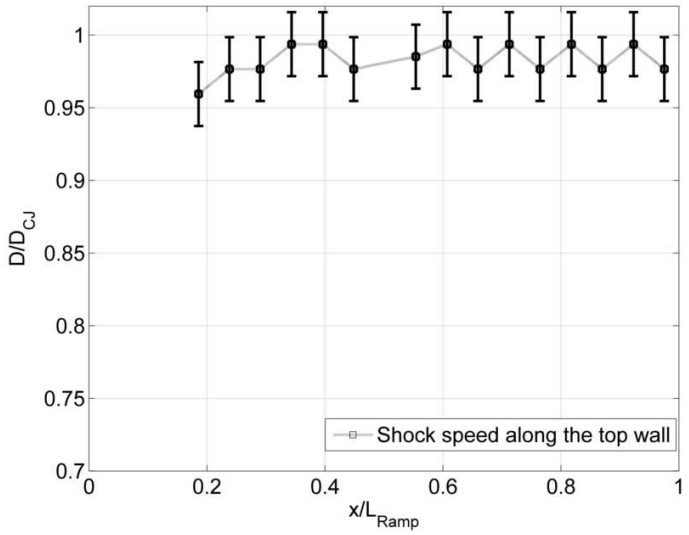

Figure A.11: Normalized detonation speed $\frac{D}{D_{CJ}}$ calculation and variation along the large ramp for propane mixture $C_3H_8 + 5O_2$ at 8.6 kPa.

X	Y	Delta_x	Delta_x(m)	FPS	V	Ramp End_X	Ramp End_y	Delta_x_Relative to ramp	D_CJ
220	14			42049		1118	231	0.178	2237.6
276	16	56	0.051	42049	0.964	1118	231	0.229	
334	16	58	0.053	42049	0.998	1118	231	0.282	V_ave
389	16	55	0.050	42049	0.946	1118	231	0.332	0.971722082
445	16	56	0.051	42049	0.964	1118	231	0.384	x_ref
503	16	58	0.053	42049	0.998	1118	231	0.437	1118
613	16	110	0.101	21025	0.946	1118	231	0.538	591
672	16	59	0.054	42049	1.015	1118	231	0.592	Deltax_ref (pixels)
727	16	55	0.050	42049	0.946	1118	231	0.642	527
784	16	57	0.052	42049	0.981	1118	231	0.694	y_ref
839	16	55	0.050	42049	0.946	1118	231	0.745	52
897	16	58	0.053	42049	0.998	1118	231	0.798	52
954	16	57	0.052	42049	0.981	1118	231	0.850	Deltax_ref (inches)
1011	16	57	0.052	42049	0.981	1118	231	0.902	19
1067	16	56	0.051	42049	0.964	1118	231	0.953	0.00091575

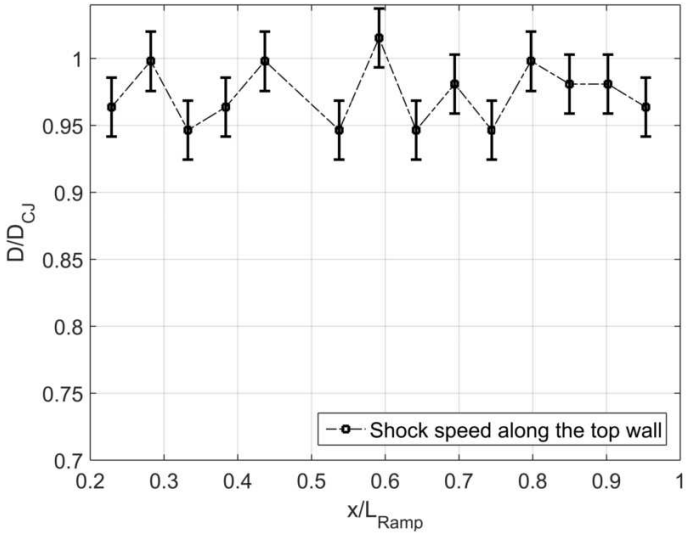

Figure A.12: Normalized detonation speed $\frac{D}{D_{CJ}}$ calculation and variation along the large ramp for propane mixture $C_3H_8 + 5O_2$ at 6.9 kPa.

X	Y	Delta_x	Delta_x(m)	FPS	V	Ramp End_X	Ramp End_y	Delta_x_Relative to ramp	D_CJ
172	16			42049		1118	231	0.134	2225.2
228	16	56	0.051	42049	0.969	1118	231	0.185	
279	16	51	0.047	42049	0.883	1118	231	0.232	V_ave
332	16	53	0.049	42049	0.917	1118	231	0.280	0.928344652
386	16	54	0.049	42049	0.934	1118	231	0.330	
437	16	51	0.047	42049	0.883	1118	231	0.376	x_ref
493	16	56	0.051	42049	0.969	1118	231	0.428	1118
547	16	54	0.049	42049	0.934	1118	231	0.477	591
653	16	106	0.097	21025	0.917	1118	231	0.574	Deltax_ref (pixels)
707	16	54	0.049	42049	0.934	1118	231	0.624	527
762	16	55	0.050	42049	0.952	1118	231	0.674	y_ref
819	16	57	0.052	42049	0.986	1118	231	0.726	52
871	16	52	0.048	42049	0.900	1118	231	0.774	52
917	16	46	0.042	42049	0.796	1118	231	0.816	Deltax_ref (inches)
972	16	55	0.050	42049	0.952	1118	231	0.866	19
1033	16	61	0.056	42049	1.056	1118	231	0.922	pxl -> m conv. Rate
1084	16	51	0.047	42049	0.883	1118	231	0.969	0.00091575

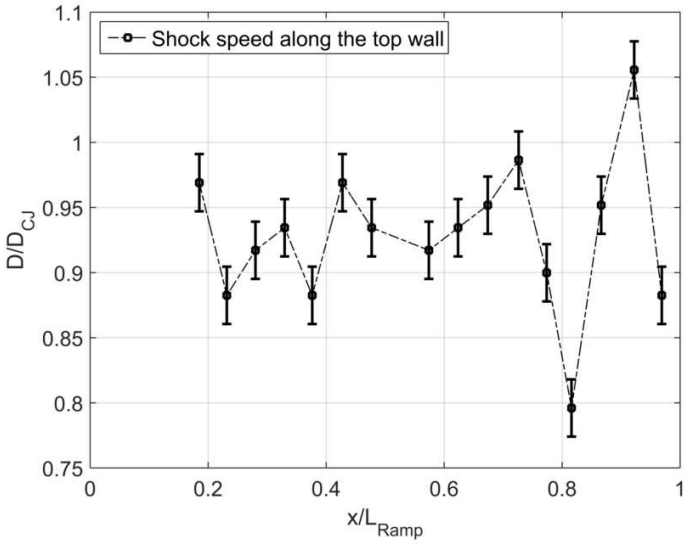

Figure A.13: Normalized detonation speed $\frac{D}{D_{CJ}}$ calculation and variation along the large ramp for propane mixture $C_3H_8 + 5O_2$ at 5.2 kPa.

X	Y	Delta_x	Delta_x(m)	FPS	V	Ramp End_X	Ramp End_y	Delta_x_Relative to ramp	D_CJ
118	16			42049		1118	231	0.084	2215.6
170	16	52	0.048	42049	0.904	1118	231	0.132	
220	16	50	0.046	42049	0.869	1118	231	0.178	V_ave
265	16	45	0.041	42049	0.782	1118	231	0.219	0.86532361
318	16	53	0.049	42049	0.921	1118	231	0.267	
372	16	54	0.049	42049	0.939	1118	231	0.317	x_ref
417	16	45	0.041	42049	0.782	1118	231	0.358	1118
476	16	59	0.054	42049	1.025	1118	231	0.412	591
523	16	47	0.043	42049	0.817	1118	231	0.455	Deltax_ref (pixels)
622	16	99	0.091	21025	0.860	1118	231	0.546	527
673	16	51	0.047	42049	0.886	1118	231	0.592	
735	16	62	0.057	42049	1.078	1118	231	0.649	y_ref
785	16	50	0.046	42049	0.869	1118	231	0.695	52
826	16	41	0.038	42049	0.713	1118	231	0.733	52
866	16	40	0.037	42049	0.695	1118	231	0.769	Deltax_ref (inches)
927	16	61	0.056	42049	1.060	1118	231	0.825	19
978	16	51	0.047	42049	0.886	1118	231	0.872	
1021	16	43	0.039	42049	0.747	1118	231	0.911	pxl -> m conv. Rate
1064	16	43	0.039	42049	0.747	1118	231	0.951	0.00091575

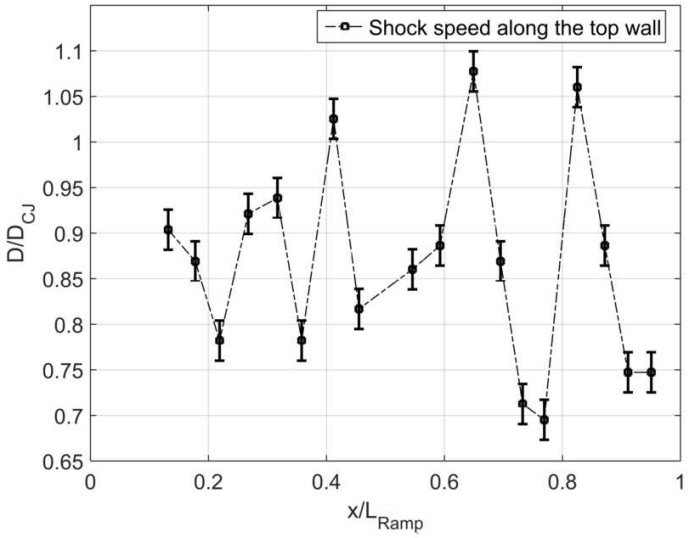

Figure A.14: Normalized detonation speed $\frac{D}{D_{CJ}}$ calculation and variation along the large ramp for propane mixture $C_3H_8 + 5O_2$ at 4.1 kPa.

X	Y	Delta_x	Delta_x(m)	FPS	V	Ramp End_X	Ramp End_y	Delta_x_Relative to ramp	D_CJ
196	16			42049		1118	231	0.156	2207.8
242	16	46	0.042	42049	0.802	1118	231	0.198	
295	16	53	0.049	42049	0.924	1118	231	0.246	V_ave
343	16	48	0.044	42049	0.837	1118	231	0.290	0.810549884
383	16	40	0.037	42049	0.698	1118	231	0.327	
441	16	58	0.053	42049	1.012	1118	231	0.380	x_ref
496	16	55	0.050	42049	0.959	1118	231	0.430	1118
547	16	51	0.047	42049	0.889	1118	231	0.477	591
645	16	98	0.090	21025	0.855	1118	231	0.567	Deltax_ref (pixels)
700	16	55	0.050	42049	0.959	1118	231	0.617	527
744	16	44	0.040	42049	0.767	1118	231	0.658	
792	16	48	0.044	42049	0.837	1118	231	0.701	y_ref
844	16	52	0.048	42049	0.907	1118	231	0.749	52
888	16	44	0.040	42049	0.767	1118	231	0.789	52
923	16	35	0.032	42049	0.610	1118	231	0.821	Deltax_ref (inches)
957	16	34	0.031	42049	0.593	1118	231	0.853	19
993	16	36	0.033	42049	0.628	1118	231	0.886	
1036	16	43	0.039	42049	0.750	1118	231	0.925	pxl -> m conv. Rate
1079	16	43	0.039	42049	0.750	1118	231	0.964	0.00091575

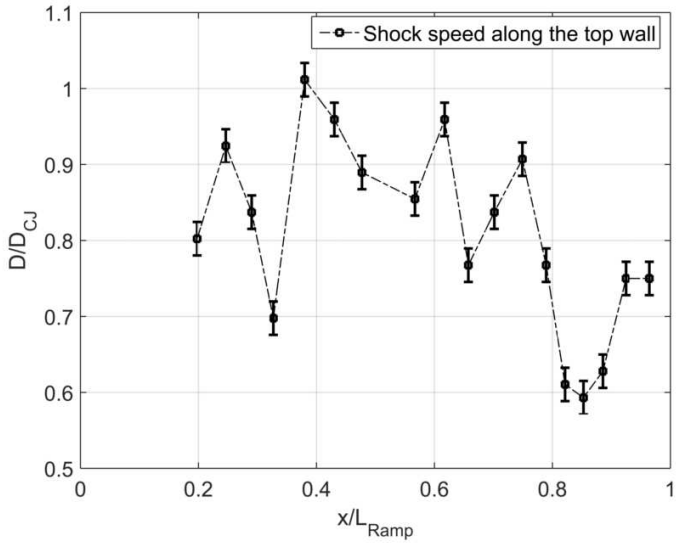

Figure A.15: Normalized detonation speed $\frac{D}{D_{CJ}}$ calculation and variation along the large ramp for propane mixture $C_3H_8 + 5O_2$ at 3.4 kPa.

X	Y	Delta_x	Delta_x(m)	FPS	V	Ramp End_X	Ramp End_y	Delta_x_Relative to ramp	D_CJ
198	16			42049		1118	231	0.158	2198.4
256	16	58	0.053	42049	1.016	1118	231	0.211	
299	16	43	0.039	42049	0.753	1118	231	0.250	
334	16	35	0.032	42049	0.613	1118	231	0.282	
390	16	56	0.051	42049	0.981	1118	231	0.333	
440	16	50	0.046	42049	0.876	1118	231	0.379	x_ref
480	16	40	0.037	42049	0.701	1118	231	0.416	1118
513	16	33	0.030	42049	0.578	1118	231	0.446	591
544	16	31	0.028	42049	0.543	1118	231	0.474	Deltax_ref (pixels)
627	16	83	0.076	14016	0.485	1118	231	0.550	527
665	16	38	0.035	42049	0.666	1118	231	0.585	
699	16	34	0.031	42049	0.596	1118	231	0.616	y_ref
733	16	34	0.031	42049	0.596	1118	231	0.647	52
765	16	32	0.029	42049	0.561	1118	231	0.677	52
796	16	31	0.028	42049	0.543	1118	231	0.705	Deltax_ref (inches)
825	16	29	0.027	42049	0.508	1118	231	0.732	19
854	16	29	0.027	42049	0.508	1118	231	0.758	
881	16	27	0.025	42049	0.473	1118	231	0.783	
909	16	28	0.026	42049	0.490	1118	231	0.809	
935	16	26	0.024	42049	0.455	1118	231	0.832	
960	16	25	0.023	42049	0.438	1118	231	0.855	pxl -> m conv. Rate
985	16	25	0.023	42049	0.438	1118	231	0.878	0.00091575
1008	16	23	0.021	42049	0.403	1118	231	0.899	
1032	16	24	0.022	42049	0.420	1118	231	0.921	
1055	16	23	0.021	42049	0.403	1118	231	0.942	
1078	16	23	0.021	42049	0.403	1118	231	0.963	
1101	16	23	0.021	42049	0.403	1118	231	0.984	

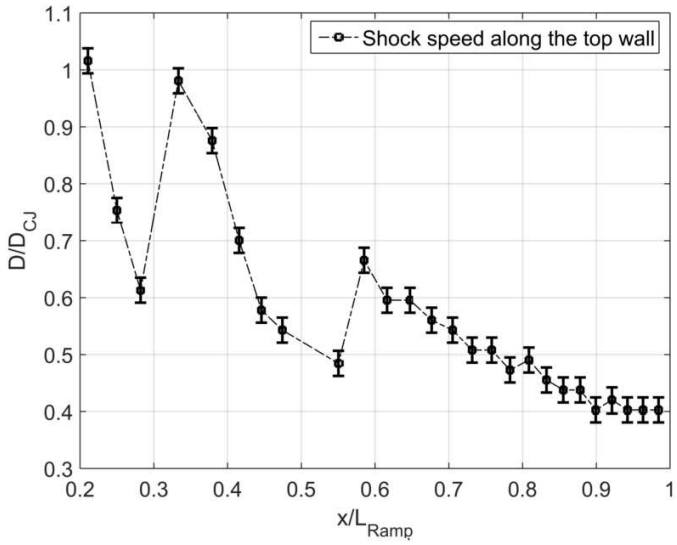

Figure A.16: Normalized detonation speed $\frac{D}{D_{CJ}}$ calculation and variation along the large ramp for propane mixture $C_3H_8 + 5O_2$ at 2.7 kPa.

X	Y	Delta_x	Delta_x(m)	FPS	V	Ramp Edge_X	Ramp Edge_y	Delta_x_Relative to ramp	D_CJ
83	17	44	0.039	42049	0.959	572	236	0.131	1715
127	17	43	0.038	42049	0.937	572	236	0.209	
170	17	44	0.039	42049	0.959	572	236	0.285	V_ave
214	17	43	0.038	42049	0.937	572	236	0.364	0.952176067
257	17	43	0.038	42049	0.937	572	236	0.440	
300	17	43	0.038	42049	0.937	572	236	0.517	x_ref
343	17	43	0.038	42049	0.937	572	236	0.593	1142
386	17	44	0.039	42049	0.959	572	236	0.669	599
430	17	43	0.038	42049	0.937	572	236	0.748	Deltax_ref (pixels)
473	17	44	0.039	42049	0.959	572	236	0.824	543
517	17	43	0.038	42049	0.937	572	236	0.902	
560	17	88	0.078	21024.5	0.959	572	236	0.979	y_ref
648	17	44	0.039	42049	0.959	572	236	1.135	132
692	17	44	0.039	42049	0.959	572	236	1.213	132
736	17	44	0.039	42049	0.959	572	236	1.292	Deltax_ref (inches)
780	17	44	0.039	42049	0.959	572	236	1.370	19
824	17	43	0.038	42049	0.937	572	236	1.448	
867	17	45	0.040	42049	0.981	572	236	1.524	
912	17	44	0.039	42049	0.959	572	236	1.604	pxl -> m conv. Rate
956	17	44	0.039	42049	0.959	572	236	1.683	0.000888766
1000	17	44	0.039	42049	0.959	572	236	1.761	
1044	17	44	0.039	42049	0.959	572	236	1.839	
1088	17			42049		572	236	1.917	

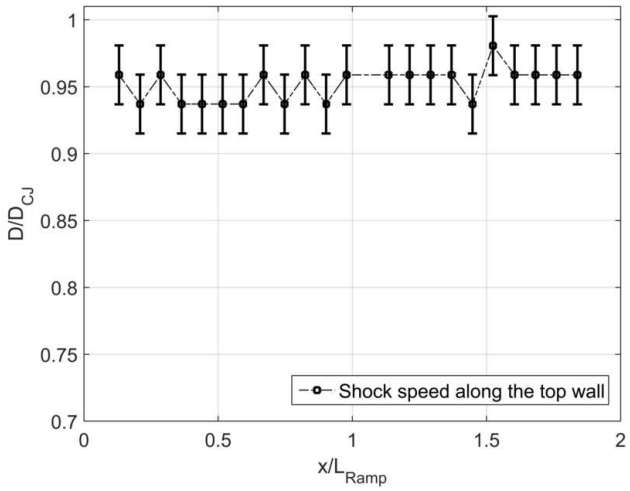

Figure A.17: Normalized detonation speed $\frac{D}{D_{CJ}}$ calculation and variation along the small ramp for acetylene mixture $2C_2H_2 + 5O_2 + 21Ar$ at 19.0 kPa.

X	Y	Delta_x	Delta_x(m)	FPS	V	Ramp End_X	Ramp End_y	Delta_x_Relative to ramp	
92	17			42049		574	238	0.143	D_CJ
135	17	43	0.038	42049	0.939	574	238	0.220	1711.6
178	17	43	0.038	42049	0.939	574	238	0.296	
221	17	43	0.038	42049	0.939	574	238	0.373	V_ave
264	17	43	0.038	42049	0.939	574	238	0.449	0.942675662
306	17	42	0.037	42049	0.917	574	238	0.524	
349	17	43	0.038	42049	0.939	574	238	0.600	x_ref
392	17	43	0.038	42049	0.939	574	238	0.676	1142
435	17	43	0.038	42049	0.939	574	238	0.753	599
478	17	43	0.038	42049	0.939	574	238	0.829	Deltax_ref (pixels)
521	17	43	0.038	42049	0.939	574	238	0.906	543
607	17	86	0.076	21025	0.939	574	238	1.059	
650	17	43	0.038	42049	0.939	574	238	1.135	y_ref
693	17	43	0.038	42049	0.939	574	238	1.212	100
737	17	44	0.039	42049	0.961	574	238	1.290	100
781	17	44	0.039	42049	0.961	574	238	1.368	Deltax_ref (inches)
824	17	43	0.038	42049	0.939	574	238	1.444	19
867	17	43	0.038	42049	0.939	574	238	1.521	
911	17	44	0.039	42049	0.961	574	238	1.599	pxl -> m conv. Rate
955	17	44	0.039	42049	0.961	574	238	1.677	0.000888766
998	17	43	0.038	42049	0.939	574	238	1.754	
1042	17	44	0.039	42049	0.961	574	238	1.832	
1085	17	43	0.038	42049	0.939	574	238	1.908	

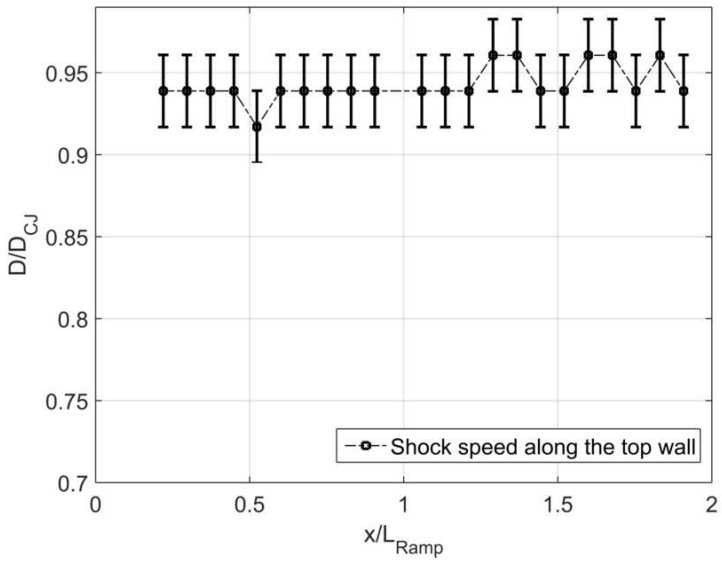

Figure A.18: Normalized detonation speed $\frac{D}{D_{CJ}}$ calculation and variation along the small ramp for acetylene mixture $2C_2H_2 + 5O_2 + 21Ar$ at 17.2 kPa.

X	Y	Delta_x	Delta_x(m)	FPS	V	Ramp End_X	Ramp End_y	Delta_x_Relative to ramp	D_CJ
136	17			42049		574	238	0.221	1707.9
179	17	43	0.038	42049	0.941	574	238	0.298	
220	17	41	0.036	42049	0.897	574	238	0.371	V_ave
263	17	43	0.038	42049	0.941	574	238	0.447	0.932955392
305	17	42	0.037	42049	0.919	574	238	0.522	
348	17	43	0.038	42049	0.941	574	238	0.598	x_ref
390	17	42	0.037	42049	0.919	574	238	0.673	1142
432	17	42	0.037	42049	0.919	574	238	0.748	599
474	17	42	0.037	42049	0.919	574	238	0.822	Deltax_ref (pixels)
517	17	43	0.038	42049	0.941	574	238	0.899	543
559	17	42	0.037	42049	0.919	574	238	0.973	
644	17	85	0.076	21025	0.930	574	238	1.124	y_ref
687	17	43	0.038	42049	0.941	574	238	1.201	129
730	17	43	0.038	42049	0.941	574	238	1.277	129
773	17	43	0.038	42049	0.941	574	238	1.354	Deltax_ref (inches)
816	17	43	0.038	42049	0.941	574	238	1.430	19
859	17	43	0.038	42049	0.941	574	238	1.507	
901	17	42	0.037	42049	0.919	574	238	1.581	pxl -> m conv. Rate
944	17	43	0.038	42049	0.941	574	238	1.658	0.000888766
988	17	44	0.039	42049	0.963	574	238	1.736	
1032	17	44	0.039	42049	0.963	574	238	1.814	
1074	17	42	0.037	42049	0.919	574	238	1.889	

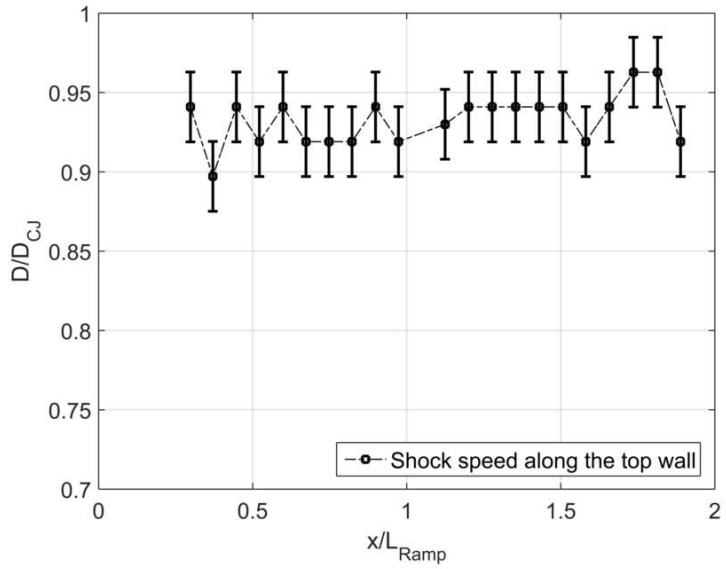

Figure A.19: Normalized detonation speed $\frac{D}{D_{CJ}}$ calculation and variation along the small ramp for acetylene mixture $2C_2H_2 + 5O_2 + 21Ar$ at 15.5 kPa.

X	Y	Delta_x	Delta_x(m)	FPS	V	Ramp End_X	Ramp End_y	Delta_x_Relative to ramp	D_CJ
153	17			42049		574	238	0.251658932	1703.7
195	17	42	0.037	42049	0.921	574	238	0.326315285	
237	17	42	0.037	42049	0.921	574	238	0.400971639	V_ave
279	17	42	0.037	42049	0.921	574	238	0.475627993	0.922293374
320	17	41	0.036	42049	0.899	574	238	0.548506814	
361	17	41	0.036	42049	0.899	574	238	0.621385635	x_ref
403	17	42	0.037	42049	0.921	574	238	0.696041989	1142
444	17	41	0.036	42049	0.899	574	238	0.76892081	599
486	17	42	0.037	42049	0.921	574	238	0.843577164	Deltax_ref (pixels)
528	17	42	0.037	42049	0.921	574	238	0.918233517	543
612	17	84	0.075	21025	0.921	574	238	1.067546225	
654	17	42	0.037	42049	0.921	574	238	1.142202578	y_ref
697	17	43	0.038	42049	0.943	574	238	1.218636464	63
740	17	43	0.038	42049	0.943	574	238	1.29507035	63
782	17	42	0.037	42049	0.921	574	238	1.369726703	Deltax_ref (inches)
824	17	42	0.037	42049	0.921	574	238	1.444383057	19
867	17	43	0.038	42049	0.943	574	238	1.520816943	
909	17	42	0.037	42049	0.921	574	238	1.595473297	
952	17	43	0.038	42049	0.943	574	238	1.671907182	pxl -> m conv. Rate
994	17	42	0.037	42049	0.921	574	238	1.746563536	0.000888766
1036	17	42	0.037	42049	0.921	574	238	1.82121989	
1078	17	42	0.037	42049	0.921	574	238	1.895876243	
1121	17	43	0.038	42049	0.943	574	238	1.972310129	

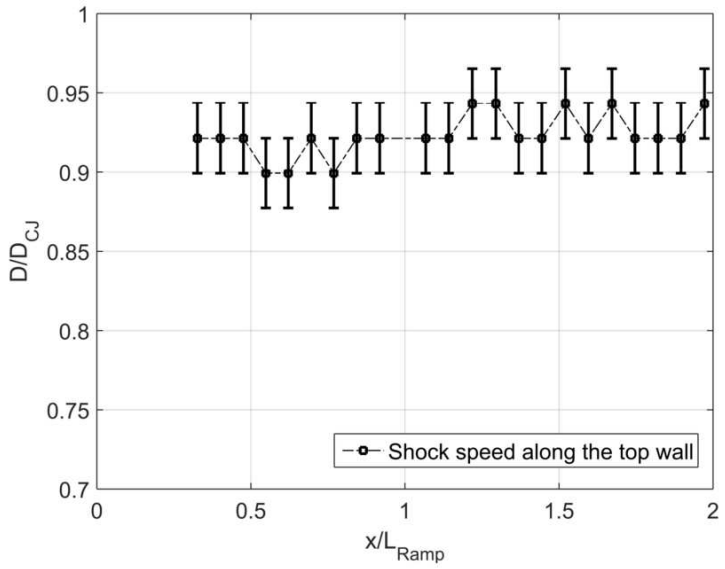

Figure A.20: Normalized detonation speed $\frac{D}{D_{CJ}}$ calculation and variation along the small ramp for acetylene mixture $2C_2H_2 + 5O_2 + 21Ar$ at 13.8 kPa.

X	Y	Delta_x	Delta_x(m)	FPS	V	Ramp End_X	Ramp End_y	Delta_x_Relative to ramp	D_CJ
178	17			42049		574	238	0.296	1698.9
220	17	42	0.037	42049	0.924	574	238	0.371	
261	17	41	0.036	42049	0.902	574	238	0.444	V_ave
302	17	41	0.036	42049	0.902	574	238	0.517	0.904901362
342	17	40	0.036	42049	0.880	574	238	0.588	
383	17	41	0.036	42049	0.902	574	238	0.660	x_ref
423	17	40	0.036	42049	0.880	574	238	0.732	1142
464	17	41	0.036	42049	0.902	574	238	0.804	599
505	17	41	0.036	42049	0.902	574	238	0.877	Deltax_ref (pixels)
546	17	41	0.036	42049	0.902	574	238	0.950	543
628	17	82	0.073	21025	0.902	574	238	1.096	
669	17	41	0.036	42049	0.902	574	238	1.169	y_ref
710	17	41	0.036	42049	0.902	574	238	1.242	63
752	17	42	0.037	42049	0.924	574	238	1.316	63
793	17	41	0.036	42049	0.902	574	238	1.389	Deltax_ref (inches)
834	17	41	0.036	42049	0.902	574	238	1.462	19
874	17	40	0.036	42049	0.880	574	238	1.533	
916	17	42	0.037	42049	0.924	574	238	1.608	pxl -> m conv. Rate
958	17	42	0.037	42049	0.924	574	238	1.683	0.000888766
999	17	41	0.036	42049	0.902	574	238	1.755	
1041	17	42	0.037	42049	0.924	574	238	1.830	
1083	17	42	0.037	42049	0.924	574	238	1.905	

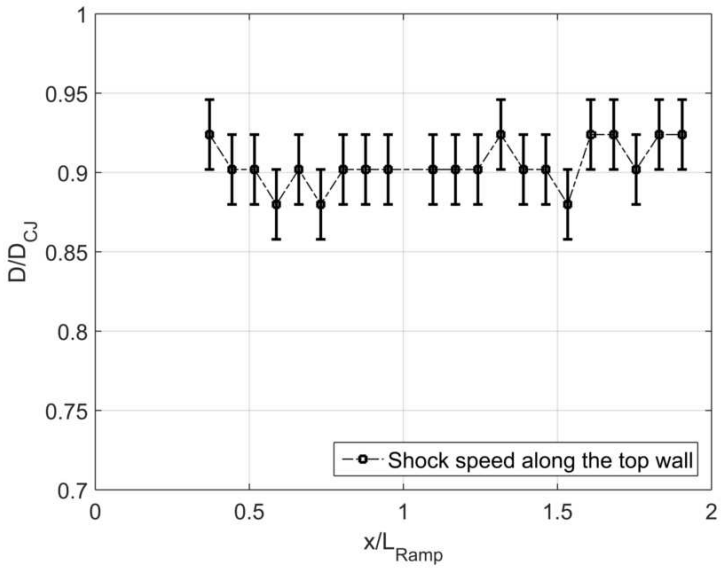

Figure A.21: Normalized detonation speed $\frac{D}{D_{CJ}}$ calculation and variation along the small ramp for acetylene mixture $2C_2H_2 + 5O_2 + 21Ar$ at 12.1 kPa.

X	Y	Delta_x	Delta_x(m)	FPS	V	Ramp End_X	Ramp End_y	Delta_x_Relative to ramp	D_CJ
57	31			46444		481	244	0.175	1688.4
90	31	33	0.032	46444	0.883	481	244	0.239	
123	31	33	0.032	46444	0.883	481	244	0.303	V_ave
156	31	33	0.032	46444	0.883	481	244	0.368	0.889177763
189	31	33	0.032	46444	0.883	481	244	0.432	
222	31	33	0.032	46444	0.883	481	244	0.496	x_ref
255	31	33	0.032	46444	0.883	481	244	0.560	1006
288	31	33	0.032	46444	0.883	481	244	0.624	510
320	33	32	0.031	46444	0.856	481	244	0.687	Deltax_ref (pixels)
353	34	33	0.032	46444	0.883	481	244	0.751	496
386	34	33	0.032	46444	0.883	481	244	0.815	
419	36	33	0.032	46444	0.883	481	244	0.879	y_ref
453	37	34	0.033	46444	0.910	481	244	0.946	104
551	41	98	0.095	15481	0.874	481	244	1.136	104
584	41	33	0.032	46444	0.883	481	244	1.200	Deltax_ref (inches)
617	41	33	0.032	46444	0.883	481	244	1.265	19
652	41	35	0.034	46444	0.937	481	244	1.333	
684	41	32	0.031	46444	0.856	481	244	1.395	
717	41	33	0.032	46444	0.883	481	244	1.459	
751	41	34	0.033	46444	0.910	481	244	1.525	
784	41	33	0.032	46444	0.883	481	244	1.590	pxl -> m conv. Rate
818	44	34	0.033	46444	0.910	481	244	1.656	0.000972984
852	44	34	0.033	46444	0.910	481	244	1.722	
886	44	34	0.033	46444	0.910	481	244	1.788	
920	44	34	0.033	46444	0.910	481	244	1.854	
954	44	34	0.033	46444	0.910	481	244	1.920	

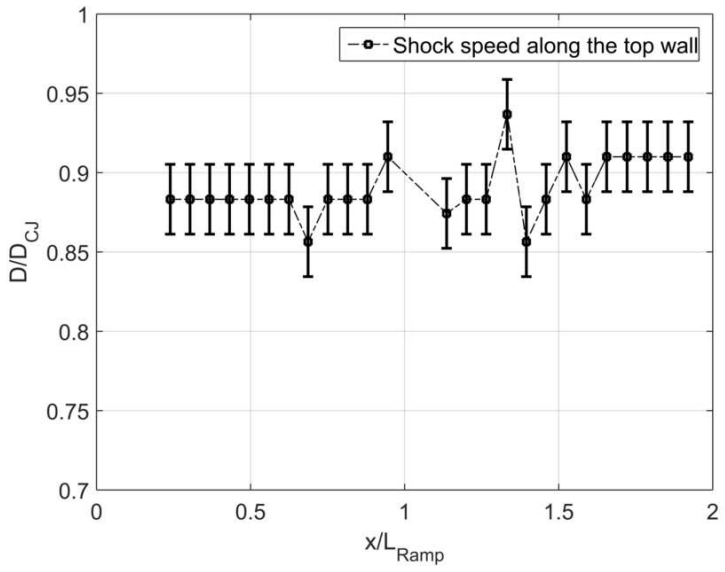

Figure A.22: Normalized detonation speed $\frac{D}{D_{CJ}}$ calculation and variation along the small ramp for acetylene mixture $2C_2H_2 + 5O_2 + 21Ar$ at 9.0 kPa.

X	Y	Delta_x	Delta_x(m)	FPS	V	Ramp End_X	Ramp End_y	Delta_x_Relative to ramp	D_CJ
24	32			46444		481	244	0.111	1685.6
57	32	33	0.032	46444	0.885	481	244	0.175	
90	32	33	0.032	46444	0.885	481	244	0.239	V_ave
122	32	32	0.031	46444	0.858	481	244	0.301	0.891399497
156	32	34	0.033	46444	0.912	481	244	0.368	
190	32	34	0.033	46444	0.912	481	244	0.434	x_ref
223	32	33	0.032	46444	0.885	481	244	0.498	1006
256	32	33	0.032	46444	0.885	481	244	0.562	510
289	32	33	0.032	46444	0.885	481	244	0.626	Deltax_ref (pixels)
321	32	32	0.031	46444	0.858	481	244	0.689	496
355	34	34	0.033	46444	0.912	481	244	0.755	
388	34	33	0.032	46444	0.885	481	244	0.819	y_ref
421	34	33	0.032	46444	0.885	481	244	0.883	103
455	35	34	0.033	46444	0.912	481	244	0.949	103
551	39	96	0.093	15481	0.858	481	244	1.136	Deltax_ref (inches)
584	39	33	0.032	46444	0.885	481	244	1.200	19
617	39	33	0.032	46444	0.885	481	244	1.265	
651	39	34	0.033	46444	0.912	481	244	1.331	
685	39	34	0.033	46444	0.912	481	244	1.397	
718	39	33	0.032	46444	0.885	481	244	1.461	pxl -> m conv. Rate
752	39	34	0.033	46444	0.912	481	244	1.527	0.000972984
785	39	33	0.032	46444	0.885	481	244	1.592	
819	41	34	0.033	46444	0.912	481	244	1.658	
853	43	34	0.033	46444	0.912	481	244	1.724	
887	44	34	0.033	46444	0.912	481	244	1.790	
921	44	34	0.033	46444	0.912	481	244	1.856	
955	44	34	0.033	46444	0.912	481	244	1.922	

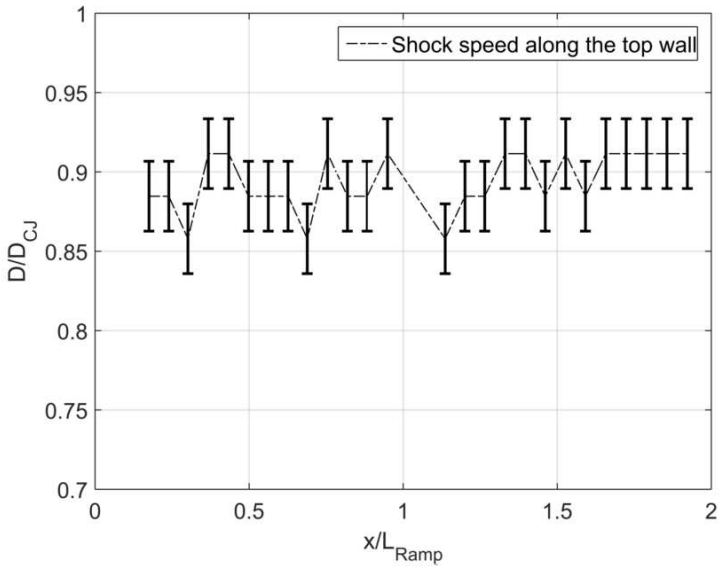

Figure A.23: Normalized detonation speed $\frac{D}{D_{CJ}}$ calculation and variation along the small ramp for acetylene mixture $2C_2H_2 + 5O_2 + 21Ar$ at 8.3 kPa.

X	Y	Delta_x	Delta_x(m)	FPS	V	Ramp End_X	Ramp End_y	Delta_x_Relative to ramp	D_CJ
79	15			42496		767	227	-0.297	1682.6
120	15	41	0.039	42496	0.976	767	227	-0.220	
159	15	39	0.037	42496	0.928	767	227	-0.146	V_ave
199	15	40	0.038	42496	0.952	767	227	-0.071	0.864586846
236	15	37	0.035	42496	0.881	767	227	-0.001	
274	15	38	0.036	42496	0.905	767	227	0.071	x_ref
311	15	37	0.035	42496	0.881	767	227	0.140	1102
346	15	35	0.033	42496	0.833	767	227	0.206	590
385	15	39	0.037	42496	0.928	767	227	0.280	Deltax_ref (pixels)
420	15	35	0.033	42496	0.833	767	227	0.346	512
450	15	30	0.028	42496	0.714	767	227	0.402	
488	15	38	0.036	42496	0.905	767	227	0.474	y_ref
527	15	39	0.037	42496	0.928	767	227	0.548	63
603	15	76	0.072	21248	0.905	767	227	0.691	63
632	15	29	0.027	42496	0.690	767	227	0.746	Deltax_ref (inches)
660	15	28	0.026	42496	0.667	767	227	0.798	19
687	15	27	0.025	42496	0.643	767	227	0.849	
731	15	44	0.041	42496	1.047	767	227	0.932	
767	15	36	0.034	42496	0.857	767	227	1.000	
812	15	45	0.042	42496	1.071	767	227	1.085	
851	15	39	0.037	42496	0.928	767	227	1.158	
887	15	36	0.034	42496	0.857	767	227	1.226	pxl -> m conv. Rate
926	15	39	0.037	42496	0.928	767	227	1.300	0.000942578
962	15	36	0.034	42496	0.857	767	227	1.368	
995	15	33	0.031	42496	0.786	767	227	1.430	
1036	15	41	0.039	42496	0.976	767	227	1.507	
1073	15	37	0.035	42496	0.881	767	227	1.577	

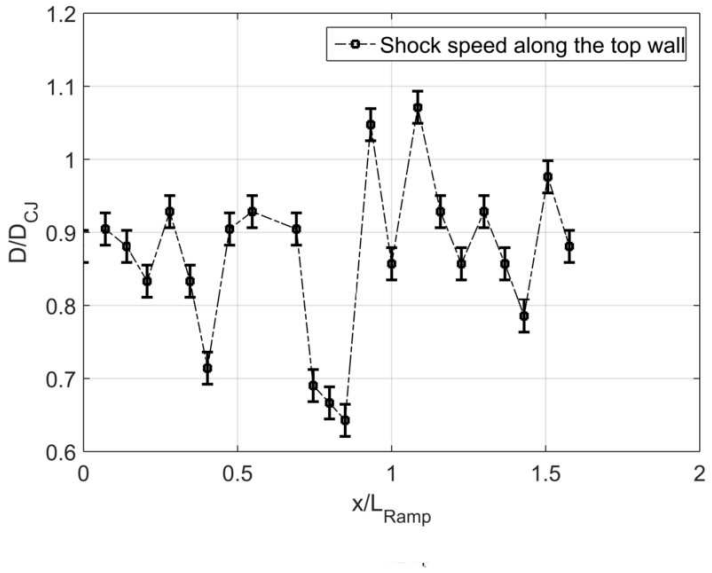

Figure A.24: Normalized detonation speed $\frac{D}{D_{CJ}}$ calculation and variation along the small ramp for acetylene mixture $2C_2H_2 + 5O_2 + 21Ar$ at 7.6 kPa.

X	Y	Delta_x	Delta_x(m)	FPS	V	Ramp End_X	Ramp End_y	Delta_x_Relative to ramp	D_CJ
65	15			42496		767	227	-0.323	1679.2
104	15	39	0.037	42496	0.930	767	227	-0.250	
144	15	40	0.038	42496	0.954	767	227	-0.174	V_ave
184	15	40	0.038	42496	0.954	767	227	-0.099	0.845736173
224	15	40	0.038	42496	0.954	767	227	-0.024	
296	15	72	0.068	21248	0.859	767	227	0.112	x_ref
333	15	37	0.035	42496	0.883	767	227	0.182	1102
369	15	36	0.034	42496	0.859	767	227	0.250	590
402	15	33	0.031	42496	0.787	767	227	0.312	Deltax_ref (pixels)
441	15	39	0.037	42496	0.930	767	227	0.385	512
473	15	32	0.030	42496	0.763	767	227	0.446	
505	15	32	0.030	42496	0.763	767	227	0.506	y_ref
539	15	34	0.032	42496	0.811	767	227	0.570	63
615	15	76	0.072	21248	0.906	767	227	0.713	63
654	15	39	0.037	42496	0.930	767	227	0.787	Deltax_ref (inches)
687	15	33	0.031	42496	0.787	767	227	0.849	19
718	15	31	0.029	42496	0.739	767	227	0.908	
749	15	31	0.029	42496	0.739	767	227	0.966	
787	15	38	0.036	42496	0.906	767	227	1.038	
817	15	30	0.028	42496	0.716	767	227	1.094	
848	15	31	0.029	42496	0.739	767	227	1.153	pxl -> m conv. Rate
892	15	44	0.041	42496	1.050	767	227	1.236	0.000942578
930	15	38	0.036	42496	0.906	767	227	1.307	
968	15	38	0.036	42496	0.906	767	227	1.379	
1003	15	35	0.033	42496	0.835	767	227	1.445	
1041	15	38	0.036	42496	0.906	767	227	1.517	
1076	15	35	0.033	42496	0.835	767	227	1.583	

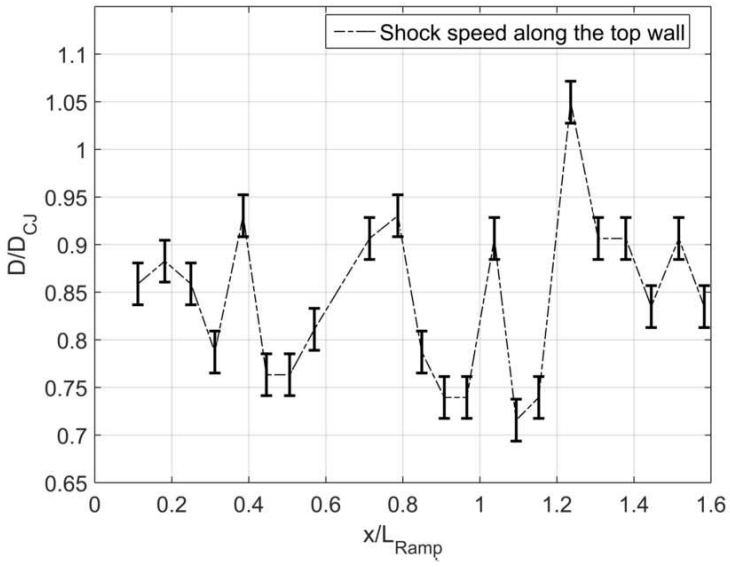

Figure A.25: Normalized detonation speed $\frac{D}{D_{CJ}}$ calculation and variation along the small ramp for acetylene mixture $2C_2H_2 + 5O_2 + 21Ar$ at 6.9 kPa.

X	Y	Delta_x	Delta_x(m)	FPS	V	Ramp End_X	Ramp End_y	Delta_x_Relative to ramp	D_CJ
91	19			42049		771	232	-0.305	1675.6
132	19	41	0.039	42049	0.987	771	232	-0.226	
173	19	41	0.039	42049	0.987	771	232	-0.147	V_ave
212	19	39	0.037	42049	0.939	771	232	-0.073	0.782506608
314	19	102	0.098	14016	0.819	771	232	0.123	
354	19	40	0.038	42049	0.963	771	232	0.200	x_ref
383	19	29	0.028	42049	0.698	771	232	0.255	1100
414	19	31	0.030	42049	0.746	771	232	0.315	597
450	19	36	0.035	42049	0.867	771	232	0.384	Deltax_ref (pixels)
476	19	26	0.025	42049	0.626	771	232	0.434	503
521	19	45	0.043	42049	1.083	771	232	0.520	
546	19	25	0.024	42049	0.602	771	232	0.568	y_ref
650	19	104	0.100	14016	0.835	771	232	0.768	63
685	19	35	0.034	42049	0.843	771	232	0.835	63
713	19	28	0.027	42049	0.674	771	232	0.889	Deltax_ref (inches)
747	19	34	0.033	42049	0.819	771	232	0.954	19
788	19	41	0.039	42049	0.987	771	232	1.033	
821	19	33	0.032	42049	0.795	771	232	1.096	
851	19	30	0.029	42049	0.722	771	232	1.154	
890	19	39	0.037	42049	0.939	771	232	1.228	pxl -> m conv. Rate
928	19	38	0.036	42049	0.915	771	232	1.301	0.000959443
958	19	30	0.029	42049	0.722	771	232	1.359	
987	19	29	0.028	42049	0.698	771	232	1.414	
1010	19	23	0.022	42049	0.554	771	232	1.459	
1029	19	19	0.018	42049	0.457	771	232	1.495	

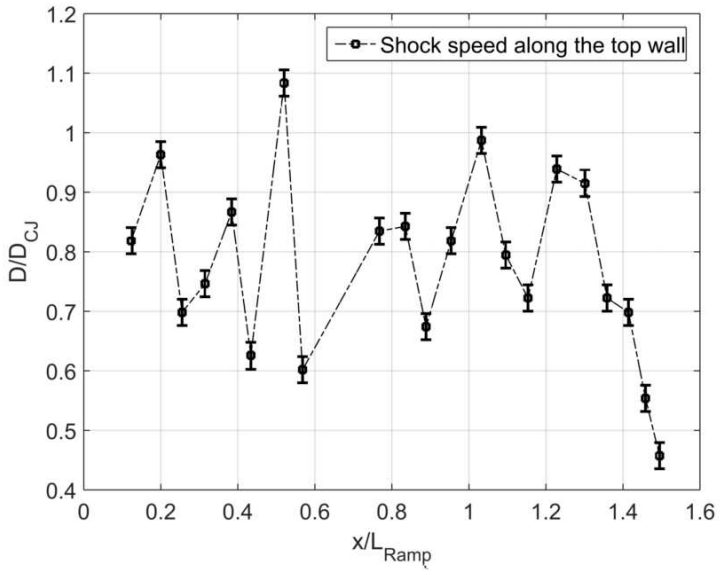

Figure A.26: Normalized detonation speed $\frac{D}{D_{CJ}}$ calculation and variation along the small ramp for acetylene mixture $2C_2H_2 + 5O_2 + 21Ar$ at 6.2 kPa.

X	Y	Delta_x	Delta_x(m)	FPS	V	Ramp End_X	Ramp End_y	Delta_x_Relative to ramp	D_CJ
90	19			42496		777	232	-0.321	1674.4
129	19	39	0.037	42496	0.952	777	232	-0.246	
168	19	39	0.037	42496	0.952	777	232	-0.171	V_ave
206	19	38	0.037	42496	0.927	777	232	-0.098	0.764133042
346	19	140	0.135	10624	0.854	777	232	0.171	
377	19	31	0.030	42496	0.756	777	232	0.231	x_ref
414	19	37	0.036	42496	0.903	777	232	0.302	1105
446	19	32	0.031	42496	0.781	777	232	0.364	603
472	19	26	0.025	42496	0.634	777	232	0.414	Deltax_ref (pixels)
502	19	30	0.029	42496	0.732	777	232	0.471	502
543	19	41	0.039	42496	1.000	777	232	0.550	
647	19	104	0.100	14165	0.846	777	232	0.750	y_ref
688	19	41	0.039	21248	0.500	777	232	0.829	55
707	19	19	0.018	42496	0.464	777	232	0.865	55
730	19	23	0.022	42496	0.561	777	232	0.910	Deltax_ref (inches)
755	19	25	0.024	42496	0.610	777	232	0.958	19
783	19	28	0.027	42496	0.683	777	232	1.012	
822	19	39	0.037	42496	0.952	777	232	1.087	
863	19	41	0.039	42496	1.000	777	232	1.165	
896	19	33	0.032	42496	0.805	777	232	1.229	pxl -> m conv. Rate
926	19	30	0.029	42496	0.732	777	232	1.286	0.000961355
954	19	28	0.027	42496	0.683	777	232	1.340	
978	19	24	0.023	42496	0.586	777	232	1.386	
1004	19	26	0.025	42496	0.634	777	232	1.436	
1035	19	31	0.030	42496	0.756	777	232	1.496	

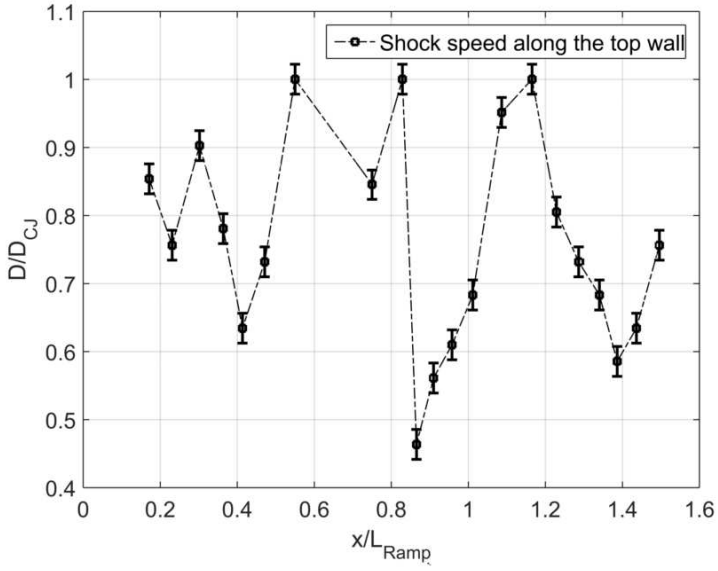

Figure A.27: Normalized detonation speed $\frac{D}{D_{CJ}}$ calculation and variation along the small ramp for acetylene mixture $2C_2H_2 + 5O_2 + 21Ar$ at 6.0 kPa.

X	Y	Delta_x	Delta_x(m)	FPS	V	Ramp End_X	Ramp End_y	Delta_x_Relative to ramp	D_CJ
39	12			42049		766	238	-0.299	2262
101	12	62	0.055	42049	1.030	766	238	-0.189	
162	12	61	0.055	42049	1.013	766	238	-0.080	V_ave
281	12	119	0.106	21025	0.988	766	238	0.133	0.995521708
341	12	60	0.054	42049	0.997	766	238	0.240	
400	12	59	0.053	42049	0.980	766	238	0.346	x_ref
460	12	60	0.054	42049	0.997	766	238	0.453	1120
520	12	60	0.054	42049	0.997	766	238	0.560	580
639	12	119	0.106	21025	0.988	766	238	0.773	Deltax_ref (pixels)
699	12	60	0.054	42049	0.997	766	238	0.880	540
760	12	61	0.055	42049	1.013	766	238	0.989	y_ref
820	12	60	0.054	42049	0.997	766	238	1.097	52
880	12	60	0.054	42049	0.997	766	238	1.204	52
940	12	60	0.054	42049	0.997	766	238	1.311	Deltax_ref (inches)
1000	12	60	0.054	42049	0.997	766	238	1.418	19
1060	12	60	0.054	42049	0.997	766	238	1.525	0.000893704

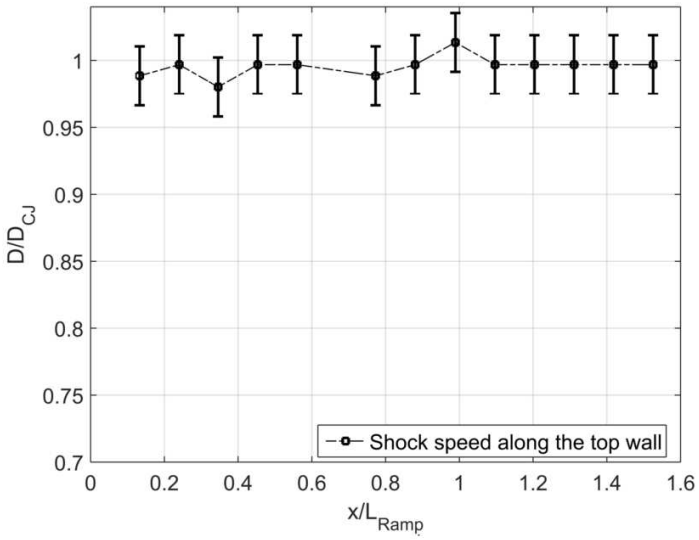

Figure A.28: Normalized detonation speed $\frac{D}{D_{CJ}}$ calculation and variation along the small ramp for propane mixture $C_3H_8 + 5O_2$ at 12.1 kPa.

X	Y	Delta_x	Delta_x(m)	FPS	V	Ramp End_X	Ramp End_y	Delta_x_Relative to ramp	D_CJ
77	11			42049		766	238	-0.232	2255.3
138	11	61	0.055	42049	1.016	766	238	-0.122	
198	11	60	0.054	42049	1.000	766	238	-0.015	V_ave
316	11	118	0.105	21025	0.983	766	238	0.196	0.986943481
375	11	59	0.053	42049	0.983	766	238	0.301	x_ref
434	11	59	0.053	42049	0.983	766	238	0.407	1120
493	11	59	0.053	42049	0.983	766	238	0.512	580
611	11	118	0.105	21025	0.983	766	238	0.723	Deltax_ref (pixels)
670	11	59	0.053	42049	0.983	766	238	0.828	540
729	11	59	0.053	42049	0.983	766	238	0.934	y_ref
789	11	60	0.054	42049	1.000	766	238	1.041	52
848	11	59	0.053	42049	0.983	766	238	1.147	52
907	11	59	0.053	42049	0.983	766	238	1.252	Deltax_ref (inches)
966	11	59	0.053	42049	0.983	766	238	1.357	19
1026	11	60	0.054	42049	1.000	766	238	1.465	pxl -> m conv. Rate
1086	11	60	0.054	42049	1.000	766	238	1.572	0.000893704

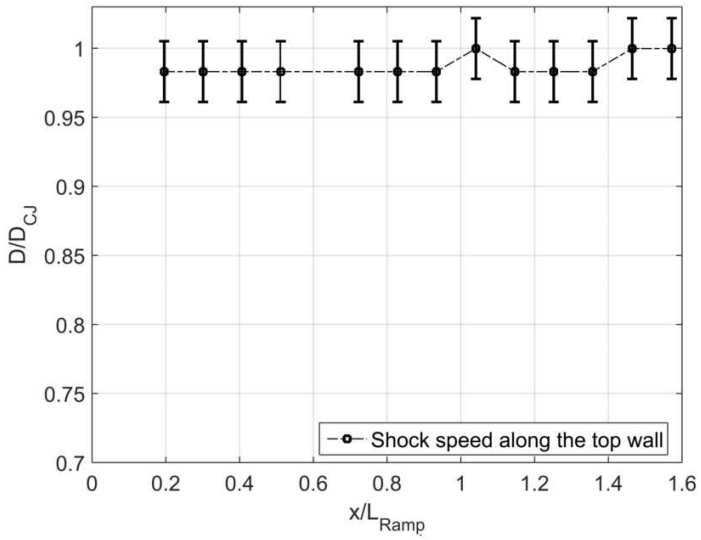

Figure A.29: Normalized detonation speed $\frac{D}{D_{CJ}}$ calculation and variation along the small ramp for propane mixture $C_3H_8 + 5O_2$ at 10.3 kPa.

X	Y	Delta_x	Delta_x(m)	FPS	V	Ramp End_X	Ramp End_y	Delta_x_Relative to ramp	D_CJ
36				42049		766	238	-0.305	2247.3
96		60	0.054	42049	1.003	766	238	-0.198	
157		61	0.055	42049	1.020	766	238	-0.089	V_ave
273	10	116	0.104	21025	0.970	766	238	0.119	0.96868148
332	10	59	0.053	42049	0.987	766	238	0.224	
389	10	57	0.051	42049	0.953	766	238	0.326	x_ref
446	10	57	0.051	42049	0.953	766	238	0.428	1120
505	10	59	0.053	42049	0.987	766	238	0.533	580
620	10	115	0.103	21025	0.962	766	238	0.739	Deltax_ref (pixels)
678	10	58	0.052	42049	0.970	766	238	0.843	540
735	10	57	0.051	42049	0.953	766	238	0.945	y_ref
793	10	58	0.052	42049	0.970	766	238	1.048	52
851	10	58	0.052	42049	0.970	766	238	1.152	52
910	10	59	0.053	42049	0.987	766	238	1.257	Deltax_ref (inches)
968	10	58	0.052	42049	0.970	766	238	1.361	19
1025	10	57	0.051	42049	0.953	766	238	1.463	pxl -> m conv. Rate
1084	10	59	0.053	42049	0.987	766	238	1.568	0.000893704

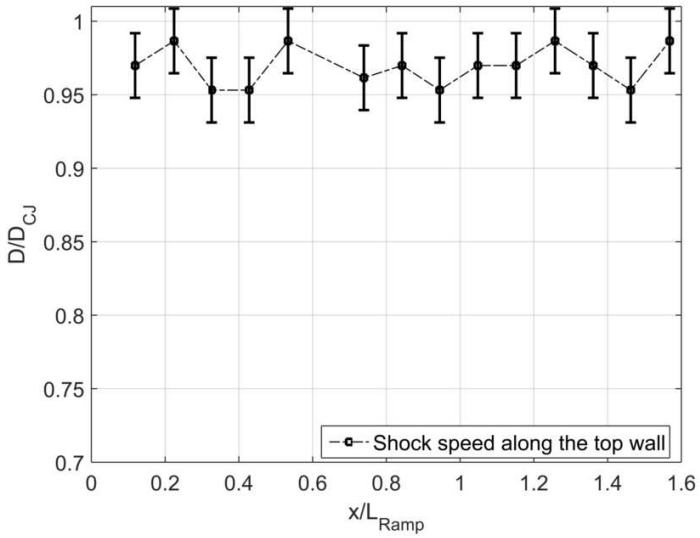

Figure A.30: Normalized detonation speed $\frac{D}{D_{CJ}}$ calculation and variation along the small ramp for propane mixture $C_3H_8 + 5O_2$ at 8.6 kPa.

X	Y	Delta_x	Delta_x(m)	FPS	V	Ramp End_X	Ramp End_y	Delta_x_Relative to ramp	D_CJ
31	10			42049		766	238	-0.314	2233.1
93	10	62	0.055	42049	1.043	766	238	-0.203	
152	10	59	0.053	42049	0.993	766	238	-0.097	V_ave
266	10	114	0.102	21025	0.959	766	238	0.106	0.912335971
320	10	54	0.048	42049	0.909	766	238	0.203	
374	10	54	0.048	42049	0.909	766	238	0.299	x_ref
428	10	54	0.048	42049	0.909	766	238	0.396	1120
482	10	54	0.048	42049	0.909	766	238	0.492	580
537	10	55	0.049	42049	0.926	766	238	0.591	Deltax_ref (pixels)
641	10	104	0.093	21025	0.875	766	238	0.777	540
693	10	52	0.046	42049	0.875	766	238	0.870	
752	12	59	0.053	42049	0.993	766	238	0.975	y_ref
811	12	59	0.053	42049	0.993	766	238	1.080	52
862	12	51	0.046	42049	0.858	766	238	1.172	52
919	12	57	0.051	42049	0.959	766	238	1.273	Deltax_ref (inches)
973	12	54	0.048	42049	0.909	766	238	1.370	19
1025	12	52	0.046	42049	0.875	766	238	1.463	0.000893704

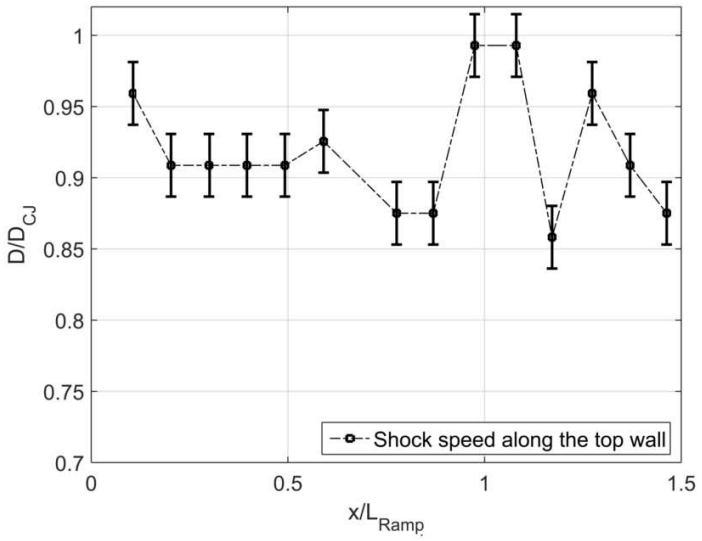

Figure A.31: Normalized detonation speed $\frac{D}{D_{CJ}}$ calculation and variation along the small ramp for propane mixture $C_3H_8 + 5O_2$ at 6.2 kPa.

X	Y	Delta_x	Delta_x(m)	FPS	V	Ramp End_X	Ramp End_y	Delta_x_Relative to ramp	D_CJ
24	12			42049		766	238	-0.326	2228
84	12	60	0.054	42049	1.012	766	238	-0.219	
145	12	61	0.055	42049	1.029	766	238	-0.110	V_ave
311	12	166	0.148	14016	0.933	766	238	0.187	0.889124074
364	12	53	0.047	42049	0.894	766	238	0.281	
416	12	52	0.046	42049	0.877	766	238	0.374	x_ref
463	12	47	0.042	42049	0.793	766	238	0.458	1120
520	12	57	0.051	42049	0.961	766	238	0.560	580
624	12	104	0.093	21025	0.877	766	238	0.746	Deltax_ref (pixels)
682	12	58	0.052	42049	0.978	766	238	0.850	540
727	12	45	0.040	42049	0.759	766	238	0.930	y_ref
763	12	36	0.032	42049	0.607	766	238	0.995	52
802	12	39	0.035	42049	0.658	766	238	1.064	52
874	12	72	0.064	42049	1.214	766	238	1.193	Deltax_ref (inches)
935	12	61	0.055	42049	1.029	766	238	1.302	19
994	12	59	0.053	42049	0.995	766	238	1.408	pxl -> m conv. Rate
1049	12	55	0.049	42049	0.928	766	238	1.506	0.000893704

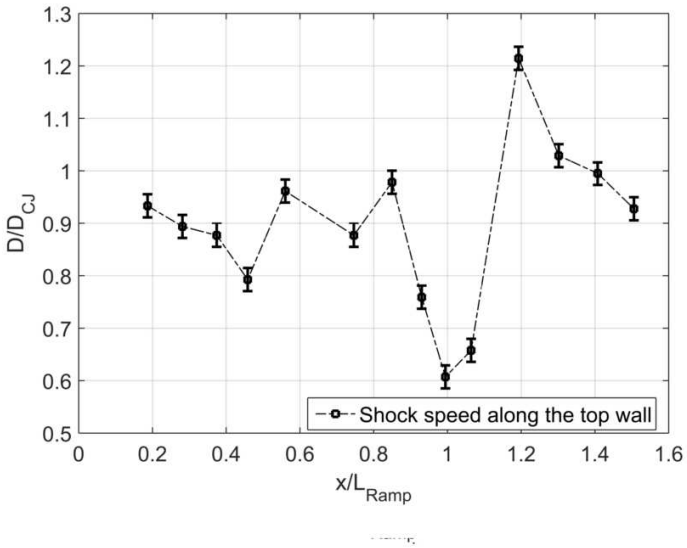

Figure A.32: Normalized detonation speed $\frac{D}{D_{CJ}}$ calculation and variation along the small ramp for propane mixture $C_3H_8 + 5O_2$ at 5.5 kPa.

X	Y	Delta_x	Delta_x(m)	FPS	V	Ramp End_X	Ramp End_y	Delta_x_Relative to ramp	D_CJ
59	11			42049		766	238	-0.264	2219.1
116	11	57	0.051	42049	0.965	766	238	-0.162	
173	11	57	0.051	42049	0.965	766	238	-0.060	
282	11	109	0.097	21025	0.923	766	238	0.135	
334	11	52	0.046	42049	0.881	766	238	0.228	
379	11	45	0.040	42049	0.762	766	238	0.308	x_ref
433	11	54	0.048	42049	0.914	766	238	0.405	1120
471	11	38	0.034	42049	0.644	766	238	0.473	580
505	11	34	0.030	42049	0.576	766	238	0.533	Deltax_ref (pixels)
597	11	92	0.082	21025	0.779	766	238	0.698	540
636	11	39	0.035	42049	0.660	766	238	0.768	
670	11	34	0.030	42049	0.576	766	238	0.828	y_ref
702	11	32	0.029	42049	0.542	766	238	0.886	52
732	11	30	0.027	42049	0.508	766	238	0.939	52
760	11	28	0.025	42049	0.474	766	238	0.989	Deltax_ref (inches)
787	11	27	0.024	42049	0.457	766	238	1.038	19
813	11	26	0.023	42049	0.440	766	238	1.084	
840	11	27	0.024	42049	0.457	766	238	1.132	
870	11	30	0.027	42049	0.508	766	238	1.186	
899	11	29	0.026	42049	0.491	766	238	1.238	
925	11	26	0.023	42049	0.440	766	238	1.284	
952	11	27	0.024	42049	0.457	766	238	1.332	
979	11	27	0.024	42049	0.457	766	238	1.381	pxl -> m conv. Rate
1005	11	26	0.023	42049	0.440	766	238	1.427	0.000893704
1030	11	25	0.022	42049	0.423	766	238	1.472	
1055	11	25	0.022	42049	0.423	766	238	1.517	
1080	11	25	0.022	42050	0.423	766	238	1.561	

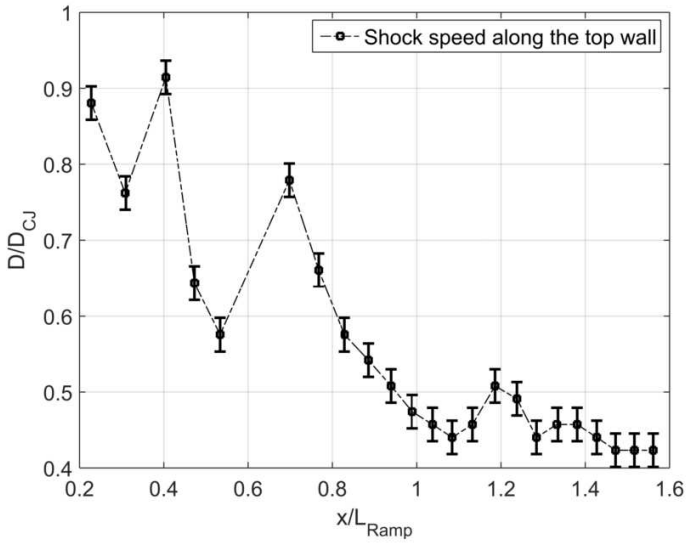

Figure A.33: Normalized detonation speed $\frac{D}{D_{CJ}}$ calculation and variation along the small ramp for propane mixture $C_3H_8 + 5O_2$ at 4.5 kPa.

Appendix B

Scaling conversions

B.1 Overview

This Appendix presents the details of the conversion performed between the scalings used in the numerical simulations of this thesis and the work performed by Short and Sharpe [47]. Reference and comparison with Short an Sharpe results was performed in Chapter 5 of the thesis in order to benchmark the code used for numerical simulations.

B.2 Comparison of different scalings

It is desirable to benchmark the code used for the numerical simulations of this thesis with the results existing in the literature. Accordingly, the problem of finding the stability boundary of one-dimensional detonation waves was selected. In this regard, the results obtained by the code written in the MG code platform were compared with the work performed by Short and Sharpe [47]. However the scalings used in the two studies were different so it was necessary to find expressions that allow us to interchange between the two scalings. The details of such conversion between the two scalings are elaborated in the following.

B.2.1 Reaction rate parameter, K_r

Due to the differences in the way time and velocity are scaled, the reaction rate parameter, K_r will also be scaled differently. The rate law for the reaction zone is expressed by

$$\frac{D\lambda_r}{D\tilde{t}} = \tilde{K_r}(1 - H(\lambda_i))(1 - \lambda_r)^\nu \tag{B.1}$$

In both works, the scaling used for length is the same (the induction zone length). In short and Sharpe, the velocity is scaled by the detonation velocity, $\tilde{D}$. In this work, the scaling used for velocity is $\sqrt{\tilde{p_0}/\tilde{\rho_0}}$. Accordingly, the scalings for K_r can be compared by the expression

$$\frac{K_r}{\overline{K_r}} = \frac{\tilde{D}}{\sqrt{\tilde{p_0}/\tilde{\rho_0}}} \tag{B.2}$$

where $\overline{K_r}$ represents the reaction rate parameter in the scalings of the work of Short and Sharpe, and K_r is the reaction rate parameter in terms of this work. for a perfect gas, $\tilde{c} = \sqrt{\gamma\tilde{p}/\tilde{\rho}}$. Using this, Equation B.2 can be rearranged in terms of more familiar variables:

$$\frac{K_r}{\overline{K_r}} = \frac{\sqrt{\gamma}\tilde{D}}{\tilde{c_0}} \tag{B.3}$$

$$\frac{K_r}{\overline{K_r}} = \sqrt{\gamma}M_{CJ} \tag{B.4}$$

Knowing $\overline{Q}$, the CJ mach number can be obtained [3]:

$$M_{CJ} = \sqrt{(1 + \frac{\gamma^2 - 1}{\gamma}\overline{Q}) + \sqrt{(1 + \frac{\gamma^2 - 1}{\gamma}\overline{Q} - 1)}} \tag{B.5}$$

Knowing the heat release and γ, the CJ Mach number could be obtained from Equation B.5. For example Short and Sharpe used the parameters $\overline{Q} = 4$ and $\gamma = 1.4$ which, from B.5 gives $M_{CJ} = 2.711$, and then from B.4 yields:

$$\frac{K_r}{\overline{K_r}} = 3.206 \tag{B.6}$$

In short and sharpe, for $E_a = 23.55$, the stability boundary was found to be $\overline{K_r} = 0.198$. Therefore in terms of the scalings used in this study, the stability boundary obtained by Short and Sharpe is obtained as $0.198 \times 3.206 = 0.635$.

Bibliography

[1] B V Voitsekhovski, B E Kotov, V V Mitrofanov, and A Topchiani. Optical studies of transverse detonation waves. *Izv. Sibrisk. Otd. Akad. Nauk SSSR*, 9:44, 1958.

[2] J H S Lee. Dynamic parameters of gaseous detonations. *Ann. Rev. Fluid Mech.*, 16:311–336, 1984.

[3] W Fickett and W C Davis. *Detonation theory and experiment*. Dover Publication Inc., 1979.

[4] J Austin. *The role of instability in gaseous detonation*. PhD thesis, California Institute of Technology, Pasadena, California, 2003.

[5] J H S Lee. *The Detonation Phenomenon*. Cambridge Univ. Press, Cambridge, 2008.

[6] J E Shepherd. Detonation in gases. *Proc. Combust. Inst.*, 32:83–98, 2009.

[7] K I Shchelkin and Y K Troshin. *Gas dynamics of combustion*. Md: Mono Book Corp., Baltimore, USA, 1965.

[8] Y N Denisov and Y K Troshin. Pulsating and spining detonation of gaseous mixtures in tubes. *Dokl. Akad. Nauk.*, 125:110–113, 1959.

[9] M I Radulescu, G J Sharpe, C K Law, and J H S Lee. The hydrodynamic structure of unstable cellular detonations. *J. Fluid Mech.*, 580:31–81, 2007.

[10] G J Sharpe. Transverse waves in numerical simulations of cellular detonations. *J. Fluid Mech.*, 447:31–51, 2001.

[11] R Deiterding. *Parallel adaptive simulation of multi-dimensional detonation structures*. PhD thesis, Brandenburgischen Technischen Universitat Cottbus, Cottbus, Germany, 2003.

[12] X Y Hu, D L Zhang, B C Khoo, and Z L Jiang. The structure and evolution of a two-dimensional h-2/o-2/ar cellular detonation. *Shock Waves*, 14:37–44, 2005.

[13] K Mazaheri, Y Mahmoudi, and M I Radulescu. Diffusion and hydrodynamic instabilities in gaseous detonations. *Combust. Flame.*, 159:2138–2154, 2012.

[14] Ya B Zeldovich. *Zh. Exp. Teor. Fiz.*, 10(5):542–568, 1940.

[15] J A Fay. Two-dimensional gaseous detonations:velocity deficit. *Phys. Fluids*, 2:283–289, 1959.

[16] YA B Zeldovich, B E Gelfand, YA M Kazdan, and S M Frolov. Propagation of detonation in a rough tube with deceleration and heat transfer being taken into account. *Sov. J. Fiz. Goreniya Vzriva*, 23:103, 1987.

[17] YA B Zeldovich, A A Borisov, B E Gelfand, S M Frolov, and A E Mailkov. Nonideal detonation waves in rough tubes. *Dynamics of explosions, A L Kuhl et al. (EDS), Prog. Astro. Aero*, 114:211, 1988.

[18] N Manson, C Brochet, J Brossard, and Y Pujol. Vibratory phenomena and instability of self-sustained detonations in gases. *Proc. Combust. Inst.*, 9:461–469, 1963.

[19] G Dupre, R Knystautas, and J H S Lee. *Dynamics of detonations and explosions: Detonations, Vol(106), chapter: Near-limit propagation of detonation in tubes*. Progress in Astronautics and Aeronautics, University of Colorado at Boulder, 1986.

[20] G Dupre, O Peraldi, J H S Lee, and R Knystautas. *Dynamics of detonations and explosions: Detonations, Vol(133), Chapter: Limit criterion of detonation in circular tubes*. Progress in Astronautics and Aeronautics, University of Colorado at Boulder, 1991.

[21] D H Edwards and J M Morgan. Instabilities in detonation waves near the limits of propagation. *Journal of Physics D: Applied Physics*, 10:2377–2387, 1977.

[22] V I Manzhalei. Detonation regimes of gases in capillaries. *Combust. Explo. Shock Waves.*, 28:296–302, 1992.

[23] J J Lee, G Dupre, R Knystautas, and J H S Lee. Doppler interferometry study of unstable detonations. *Shock Waves*, 5:175–181, 1995.

[24] A Chinnayya, A Hadjadj, and D Ngomo. Computational study of detonation wave propagation in narrow channels. *Phys. Fluids*, 25:036101, 2013.

[25] I O Moen, M Donato, R Knystautas, and J H S Lee. The influence of confinement on the propagation of detonations near the detonability limits. *Proc. Combust. Inst.*, 18:1615–1622, 1981.

[26] J Chao, H D Ng, and J H S Lee. Detonability limits in thin annular channels. *Proc. Combust. Inst.*, 32:2349–2354, 2009.

[27] A Camargo, H D NG, J Chao, and J H S Lee. Propagation of near-limit gaseous detonations in small diameter tubes. *Shock Waves*, 20:499–508, 2010.

[28] M I Radulescu. *The propagation and failure mechanisms of gaseous detonations: experiments in porous-walled tubes*. PhD thesis, Department of Mechanical Engineering, McGill University, Montreal, QC, 2003.

[29] M I Radulescu and J H S Lee. The failure mechanism of gaseous detonations: Experiments in porous wall tubes. *Combust. Flame*, 131:29–46, 2002.

[30] E K Dabora, J A Nicholls, and R B Morrison. The influence of a compressible boundary on the propagation of gaseous detonations. *Proc. Combust. Inst.*, 10:817, 1965.

[31] S B Murray and J H S Lee. The influence of yielding confinement on large-scale ethylene-air detonations. *Prog. Astro. Aero*, 94:80–103, 1984.

[32] S B Murray and J H S Lee. The influence of physical boundaries on gaseous detonation waves. *Prog. Astro. Aero*, 106:329–355, 1986.

[33] A A Vasil'ev, T P Gavrilenko, and M E Topochian. On the chapman-joguet surface in multi-headed gaseous detonations. *Astron. Acta.*, 17:499–502, 1972.

[34] J Li, X Mi, and A J Higgins. Effect of spatial heterogeneity on near-limit propagation of a pressure-dependent detonation. *Proc. Combust. Inst.*, 35:2025–2032, 2015.

[35] A Higgins. *Shock waves science and technology library, vol. 6 detonation dynamics, chapter 2: steady one-dimensional detonations*. Springer-Verlag Berlin Heidelberg, 2012.

[36] B E Gelfand, S M Frolov, and M A Nettleton. Gaseous detonations-a selective review. *Prog. Energy Combust. Sci*, 17:327–371, 1991.

[37] I Brailovsky and G Sivashinsky. Effects of momentum and heat losses on the multiplicity of detonation regimes. *Combust. Flame*, 128:191–196, 2002.

[38] J P Dionne, H D Ng, and J H S Lee. Transient development of friction-induced low-velocity detonations. *Proc. Combust. Inst.*, 28:645–651, 2000.

[39] A Makris. *The propagation of gaseous detonations in porous media*. PhD thesis, McGill University, Montreal, QC, 1993.

[40] A Makris, H Shafique, J H S Lee, and R Knystautas. Influence of mixture sensitivity and pore-size on detonation velocities in porous-media. *Shock Waves*, 5:89–95, 1995.

[41] A Sow, A Chinnayya, and A Hadjadj. Mean structure of one-dimensional unstable detonations with friction. *Journal of Fluid Mechanics*, 743:503–533, 2014.

[42] K Mazaheri, Y Mahmoudi, M Sabzpooshani, and M I Radulescu. Experimental and numerical investigation of propagation mechanism of gaseous detonations in channels with porous walls. *Combust. Flame*, 162:2638–2659, 2015.

[43] D N Williams, L Bauwens, and E S Oran. Detailed structure and propagation of three-dimesional detonations. *Proc. Combust. Inst.*, 26:2991–2998, 1996.

[44] J E Shepherd. *Dynamics of detonations and explosions: Detonations, Vol(106), Chapter: Chemical kinetics of hydrogen-air-diluent mixtures*. Progress in Astronautics and Aeronautics, University of Colorado at Boulder, 1986.

[45] M Vandermeiren and P J Van Tiggelen. Cellular structure in detonation of accetylene-oxygen mixtures. *Progress in Astronautics and Aeronautics*, 94:104–117, 1984.

[46] R A Strehlow and C D Engel. Transverse waves in detonation ii: structre and spacing in H2-O2, C2H2-O2, C2H4-O2 and CH4-O2 systems. *AIAA Journal*, 7:492–496, 1969.

[47] M Short and G J Sharpe. Pulsating instability of detonations with a two-step chain-branching reaction model: Theory and modeling. *Combust. Theor. Model.*, 7:401–416, 2003.

[48] R Bhattacharjee. *Experimental investigation of detonation re-initiation mechanisms following a mach reflection of a quenched detonation.* M.Sc Thesis, Department of Mechanical Engineering, University of Ottawa, Ottawa, ON, 2013.

[49] L Maley. *On shock reflections in fast flames.* M.Sc Thesis, Department of Mechanical Engineering, University of Ottawa, Ottawa, ON, 2015.

[50] M I Radulescu and B MCN Maxwell. The mechanism of detonation attenuation by a porous medium and its subsequent re-initiation. *J. Fluid Mech.*, 667:96–134, 2011.

[51] K Dennis, L Maley, Z Liang, and M I Radulescu. Implementation of large scale shadowgraphy in hydrogen explosion phenomena. *International Journal of Hydrogen Energy*, 39(21):11346–11353, 2014.

[52] G S Settles. *Schlieren and Shadowgraph Techniques.* Springer, 2001.

[53] B J McBride and S Gordon. Computer program for calculation of complex chemical equilibrium compositions. *Technical Report E-8017-1, National Aeronautics and Space Administration report*, Washington D.C, 1996.

[54] C A Eckett, J J Quirk, and J E Shepherd. The role of unsteadiness in direct initiation of gaseous detonations. *J. Fluid Mech.*, 421:147–183, 2000.

[55] C A Eckett. *Numerical and analytical studies of the dynamics of gaseous detonations.* PhD thesis, California Institute of Technology, Pasadena, California, 2000.

[56] R Klein. Curved detonations in expplosive gas mixtures with high temperature sensitivity. *Proceedings of The Zel'dovich Memorial, Moscow*, 12:288–315, 1994.

[57] R Klein, J C Krok, and J E Shepherd. Curved quasi-steady detonations: Asymptotic analysis and detailed chemical kinetics. *GALCIT Report*, FM 95-04, 1995.

[58] L T He. Theoretical determination of the critical conditions for the direct initiation of the detonations in hydrogen-oxygen mixtures. *Combustion and Flame*, 104:401–418, 1996.

[59] J Yao and D S Stewart. On the normal detonation shock velocity-curvature relationship for materials with large activation energy. *Combustion and Flame*, 100:519–528, 1995.

[60] M Sichel, N A Tonello, E S Oran, and A Jones. A two-step kinetics model for numerical simulation of explosions and detonations in H2-O2 mixtures. *Proc. R. Soc. Lond. A*, 458:49–82, 2002.

[61] W Fickett and W W Wood. Flow calculations for pulsating one-dimensional detonations. *Phys. Fluids*, 9:903–916, 2002.

[62] D S Stewart, T D Aslam, and J Yao. On the evolution of cellular detonation. *Proc. Combust. Inst.*, 26:2981–2989, 1996.

[63] V N gamezo, D Desbordes, and E S Oran. Formation and evolution of two-dimenional cellular detonations. *Combust. Flame*, 116:154–165, 1999.

[64] S H Lam and D A Goussis. Understanding complex chemical kinetics with computational singular perturbation. *Proc. Combust. Inst.*, 22:931–941, 1989.

[65] Ya B Zeldovich, G I Barenblatt, V B Librovich, and G M Makhviladze. *The mathematical theory of combustion and explosions*. Consultants Bureau, 1985.

[66] V P Korobeinikov, V A Levin, V V Markov, and G G Chernyi. Propagation of blast waves in a combustible gas. *J. Astronautica Acta*, 17:529–537, 1972.

[67] E S Oran, J P Boris, T R Young, M Flanigan, M Burks, and J M Picone. Numerical simulations of detonations in hydrogen-air and methane-air mixtures. *Proc. Combust. Inst.*, 18:1641–1649, 1981.

[68] S Taki and T Fujiwara. Numerical simulation of triple shock behavior of gaseous detonation. *Proc. Combust. Inst.*, 18:1671–1681, 1981.

[69] L He and P Clavin. Critical conditions for detonation initiation in cold gaseous mixtures by nonuniform hot pockets of reactive gas. *Proc. Combust. Inst.*, 24:1861–1867, 1992.

[70] E S Oran, A Jones, and M Sichel. Numerical simulations of detonation transmission. *Proc. R. Soc. Lond. A*, 436:267–297, 1992.

[71] K Kailasanath, J H Gardner, J P Boris, and E S Oran. Numerical simulations of unsteady reactive flows in a combustion chamber. *Combust. Flame*, 86:115–134, 1991.

[72] C Leung, M I Radulescu, and G J Sharpe. Characteristic analysis of the one-dimensional pulsating dynamics of chain-branching detonations. *Phys. Fluids*, 22:126101–126115, 2010.

[73] Z Liang, S Browne, R Deiterding, and J E Shepherd. Detonation front structure and the competition for radicals. *Proc. Combust. Inst.*, 31:2445–2453, 2007.

[74] S Browne, J Zeigler, and J E Shepherd. Numerical solution methods for shock and detonation jump conditions. *GALCIT Technical Report*, FM2006.006, 2006.

[75] B Borzou and M I Radulescu. *Evaluation of hydrogen, propane and methane-air detonations instability and detonability.* International Conference on Hydrogen Safety, ICHS, Brussels, Belgium, 2013.

[76] D Goodwin. An object-oriented software toolkit for chemical kinetics, thermodynamics, and transport processes. *Technical Report*, Caltech, Pasadena, 2009.

[77] Chemical kinetic mechanisms for combustion applications. University of california at san diego (http://combustion.ucsd.edu). *Mechanical and Aerospace Engineering (Combustion Research).*

[78] H D NG, M I Radulescu, A J Higgins, N Nikoforakis, and J H S Lee. Numerical investigation of the instability for one-dimensional chapman-jouguet detonations with chain-branching kinetics. *Combust. Theor. Model.*, 9:385–401, 2005.

[79] S A E G Falle. Self-similar jets. *Mon. Not. R. astr. Soc.*, 250:581–596, 1991.

[80] S A E G Falle and S S Komissarov. An upwind numerical scheme for relativistic hydrodynamics with a general equation of state. *Mon. Not. R. astr. Soc.*, 250:581–596, 1991.

[81] M I Radulescu and J H S Lee. On the hydrodynamic thickness of detonations. *Fizika Goreniya i Vzrya*, 41(6):157–180, 2005.